

We are IntechOpen, the world's leading publisher of Open Access books Built by scientists, for scientists

6,300

Open access books available

171,000

International authors and editors

190M

Downloads

Our authors are among the

154

Countries delivered to

TOP 1%

most cited scientists

12.2%

Contributors from top 500 universities



WEB OF SCIENCE™

Selection of our books indexed in the Book Citation Index
in Web of Science™ Core Collection (BKCI)

Interested in publishing with us?
Contact book.department@intechopen.com

Numbers displayed above are based on latest data collected.
For more information visit www.intechopen.com



Real-Time Particle Radiography by Means of Scintillating Fibers Tracker and Residual Range Detectors

Domenico Lo Presti, Giuseppe Gallo, Danilo Luigi Bonanno, Daniele Giuseppe Bongiovanni, Fabio Longhitano and Santo Reito

Abstract

In this chapter, a detailed description of the construction and the procedure for the measurement of performances of a charged particle imaging system is given. Such a system can be realized by the combined use of a position sensitive detector and a residual range detector. The position sensitive detector is made up of two superimposed and right-angled planes, each of which subsists of two layers of pre-aligned and juxtaposed scintillating fibers. The selected 500 μm square section fibers are optically coupled to two silicon photomultiplier arrays adopting a channel reduction system patented by the Istituto Nazionale di Fisica Nucleare. The residual range detector consists of 60 parallel layers of the same fibers used in the position detector, each of which is optically coupled to a channel of silicon photomultiplier array by means of two wavelength-shifting fibers. The sensitive area of both detectors is $90 \times 90 \text{ mm}^2$. The performance of the prototypes was tested in different facilities with protons and carbon ions at energy up to about 250 MeV and rate up to about 10^9 particles per second. The comparison between simulations and measurements confirms the validity of this system. Based on the results, a future development is a real-time radiography system exploiting high-intensity pencil beams and real-time treatment plan verification.

Keywords: real-time particle radiography, innovative detector readout strategy, beam monitoring, scintillating optical fibers, treatment plan verification

1. Introduction

Hadron therapy is a promising alternative in treatment of tumors, because it is one of the most effective techniques of external radiation therapy, which allows killing tumor cells while leaving almost intact the surrounding issue. In order to achieve the maximum effectiveness, high precision is needed in dose delivery, which requires a real-time adequate quality control of the beam parameters (position, profile, fluence, energy) combined with the precise measurement of patient positioning [1, 2]. QBeRT is a particle tracking system [3] and consists of a position-sensitive

detector (PSD) and a residual range detector (RRD) (see **Figure 1**). The main parts of this system are detectors expressly designed to achieve high-resolution imaging, high-resolution residual range measurement, large sensitive area, and high-rate beam compliance. The QBeRT system performs all these tasks and, advantageously, requires a low number of readout channels, making possible the reduction of the complexity and cost of the electronic data acquisition (DAQ) chain, by means of a readout channel reduction system patented by Istituto Nazionale di Fisica Nucleare (INFN) [4]. Both detectors, PSD and RRD, are able to work in imaging conditions, with particle rate up to 10^6 particles per second, and in therapy conditions (up to 10^9 particles per second). In imaging condition, the system is capable to realize a particle radiography and permits a real-time monitoring of the patient position in treatment room. In therapy condition, the PSD acts as a profilometer, detecting the position, the profiles, and the fluence of the beam. The combined use of the information measured by the PSD and the RRD allows to check the treatment plan in real time. The design of both detectors is based on scintillating optical fibers (SciFi) with 500 μm nominal square section.

The working principle of the scintillating optical fibers is schematized in **Figure 2**. SciFi consist of a polystyrene-based core and a PMMA cladding. The scintillating core is a mix of polystyrene and fluorescent dopants selected to produce the scintillation light when a particle releases energy in it and sets the optical characteristics for light propagation in the fiber. Scintillation light is produced isotropically but only a portion of these photons, in the two opposite directions along the fiber, can propagate by total internal reflection (TIR) mechanism. Multi-clad fibers have a second layer of cladding that has an even lower refractive index and permits TIR at a second boundary. External EMA is an optional external layer used to eliminate optical cross talk. SciFi sizes range from 0.25 to 5 mm square or round cross-sections and available in canes, spools, ribbons, and arrays.

The scintillation light is routed by the SciFi in the PSD, by means of wavelength-shifting fibers in the RRD, toward two silicon photomultiplier (SiPM) arrays, which output a proportional electric signal. PSD and RRD employ a DAQ chain divided in two sections. The first section consists of the front-end (FE) boards, which process the electric signal from the light sensor and perform the analog-to-digital conversion.

Data from the FE is acquired by a readout (RO) board based on a National Instrument system on module (SoM) for pre-analysis and filtering. The actual readout channel reduction scheme applied to the PSD limits the performances of

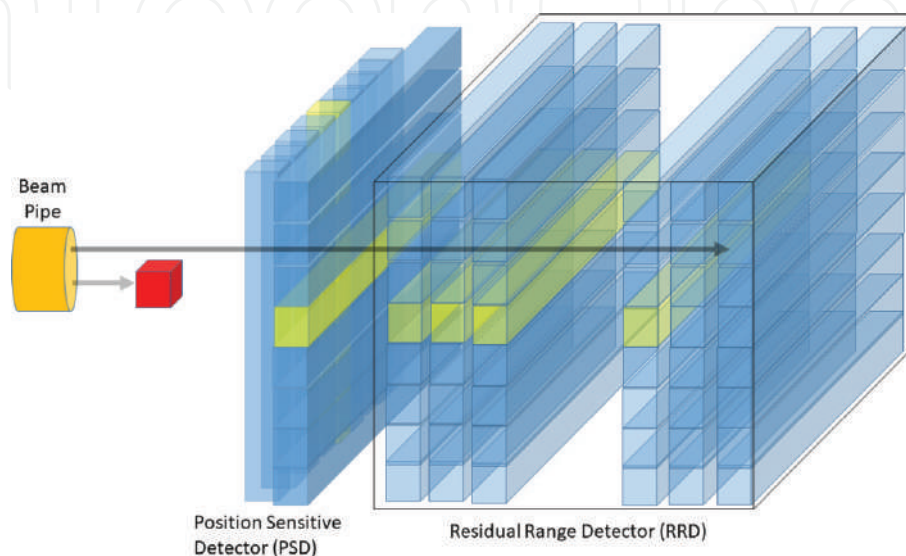


Figure 1.
Schematic of the QBeRT proton tracking system.

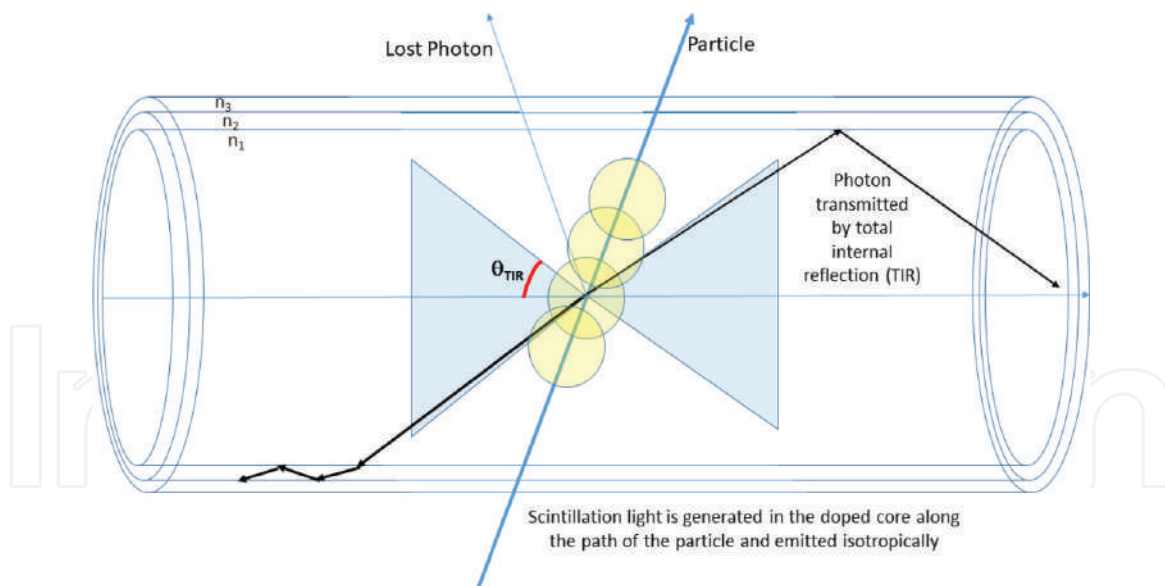


Figure 2.
Working principle of the scintillating fibers.

the detector when the beam spot size exceeds about 2 cm. Notice that the choice of the suitable readout channel reduction scheme and the modularity of the detector architecture allows to resize the sensitive area and the maximum beam spot size in order to fit any specific requirement. It is possible to obtain a large area detector (up to $400 \times 400 \text{ mm}^2$) covering a range up to 250 MeV protons with high spatial and range resolution (up to 150 and 170 μm , respectively). The detectors described in this chapter have been intensively tested in imaging and therapy (up to 10^9 proton/s) conditions [5] thanks to the collaboration with the colleagues working at CATANA facility (Centro di AdroTerapia ed Applicazioni Nucleari Avanzate at Laboratori Nazionali del Sud-Istituto Nazionale di Fisica Nucleare in Catania), at TIFPA (Trento Institute for Fundamentals Physics Applications) in Trieste, and at CNAO (Centro Nazionale di Adroterapia Oncologica) in Pavia.

2. The position-sensitive detector

The PSD prototype has a sensitive area of $90 \times 90 \text{ mm}^2$, which is made of two ribbons, layers of pre-aligned BCF-12 SCIFI, manufactured by Saint-Gobain Crystals, juxtaposed and orthogonally oriented, named the X and Y planes. The SciFi have 500 μm nominal square section. In detail, each single layer is composed of four ribbons of 40 fibers. The ribbons are optically isolated from each other by means of 220- μm -thick black adhesive tape to reduce cross talk between adjacent and overlapped ribbons. Each fiber is coated with white extra mural absorber (EMA) [6] to further reduce the cross talk between individual fibers. Particles intersecting the PSD's sensitive area deposit energy in the fibers which is partially converted in scintillation light. A fraction of this light is channeled in the core and propagated in the fiber toward the photo-sensor. When a particle loses suitable energy in all four SciFi layers, the coordinates of the intersection of its trajectory and the sensitive area can be measured. A picture of PSD detector is shown in **Figure 3**.

The PSD has 640 optical channels (four layers of 160 fibers each). The channel reduction system reduces the number of the readout channels without any data loss or degradation in the position measurement. The readout is performed in time coincidence, strongly reducing the effect of noise and chance coincidences, enhancing at the same time the performances of the system. The working principle of channel

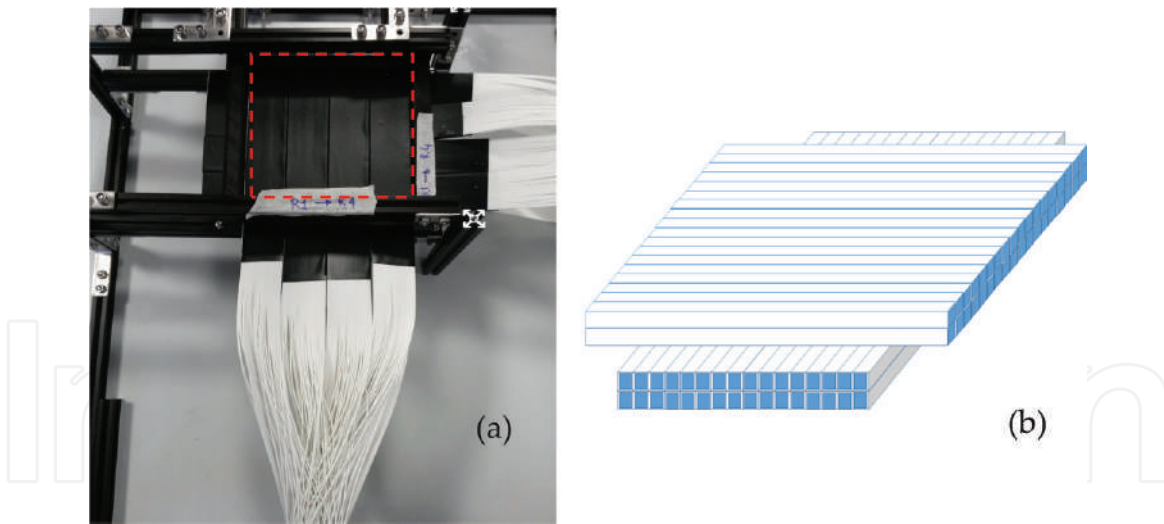


Figure 3. (a) Picture of PSD detector during the assembly phase. The dashed red box highlights the sensitive area of the detector. (b) A sketch of the arrangement of the four layers is shown.

reduction can be argued by considering a strip detector able to detect one particle at a time. Each strip can be read from both ends, and the signals are grouped following the scheme reported in **Figure 4**, where a two-dimension 16-strip detector is illustrated. All strips are read out, on one end, in m groups of n neighboring strips, named *NeigSet*, while at the other end, the first strips of each group are grouped in *StripSet1*, the second strips of each group in *StripSet2*, and so on to m . The two numbers are not necessarily the same. The minimum number of total channels, obtained by choosing $n = m$, is $4\sqrt{N}$, where N is the total number of strips per layer, X or Y. This implies that the number of readout channels on the second side is equal to the number of fibers per channel on the first side. A particle crossing one

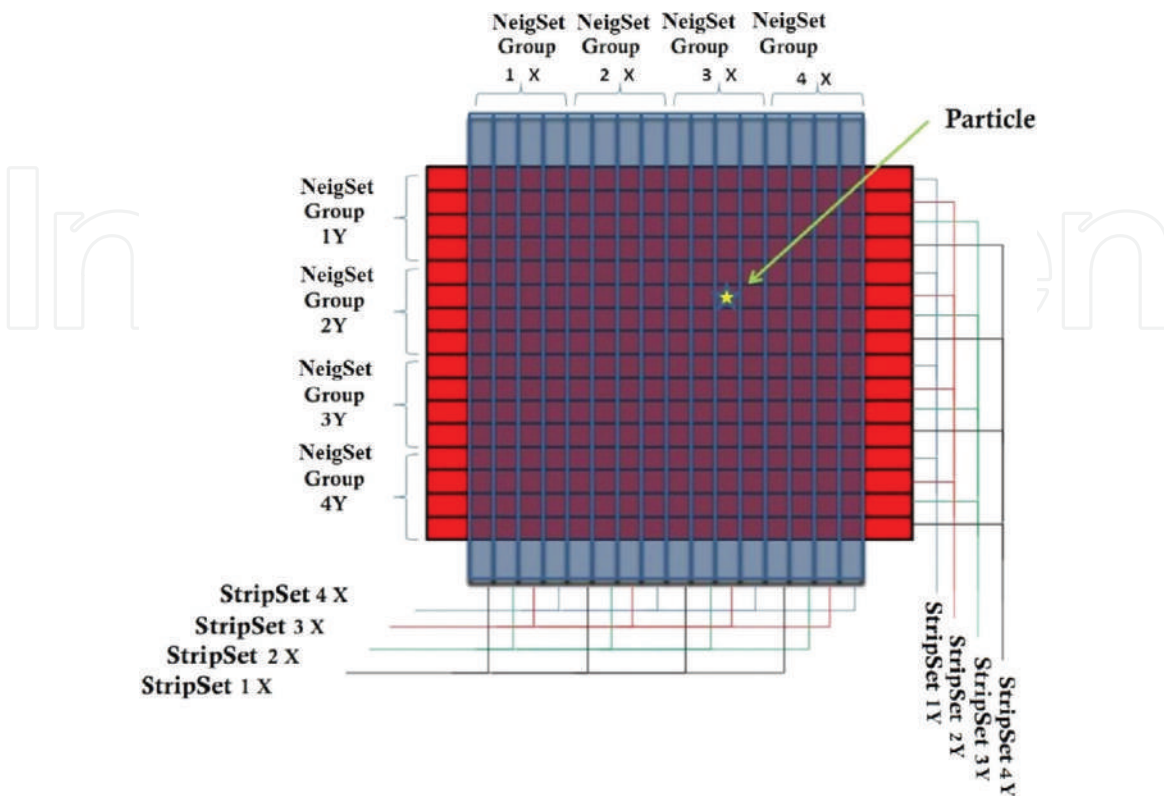


Figure 4. An example of the application of the channel reduction scheme to a two-dimension 16-strip detector.

strip generates a signal at both ends of the fiber. Then, we have a signal from the i^{th} *NeigSet* group and another from the j^{th} *StripSet* that univocally identifies the *Strip_{hit}* hit, according to equation (1):

$$\text{Strip}_{hit} = (i - 1) \cdot n + j. \quad (1)$$

The developed readout scheme reduces the number of readout channels to 16, instead of 32 channels without the application of the compression. When N is large, the reduction factor becomes important, allowing a compact and low-cost real-time acquisition. Notice that to reconstruct the point where the particle crosses the detector (event), an energy release in both planes is needed. In the PSD, readout occurs in time coincidence between the two layers of fibers for each plane. The channel reduction system can read the signal from the whole detector with only 112 channels (less than a fifth respect to the 640 total channels). Each of the 56 optical channels per plane is optically coupled to one of the 64 channels of a SiPM array. For a detailed description of the readout channel reduction system, see Refs. [7–10].

2.1 The PSD DAQ chain

As previously stated, the signals from the SiPM arrays are acquired by a DAQ chain divided in two main sections. The first section consists of the FE electronics which operate the analog-to-digital conversion. The digital-encoded data output from the FE is sent to the RO board which hosts a system on module (SoM) manufactured by the National Instrument (NI) for decoding and filtering. The SoM basically consists of a field-programmable gate array (FPGA) and a real-time processor, communicating by means of a direct memory access (DMA) data bus. The real-time processor has gigabit Ethernet connection for data transfer toward a PC, where the real-time visualization and storage of the results are accomplished.

Two FE boards, one for each direction, are required. Each FE board hosts a 64-channel SiPM array manufactured by Hamamatsu Photonics, mod. S13361-3050AE-08, with $3 \times 3 \text{ mm}^2$ photosensitive area per channel. These custom designed boards amplify and filter the analog signals from each SiPM array channel and compare them, by means of an array of fast comparators, to an individual threshold, remotely settable by a DAC. An individual threshold per channel is useful to compensate the unavoidable mismatch of the SiPMs gain and of the optical coupling of SiPM to fibers. The output of each FE board is an asynchronous digital data bus of 56 bits which represents the status of the SiPM signals and is acquired by the NI SoM on the RO board. The FPGA samples the FE output at high frequency, up to 250 MHz. This data is transferred toward the SoM processor via DMA. The processor applies real-time filtering algorithms and, after discarding the spurious events, reconstructs the impact point of the particles. The SoM's FPGA can be programmed via a graphical approach by means of the LabVIEW platform. The LabVIEW platform also manages the entire acquisition chain and data processing in real time.

3. The residual range detector

The RRD prototype is a stack of 60 layers, $90 \times 90 \text{ mm}^2$ area. Any layer is a ribbon of 180 BCF-12 SciFi. A picture of the detector is shown in **Figure 5(a)**. The ribbons are oriented horizontally and optically coupled at both ends to 1 mm square section wavelength-shifting fibers (WLS), see **Figure 5(b)** and **(c)**. To avoid optical cross talk between adjacent RRD layers, which would degrade range resolution and therefore energy measurement, each layer is optically isolated from the others by

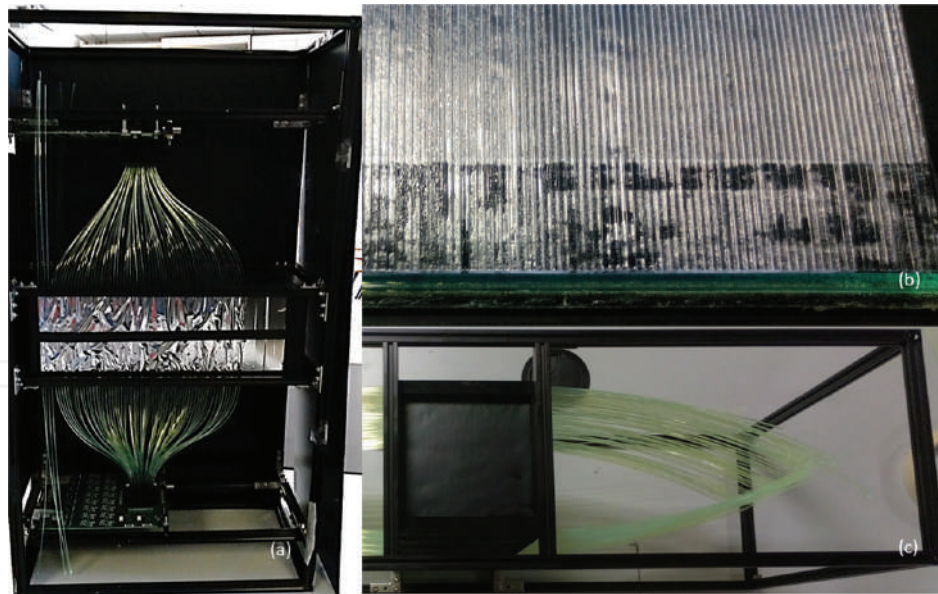


Figure 5. (a) View of the RRD prototype. (b) Detail of the optical coupling between SciFi and WLS fibers in a RRD layer. (c) View of the sensitive area of the RRD.

means of 100 μm black adhesive film. The SciFi used in the RRD are not coated with EMA because cross talk between adjacent fibers in the same layer does not affect detector resolution. The scintillation light produced in each layer at the passage of the particle is partially absorbed, reemitted, and channeled by the WLS. The two WLS coupled to a layer transfer the collected light to a channel of a SiPM array. The FE output is, then, processed by the DAQ chain. The SiPM array and the DAQ chain are identical to those used in the PSD described in the previous section.

A charged particle crossing the RRD passes through a number of layers as a function of its initial energy, before stopping. The dose deposited in each layer increases with depth up to the Bragg peak, where the particles produce the maximum amount of scintillation light. This point corresponds approximately to the end of the particles' path in the detector, so, by detecting the layer in which the light signal is the more intense, it is possible to measure their range. The RRD's working principle is reported in **Figure 6**. A calibration of the detector allows to obtain a

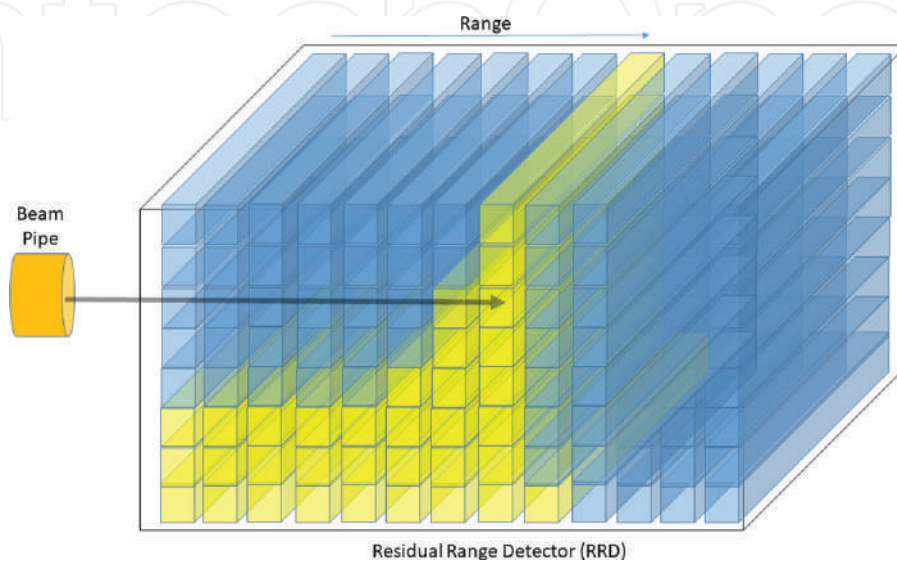


Figure 6. Working principle of the RRD. In this figure, the height of the yellow column is proportional to the energy released in each layer by a particle crossing the RRD.

range-energy characteristic curve, which can be fitted by a function $R_0 = \alpha E_0^p$. In this way, it is possible to retrieve the initial energy of the particles from the measured range. For the actual RRD, the maximum measurable range was about 36 mm in polystyrene/PVC corresponding to the range of protons with 67 MeV initial energy, but this maximum range can be easily extended up to higher energies by placing a stack of calibrated water-equivalent range shifters between the beam exit and the RRD entry window.

4. Experimental results

Measurements at CATANA were carried out to fully characterize the performance of the prototypes, with protons up to 58 MeV at the output in treatment room. During the last year, other measurements have taken place at TIFPA proton irradiation facility. The spatial resolution of the PSD was measured by means of a calibrated brass collimator applied at the beam pipe exit in the treatment room at CATANA. After data analysis, it is possible to estimate the holes' centers and compare them with the projection of the collimator holes on the detector plane. Then, the mean distances between the reconstructed centers and the collimator hole centers were calculated for each hole, and the mean distance was about 130 μm , comparable with the (a priori) spatial resolution of the PSD, given by $500 \mu\text{m}/\sqrt{12}$. The maximum spatial resolution is an intrinsic characteristic of the detector, independent of the readout strategy.

In order to calibrate the RRD, several measures of the range have been acquired changing the initial energy of protons. At CATANA facility, the proton beam energy can be passively modulated by placing a different calibrated PMMA range shifter at the beam pipe exit. The energy of the protons at the beam pipe exit was calculated by means of Monte Carlo simulation. The Bragg peak position is not exactly at the real end of the particles' path but just before. It is an experimentally consolidated practice to assume that the particle range measurement corresponds to the distance

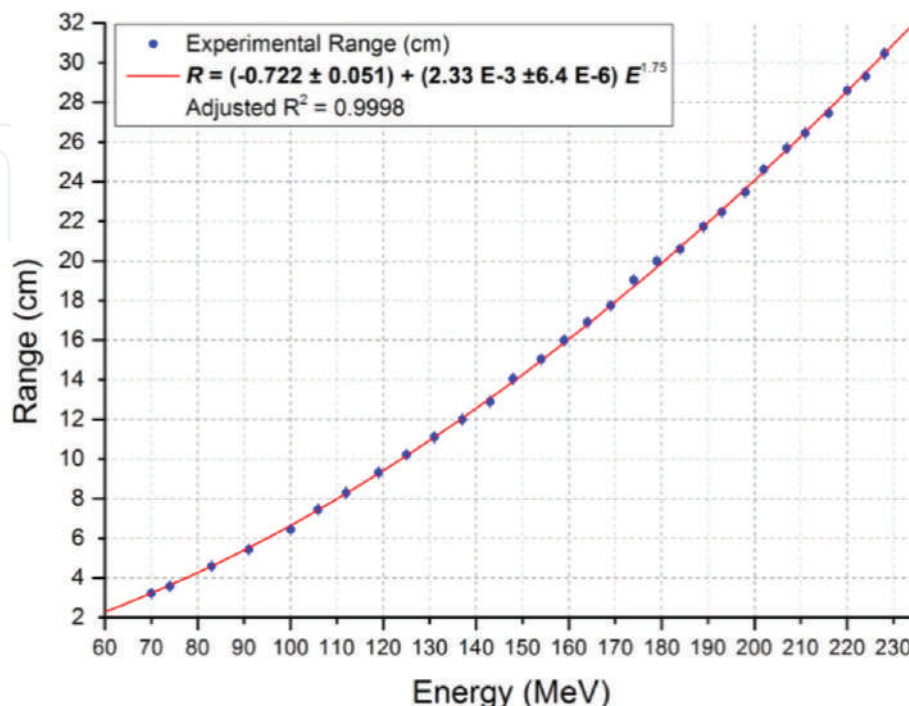


Figure 7. Measured values of the range vs. the corresponding proton energy at TIFPA and resulting data fit.

from the entrance window where the intensity of the signal is one tenth of its maximum value.

This distance corresponds to the layer on the right of the Bragg peak (or the next layer compared to the incident beam direction). The results of this measurement are compared with the range values calculated by means of a Monte Carlo simulation of the response of the detector. Both data sets were fitted with the power law (Eq. (1)):

$$R = a + b \cdot E^{1.75} \quad (1)$$

where R is the range of the protons in the RRD, E is the kinetic energy at the entrance of the RRD, and a and b are free parameters of fit.

The same measurement was performed at TIFPA with proton energy in the range between 70 and 250 MeV and with a high-intensity beam, up to 10^9 protons per second.

In order to extend the range of the RRD, a series of calibrated water-equivalent range shifters, 10-mm-thick polystyrene slab phantoms was placed in front of the entry window of the RRD every time the energy of the beam exceeded the range of detector alone. In **Figure 7**, the range vs. energy calibration graph, measured at TIFPA, is shown.

5. Beam profile measurement

The PSD can work as a profilometer at rate up to 10^9 particles per second therapy conditions. It is able to measure the size and the position of the beam spot. As a

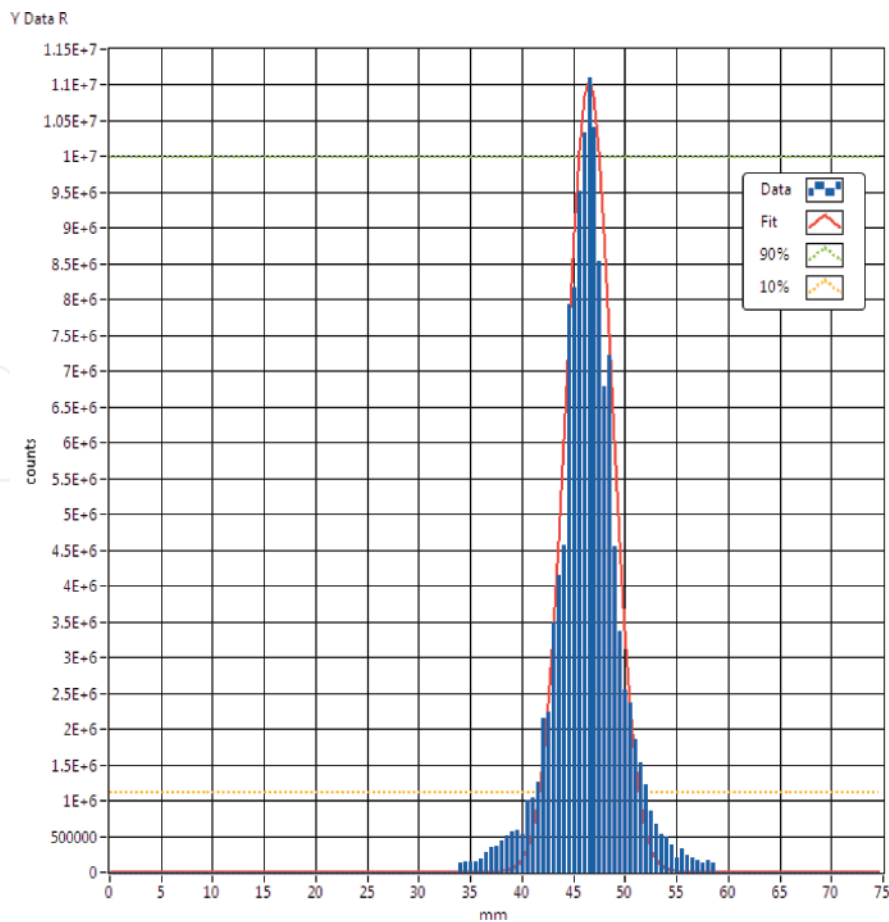


Figure 8. Examples of Y profile of the proton beam spot at 70 MeV. The calculated Gaussian fit, in red, is superimposed to data.

consequence of the application of the channel reduction system, the beam profile can be reconstructed only if the beam spot size is lower or equal to the width of a ribbon (about 2 cm). The PSD was tested as a profilometer at TIFPA, where the beam optics causes a reduction of the beam spot size with increasing energy. In the test, the PSD worked properly at high energies, as shown in **Figure 8**.

6. The proton radiography

The PSD and RRD have been tested in radiography configuration at CATANA. In this test, the experimental setup is the one previously described, but the two detectors were simultaneously active.

In order to acquire a radiographic image, a range measurement must be performed for each particle crossing the PSD at a given position. Then, data acquisition must run at low beam intensity (imaging conditions, about 10^6 particles per second on average). When a particle causes a quadruple time coincidence in the PSD, the crossing position within the sensitive area is measured, and a trigger signal starts the measurement of the particle range in the RRD. The software analysis associates the positions measured by the PSD to the RRD range measurements event by event. At the end of data acquisition for each pixel, the software analysis calculates the centroid by Gaussian fit of the range measurements distribution corresponding to that pixel. The result of this analysis is, therefore, a 160×160 matrix, as many as the PSD pixels, in which each element is the centroid of the range measurement of the particles that have crossed the corresponding pixel. Note that the use of a single PSD placed before the RRD can introduce a not negligible error for the fact that the input and output particle crossing positions through the calibrated target one must necessarily be assumed coincident or

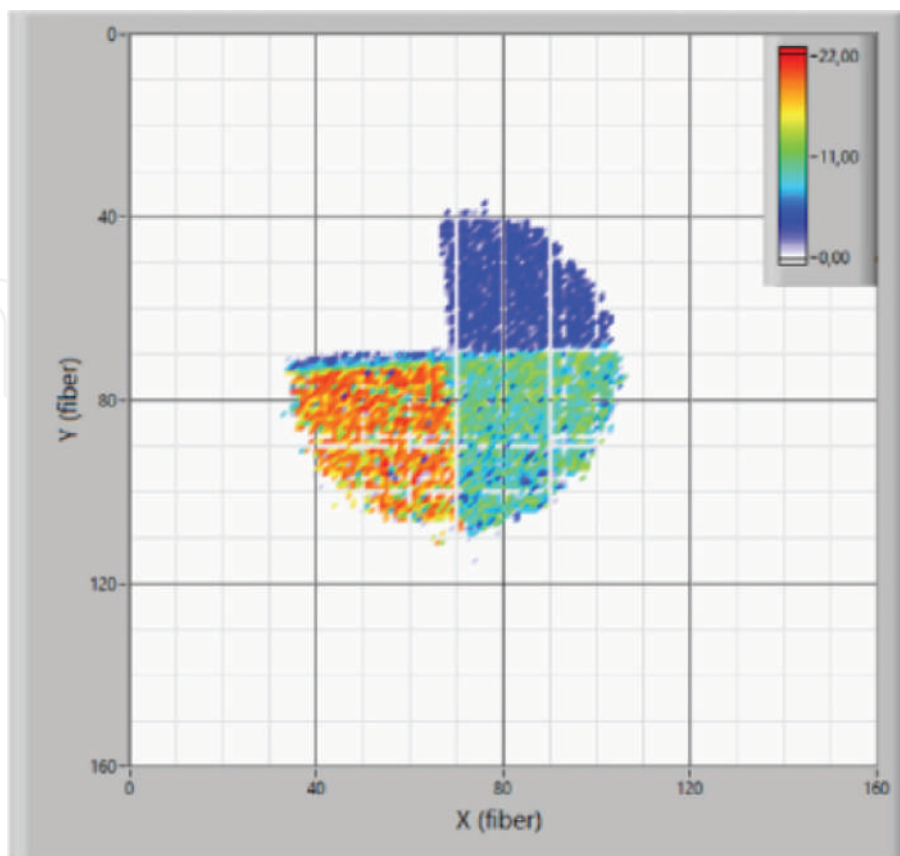


Figure 9.
The radiography of the ladder target with A12 range shifter.

undergone a negligible deflection traversing the medium. This error could be minimized using multiple PSD at different depths in the RRD.

A simple PVC target with the shape of a ladder was designed for the radiography test. Due to the homogeneous density of the target, in the radiography, only the differences in thickness traversed by the protons can be distinguished. The radiography image reported in **Figure 9** refers to a 3.5 cm diameter beam crossing a PMMA range shifter of about 10 mm thickness.

The z value in **Figure 9** is the centroid of the range distribution, expressed in numbers of RRD layers, pixel by pixel. Notice that the empty quarter-circle sector refers to the thickest step, 15 mm thick, of the ladder. The 58 MeV protons of the CATANA beam have insufficient energy to exit after passing through the thickness of the A12 range shifter and 15 mm of PVC. Moreover, border effects due to the non-orthogonality of the ladder with respect to the beam axis and the unavoidable divergence of the beam caused by the use of range shifters are visible in the radiography. The void pixels within the spot correspond to pixels where the range measurement statistics is too low. Many of these pixels are aligned along the same row or column, suggesting a correlation to low efficiency of the tracker in those areas. Two different 3D perspectives of the radiography are shown in **Figure 10(a)** and **(b)**. The last step in the analysis is the calculation of the relation between the measured range and the ΔE energy lost by the particles. The ΔE calculation must also take into account the energy lost by the particles in the PSD, which is placed between the target and the RRD. Since the sensitive areas of both detectors consist of 500 μm layers of SciFi, the PSD can be considered as an extension of the RRD. The residual proton range in the PSD and RRD was simulated as a function of the particle initial energy in the tracker E .

The range values thus obtained were fitted to the power law reported below in the equation, where R is the particle range in the RRD and PSD, expressed as the number of layers, and the resulting fit parameters are $A = -0.191 \pm 0.311$ and $B = 0.0370 \pm 0.0006$ (R -square = 0.998). Therefore, the energy loss ΔE can be easily calculated as

$$\Delta E[\text{MeV}] = 58 - \left(\frac{R - A}{B} \right)^{1/1.75}$$

The final radiography obtained after applying the energy-range conversion formula is shown in **Figure 11**.

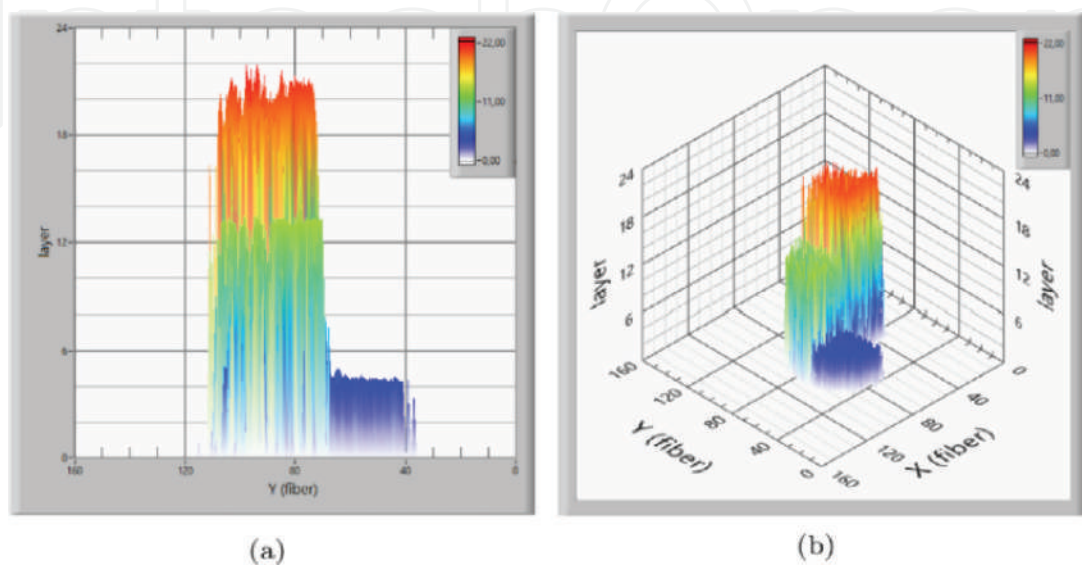


Figure 10. Two different perspectives of the 3D representation of the radiography: (a) lateral view and (b) isometric perspective.

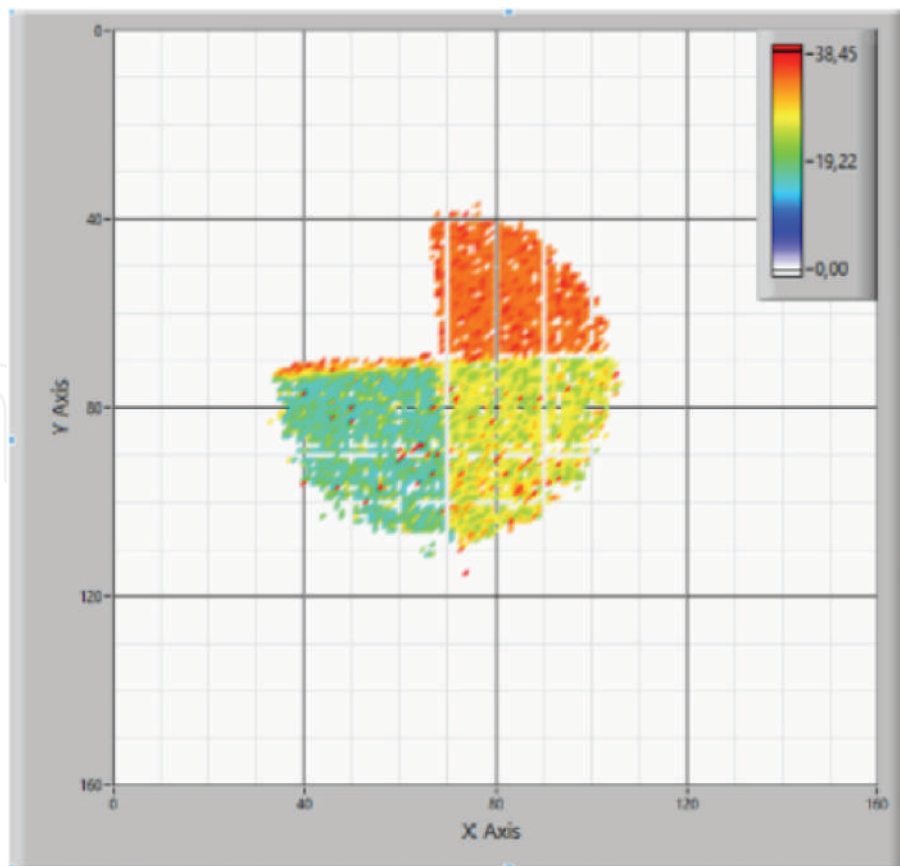


Figure 11.
The radiography of the ladder with A12 range shifter expressed in energy loss.

7. Radiograph data analysis

As mentioned earlier, radiography images reconstructed from range measurements are subject to some limitations: (i) lack of knowledge of the effective paths of the particles crossing the phantom because only one PSD was used. In this case, particle trajectories cannot be corrected according to the effect of Multiple Coulomb; (ii) further beam divergence was introduced by the tolerances in the alignment of the target, not exactly placed at isocenter and perpendicular to the incident beam direction. The reduction of the error in the calculus of the target thickness is obtained by the data filtering of range measurements. From the simulations, protons with an initial energy of 58 MeV crossing A12 range shifter, the target and the tracker, and stopping in the RRD have a maximum range straggling of $\sigma_{\text{str}} = 0.4$ mm, which already includes the effects of initial energy spread (0.3 MeV). So, in a region of interest (ROI) corresponding to a homogeneous quarter of the target, a range of measurements around the expected value from the simulation can be selected plus or minus two layers (equal to six times σ_{str}).

Subtracting the square of the maximum range straggling value of $\sigma_{\text{str}} = 0.4$ mm from the standard deviation of range measurements, it is again possible to find the a priori range resolution of about 170 μm . These mean range values can be converted into proton energy loss and subsequently into energy loss.

8. Future developments

The combined use of a pencil beam facility and the radiographic system, presented in this chapter, could allow the development of a faster real-time

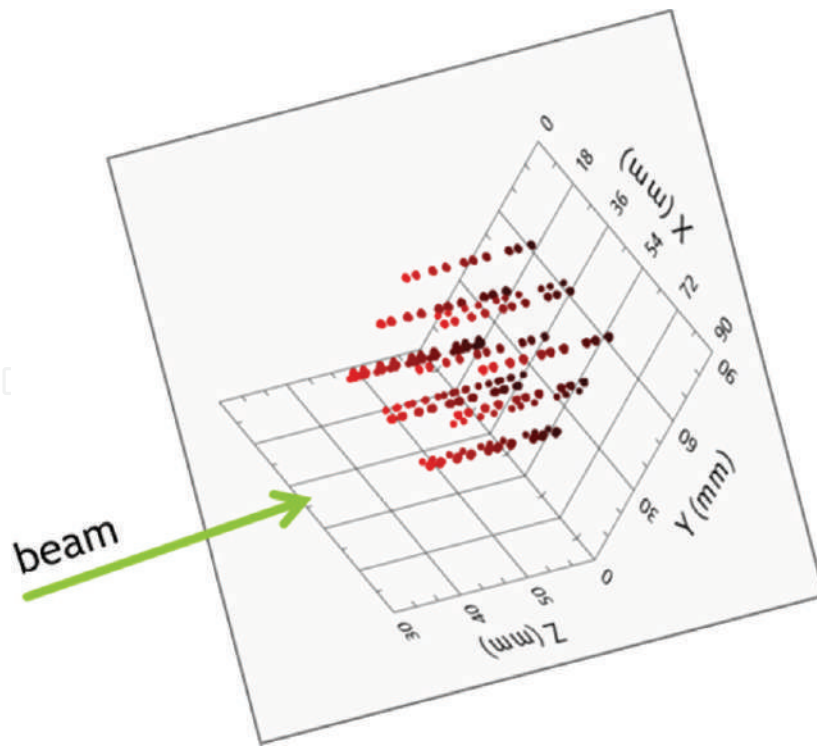


Figure 12. The real-time reconstructed pattern. The x and y for each point are measured by the PSD. The z is the range measured by the RRD. The color is proportional to the measured fluence.

radiographic technique. Furthermore, the acquired radiography will be spatially correlated with the treatment plan applied to the patient. Exploiting the features of the described proton imaging system, a new method of quantifying treatment plan quality will be investigated.

A demonstrative measurement has been performed at CNAO in Pavia. A simple pattern of point in the field of view of the radiographic system, presented in this chapter, was covered by the pencil beam. The same pattern was modulated in energy, in the range of energy compatible with the range in the RRD, in order to obtain a 3D matrix. Each point in the matrix was covered by the pencil beam in one spill delivering a fixed dose, up to 10^9 protons per spill. The PSD measured the centroid, the FWHM and the fluence of the beam delivered in each position. The RRD measured the centroid, the FWHM of the range of the protons delivered in each spill. **Figure 12** shows the real-time reconstructed pattern.

The results demonstrate the potentiality of the system. Accurate measurements will be performed in order to refine these statements in a quantitative way at TIFPA in a treatment room. In these future tests, a calibrated phantom will be used for the measurement.

The definition of the optimal parameters for the radiography, e.g., beam energy and fluence to be chosen in order to obtain the required spatial and density resolution will allow the definition of the specifications for the design of the final detectors.

9. Conclusions

This chapter presents the design and characterization of an innovative imaging system for charged particle beam based on SciFi. The system consists of a position-sensitive detector and a residual range detector. Both prototypes, with a sensitive area of $90 \times 90 \text{ mm}^2$, have cutting-edge performances, which distinguish them from

all other devices designed for the purposes considered in this chapter. In addition, improvements in the DAQ chain and the use of SiPM arrays make possible the use of the PSD as a beam monitoring and quality assurance system, by measuring real time the center and the shape of the spot, the fluence, and residual energy of the beam. The verification of this feature was investigated and demonstrated in beam tests. The performance of the PSD and RRD was tested at CATANA proton therapy facility with energies up to 58 MeV. Moreover, Monte Carlo simulations of the RRD detector response and the radiography of a calibrated target were measured by the system. From the analysis of the results and by a comparison with data from simulations, the architecture and the technology were validated.

Tests at CNAO and TIFPA validated the functionality of these devices with active beam shaping systems using protons with energies up to 250 MeV. Future developments concern the real-time qualification of a treatment plan and the comparison of the results with those provided by the official dose delivery system. Furthermore, the feasibility of a real-time radiography exploiting pencil beam will be tested.

Author details

Domenico Lo Presti^{1,2*}, Giuseppe Gallo^{1,2}, Danilo Luigi Bonanno²,
Daniele Giuseppe Bongiovanni², Fabio Longhitano² and Santo Reito²

1 Department of Physics and Astronomy, University of Catania, Catania, Italy

2 Istituto Nazionale di Fisica Nucleare, Catania, Italy

*Address all correspondence to: domenico.lopresti@ct.infn.it

IntechOpen

© 2018 The Author(s). Licensee IntechOpen. This chapter is distributed under the terms of the Creative Commons Attribution License (<http://creativecommons.org/licenses/by/3.0>), which permits unrestricted use, distribution, and reproduction in any medium, provided the original work is properly cited. 

References

- [1] Poludniowski G, Allinson N, Evans P. Proton radiography and tomography with application to proton therapy. *The British Journal of Radiology*. 2015;88(1053):20150134
- [2] Schneider U, Pedroni E. Proton radiography as a tool for quality control in proton therapy. *Medical Physics*. 1995;22(4):353-363
- [3] Gallo G, Lo Presti D, Bonanno D, Longhitano F, Bongiovanni D, Reito S, et al. QBeRT: An innovative instrument for qualification of particle beam in real-time. *Journal of Instrumentation*. 2016;11(11):C11014
- [4] Lo Presti D. Detector based on scintillating optical fibers for charged particle tracking with application in the realization of a residual range detector employing a read-out channels reduction and compression method. INFN Patent No. WO2013186798; 2013
- [5] Cirrone GAP et al. A 62-MeV proton beam for the treatment of ocular melanoma at Laboratory Nazionali del SUD-INFN. *IEEE Transactions on Nuclear Science*. Jun. 2004;51(3):860-865
- [6] SGC Products. Scintillating Fiber Webpage. <http://www.crystals.saint-gobain.com/products/scintillating-fiber>
- [7] Lo Presti D, Bonanno D, Longhitano F, Pugliatti C, Aiello S, Cirrone G, et al. A real-time, large area, high space resolution particle radiography system. *Journal of Instrumentation*. 2014;9(06):C06012
- [8] Lo Presti D, Aiello S, Bonanno D, Cirrone GAP, Leonora E, Longhitano F, et al. OFFSET: Optical Fiber Folded Scintillating Extended Tracker. *Nuclear Instruments and Methods in Physics Research Section A: Accelerators, Spectrometers, Detectors and Associated Equipment*. 2014;737:195-202
- [9] Lo Presti D, Bonanno D, Longhitano F, Bongiovanni D, Russo G, Leonora E, et al. Design and characterisation of a real time proton and carbon ion radiography system based on scintillating optical fibres. *Physica Medica*. 2016;32(9):1124-1134
- [10] Lo Presti D et al. An innovative proton tracking system for qualification of particle beam in real-time. *IEEE Transactions on Radiation and Plasma Medical Sciences*. 2017;1(3):268-274. DOI: 10.1109/TRPMS.2017.2690842

We are IntechOpen, the world's leading publisher of Open Access books Built by scientists, for scientists

6,300

Open access books available

171,000

International authors and editors

190M

Downloads

Our authors are among the

154

Countries delivered to

TOP 1%

most cited scientists

12.2%

Contributors from top 500 universities



WEB OF SCIENCE™

Selection of our books indexed in the Book Citation Index
in Web of Science™ Core Collection (BKCI)

Interested in publishing with us?
Contact book.department@intechopen.com

Numbers displayed above are based on latest data collected.
For more information visit www.intechopen.com



Review of Liquid-Filled Optical Fibre-Based Temperature Sensing

Fintan McGuinness, Gabriel Leen, Elfed Lewis, Gerard Dooly, Daniel Toal and Dinesh Babu Duraibabu

Abstract

While ever higher resolution temperature sensing is of demand in research and industry, the cost of sensors in the sub-milli-Kelvin (mK) range can be restrictive. Furthermore, as the majority of commercial temperature sensor measurements are transmitted via electrical circuits, significant post-processing is required to obtain a high-resolution due to phenomena such as electromagnetic interference, self-heating, electrical noise, etc. Consequentially, research in recent years has focused on the development of several technologies which overcome this issue, with optical fibre sensors proving to be a viable option. Owing to this, the following chapter will aim to review the current state-of-the-art in liquid filled optical fibre temperature sensing and the underlying methods.

Keywords: optical, fibre, temperature, sensor, liquid, review

1. Introduction

Prior to the development of thermometers, or indeed a scale of temperature, Renaissance Italy had already begun to question the nature of relative temperatures with scientific postulations such as *Bardi's problem*. This problem was posed by Count Bardi di Vernio to Galileo to determine why a person felt cold upon entering a river in summer, yet grew comfortable over time. While forgoing a direct solution to Bardi's Problem, Galileo reportedly developed a thermoscope in response [1]. Although the device was capable of showing variation in sensible heat it differed from a thermometer in that it did not have a defined scale, it also suffered from barometric influences due to the nature of its construction [2]. It should be noted at this point that there remains uncertainty over the original inventor of the thermoscope, however four prime candidates have been identified, these being; Galileo, Sanctorius Sanctorius, Robert Fludd and Cornelius Drebbel [1]. The advent of precision thermometry originated with the designs of Fahrenheit in the early eighteenth century, with his sealed mercury-in-glass thermometers being a significant advancement on the then state-of-the-art [2]. While specialised liquid-in-glass thermometers have demonstrated resolutions in the region of 0.2 K [3] they are the least useful for accurate measurements in a temporal sense. This is primarily due to the inability to perform transient measurements and relatively cumbersome geometry when compared to electronic sensors.

Currently, industrial temperature sensor designs typically rely on either the thermoelectric effect or temperature dependant resistance. Owing to their wide

operating range, thermocouples have been utilised in general engineering applications ranging from precision temperature control for tea processing factories to monitoring the cell temperatures of hepatoblastomas, with peak sensitivities in the region of 20 mK [4, 5]. However due to relatively poor response times, thermocouples are unsuited to high speed measurement. Another robust temperature sensor design is the negative temperature coefficient thermistor (NTC). A particular benefit to using NTCs is the ability to custom mould them for a desired application along with easily tunable resistance at the device and circuit levels [6]. Clow et al. [7] presented an array of NTCs used as a single sensor which was capable of 0.1 mK resolution with application in paleothermometry. While the sensor had excellent resolution it suffered from several drawbacks, the most relevant being a 7 s response time, which prevented it from recording highly transient temperatures gradients. Furthermore the sensor was sensitive to triboelectric effects from snow deposits on sensing wires and self-heating related noise, these being issues which scaled with distance. Precision resistance temperature detectors (RTDs) with milli-Kelvin (mK) resolution are readily available with a response time of 950 ms, and high-speed RTDs in the region of 400 ms [8]. While these sensors present high precision over their working range, a drawback of using RTDs is their inherent fragility. While suited for use in a laboratory, and other controlled environments, general deployment is still proving difficult at present. Hewlett & Packard pioneered the initial development of quartz thermometers in the mid-1960s, with resolution being in the range of 0.1 mK [9]. While capable of achieving sensitivity equivalent to the sensor presented by Clow et al. [7] the reported response time was 30% slower, and had a larger overall footprint.

The issues posed by the use of these *traditional* sensors in the presence of electromagnetic interference (EMI) and other considerations such as damage resilience and projected lifespan, has resulted in significant investment being made in the exploration of optical fibres as a means of high resolution temperature sensing. While still relatively fragile compared to thermocouples and glass bulb thermometers, optical fibre temperature sensors (OFTS) offer the possibility of a cost effective, high speed and precise sensor. The purpose of this review is to present the current state-of-the-art in a subset of optical fibre sensors that is to say, liquid-filled optical fibre temperature sensors (LiF-OFTS). Further to this, applications in which they have been utilised will be presented along with a discussion of potential future developments.

1.1 Temperature sensor requirements

As temperature sensors can be a mission critical piece of equipment various standards have been issued with respect to their usage. Common publishers of temperature sensor requirements for calibration and reporting include the ASTM [10] and IEEE [11]. The measurement range of a given sensor is largely determined by the nature of its operating environment. In an industrial process the range may be several hundred Kelvin, whereas a homeostatic biomedical thermometer requires a range in the order of only 15 K [12]. Some commercially available probes made from exotic materials such as a tungsten-rhenium alloy thermocouples (Types G, C and D) have wide working ranges, approximately 273–2590 K [13]. These commonly find application in processes involving high temperatures, however require further protection if being utilised in an oxidising environment.

The overall resolution of a temperature sensor may be more important than the operating range depending on an intended application. While it is not critical that a domestic oven have precision temperature control, it can be of great assistance to

Company	General Electric	Hanna Instruments	SENSTECH
Sensor type	PRT [18]	TC (K-Type) [8, 19]	NTC [20]
Min. temperature	283 K	73 K	218 K
Max. temperature	450 K	573 K	398 K
Resolution	0.003 K	0.1 K	0.044 K
Response time	0.5 s	4 s	0.75 s
Accuracy	0.5 K	0.5 K	0.5 K

Table 1.
 Commercially available high resolution temperature sensors.

pharmaceutical calorimetry. A review of the topic conducted by Buckton et al. [14] highlighted the need for identical and constant temperatures within the fermenter and calorimeter, along with maintaining an isothermal condition within the calorimeter itself. As the heat released in these reactions is typically of the order 1×10^{-4} mW it is readily evident that precision thermometry is beneficial in obtaining repeatable results. Rossi et al. [15] examined the relationship between intracranial and core temperatures in patients within 2–168 h post severe head injury. From this, intracranial temperatures were verified by comparison to the Delta OHM HD 9215, which had a resolution of 0.1 K. It was reported that core temperature was a poor indicator of intracranial temperature during pyrexial episodes, which was indicative of benefits to independent high resolution temperature sensing within the cranium. As magnetic resonance imaging (MRI) is common in patients post trauma, significant benefit would be provided should the thermometer be unaffected by the strong magnetic field, as it may remain in place to continue real-time monitoring.

Sampling rate is an important factor when deciding on a temperature sensor as it has to be considered in conjunction with the sensor response time. If the heat transfer from the system is known, then a rate of temperature change may be determined by Eq. (1) [16]. Evidently as temporal resolution is increased smaller variations in heat, and as a consequence temperature, may be determined.

$$\frac{\delta Q}{\delta t} = c \cdot \frac{\delta T}{\delta t} \quad (1)$$

Further to the items outlined above, specialised considerations may be required. In automotive engine development it is commonplace to embed multiple sensors inside the cylinder head/wall. While electronic sensors operate with little issue for the majority of a four-stroke cycle (720°) the spark plug activates for several degrees before or after top dead centre. As this is a period of strong pressure and thermal gradients, EMI introduced by the spark plug creates difficulty in analysing the recorded data [17]. A small sample of commercially available high resolution temperature sensors is presented in **Table 1**.

2. Advantages of optical fibre sensors

As mentioned in the introduction, optical fibre sensors present many advantages over their electronic counterparts. Therefore, the following section will examine several properties of optical fibres which indicate their viability as an alternative to electronic sensors.

2.1 Construction

Commercially available silica fibres are widely used in the development of optical fibre temperature sensors owing to their small cross-sectional area and consequently their ability to be implemented in restricted areas. However, the relatively low cost of silica fibre compared to more exotic fibres such as those manufactured from fluoride or synthetic sapphire may be a factor to consider. As is reported, optical fibre sensors are particularly suited to environments where an electronic sensor may not have sufficient protection from EMI, and where line of sight to the measurement point is obstructed [21]. Furthermore, optical fibre sensors do not represent a potential source of ignition in an explosive environment; can be biocompatible; and can be made to work over very long distances. To date, optical fibre temperature sensors have been implemented in applications ranging from *in-vivo* biomedical sensing [22], to structural and geothermal engineering [23].

2.2 Measurement stability

In civil engineering applications, such as bridges, use of chirped fibre Bragg gratings (FBGs) provide excellent through life performance as fibre degradation is in excess of 25 years [24] with data transmission losses being minimal [23]. Furthermore, stability of measurements are generally quite good due to performance being driven predominantly by the wavelength stability of light source used. This being an easy factor to account for, as said light source may be kept in a controlled environment.

2.3 Distributed sensing

In addition to the EMI resistance and dimensional advantages of using optical fibre sensors, their ability to provide multipoint sensing with minimal use of fibre is a desirable characteristic. One such method is the use of chirped FBGs whereby multiple FBGs are inscribed on a single fibre, with the grating period modified at each location thus providing high spatial resolution. Wave division multiplexing (WDM) is another commonly used method in multi-point sensing with optical fibres, however this method narrows the usable bandwidth of light proportionally to the number of fibres used. Historically, Raman scattering has been used as an efficient means of multi-point temperature measuring; however, Brillouin sensors reported have shown exceptional strain measurement capability for an equivalent temperature sensing performance [25].

3. Theory and working principles

In the use of optical fibres for temperature sensing, measurements can be conducted using both intrinsic and extrinsic techniques. The most common technique for assessing temperature changes using optical fibres is the use of interferometry. Examples being fibre Bragg gratings (FBGs), extrinsic Fabry-Perot interferometers (EFPIs), Mach-Zehnder interferometers (MZIs) and Sagnac interferometers (SIs). As the fibre requires a light source to conduct the measurement, various types have been explored such as; broadband light source [26] monochrome laser [21] and swept laser [27]. Measurements can be carried out by observing either the transmitted spectrum, or the reflected spectrum. When recording the reflected spectrum losses occur in the back reflections through the fibre and at the coupler between the light source and spectrometer. That said however, this method allows

for the fibre to be used as a point measurement device in applications where transmission is impractical, i.e. biomedical [28], automotive [29], and pharmaceutical [30] sensing. As the modus operandi of any particular optical fibre sensor is modulation of the light source, this can be carried out via intensity, frequency, or phase modulation. The latter of which will be the main focus of the review as this is the method typically employed by LiF-OFTS.

3.1 Fibre Bragg gratings

Fibre Bragg gratings are created by periodically modifying the refractive index of an optical fibre core. At each change of refractive index the reflected light constructively interferes producing a high intensity narrowband signal. This effect is described by Eq. (2) where λ_B is the Bragg wavelength, n_{eff} is the effective refractive index, and Λ is the pitch between each of the modified refractive indices. **Figure 1** provides a schematic of an FBG inscribed on a fibre core. As is evident from Eq. (2) care must be taken to eliminate, or account for, mechanical straining of the fibre as this will artificially modify the grating period. Once mechanical strain has been determined the change in Bragg wavelength with temperature is given by Eq. (3). A review on the packaging of FBGs is provided by Hong et al. [31].

$$\lambda_B = 2n_{eff} \cdot \Lambda \quad (2)$$

$$\frac{d\lambda_B}{dT} = 2 \left(n_{eff} \cdot \frac{d\Lambda}{dT} + \Lambda \cdot \frac{dn_{eff}}{dT} \right) \quad (3)$$

Owing to the simple nature of their construction FBGs have been utilised to great success as a means of sensing temperature, however they are not without inherent issues such as damage due to exposure to excessive temperatures [22], and grating orientation to the heat source [32]. Zhang et al. [22] reported the assessment of cylinder head temperature and mixture flow within maritime diesel engines, where significant steps were taken to protect the fibre coating from excessive cylinder head temperatures (873.15 K). Gassino et al. [32] examined the use of FBGs in the presence of strong temperature gradients (~ 10 K/cm) during thermal ablation of tumours. Several key design factors were discussed from which it was determined the largest sources of error were caused by the temperature gradient along the length of the FBG, and FBG orientation with respect to the temperature gradient.

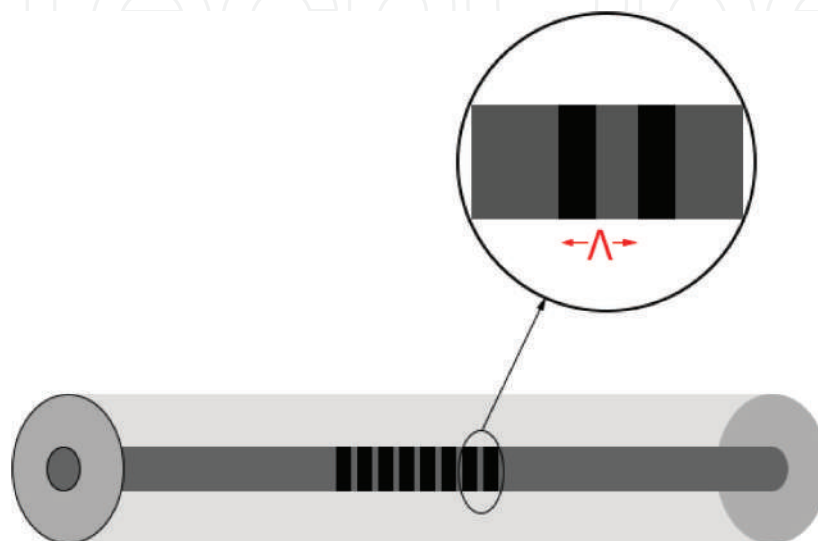


Figure 1.
 Schematic of FBG, highlighting grating pitch (Λ) in fibre core.

3.2 Extrinsic Fabry-Perot interferometers

Fabry-Perot based sensors are typically extrinsic in nature and used as a point measurement device at the tip of an optical fibre. A common construction of EFPI sensors involves a single mode fibre (SMF) spliced to a capillary with a multi-mode fibre (MMF) which acts as a diaphragm fused to the opposing end of the capillary, creating an air filled cavity between the SMF and MMF. **Figure 2** highlights the dimensions relevant to diaphragm deflection and rigidity, with the construction presented in **Figure 3**. As light reaches the end face of the SMF a portion of the light is reflected, with the remainder transmitted into the air cavity. Similar reflections occur at the air-diaphragm, and diaphragm-external media interfaces. As the light reflected from the inner and outer faces of the diaphragm has travelled a greater distance, than the light reflected at the end face of the SMF, a phase difference between reflections will exist. While FPIs behave similar to FBGs in that they have varying refractive indices along the axial direction, adjustment of the diaphragm thickness can be used as a means of increasing pressure sensitivity by modifying the diaphragm flexural rigidity. Said flexural rigidity is determined by Eq. (4) [33] where h , E and ν are the diaphragm thickness, Young's modulus, and Poisson's ratio respectively. Eq. (5) [33] provides the relationship between diaphragm displacement and uniformly applied pressure, this being fundamental to the temperature sensor presented by Poeggel et al. [34]. From this it becomes apparent that a thinner diaphragm leads to greater maximum deflection, and said maximum deflection occurs at the diaphragm centre.

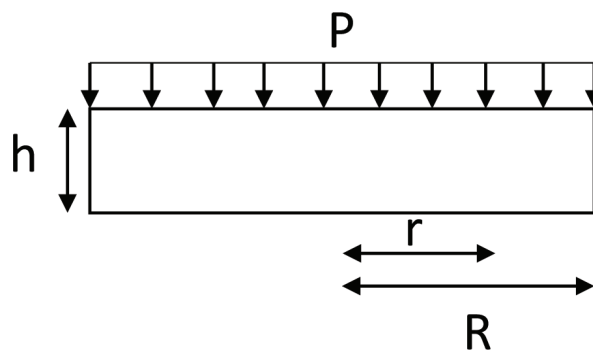


Figure 2.
Dimensions which influence diaphragm flexural rigidity and deflection.

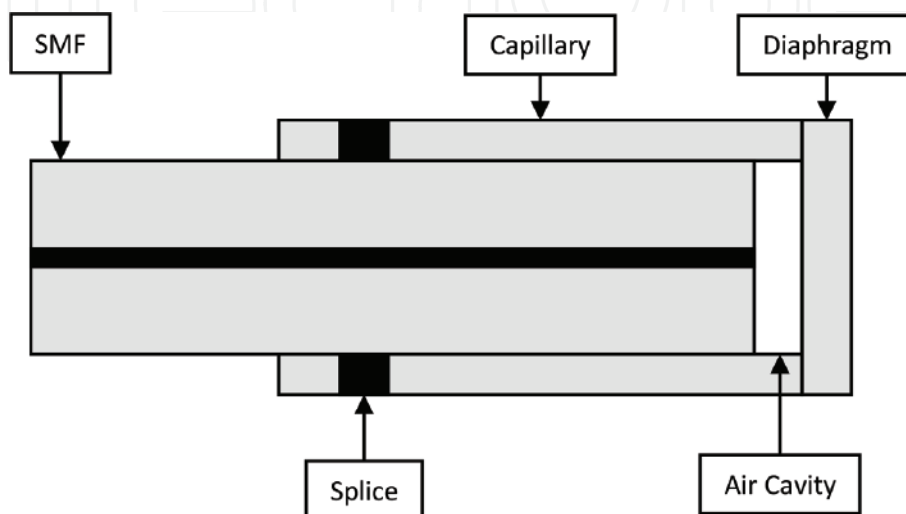


Figure 3.
Schematic of typical EFPI.

$$D = \frac{Eh^3}{12(1 - \nu^2)} \quad (4)$$

$$z(r) = \frac{3}{16} \cdot \frac{(1 - \nu^2)(R^2 - r^2)}{Eh^3} \cdot P \quad (5)$$

Gao et al. proposed an alternative construction, using particle vapour deposition (PVD) to create a ‘diaphragm’, which was fused directly to an MMF [35]. This construction provides a number of advantages, such as a robust construction, and the ability to custom tune optical path lengths without the uncertainties related to splicing. Eq. (6) presents the relationship between the optical path differences (OPD) with the thermal coefficients of refractive index (α_n) and material thickness (α_d) for the PVD diaphragm.

$$\frac{OPD(T)}{OPD(T_0)} \approx 1 + (\alpha_n + \alpha_d)(T - T_0) \quad (6)$$

3.3 Mach-Zehnder interferometers

Mach-Zehnder interferometers (MZIs) operate by splitting the source light and introducing an optical path difference, before recombining the beams prior to the detector [36]. As a means of sensing in optical fibres, common practice has been to splice a length of photonic crystal fibre (PCF) between two lengths of SMF [37–40]. These operate by allowing the core mode of the SMF to be split into core and cladding modes at the first splice point within the PCF. These are subsequently rejoined at the second splice point with an interference between the two modes becoming apparent in the transmission, this is usually represented by resonant dip (s) in the signal transmitted to the optical spectrum analyser (OSA). Modification to the air holes of the PCF is commonly carried out via collapsing or filling with various fluids, in order to increase sensitivity to the desired measurand. For the purpose of temperature sensing it is common to fill the PCF holes with a fluid which has a high magnitude (as it may be positive or negative) thermo-optic coefficient [37, 39, 41, 42]. **Figure 4** below provides a schematic of how a typical MZI sensor setup is presented in literature. In a PCF the two branches of the MZI are the cladding and core modes respectively. A transverse section of a PCF is presented in **Figure 5** where the core, and cladding air holes are highlighted.

3.4 Sagnac interferometers

Sagnac interferometers (SIs) behave similarly to MZIs in that they compare optical path differences of two beams which have been split and subsequently recombined. However, they differ such as the two beams counter-propagate with

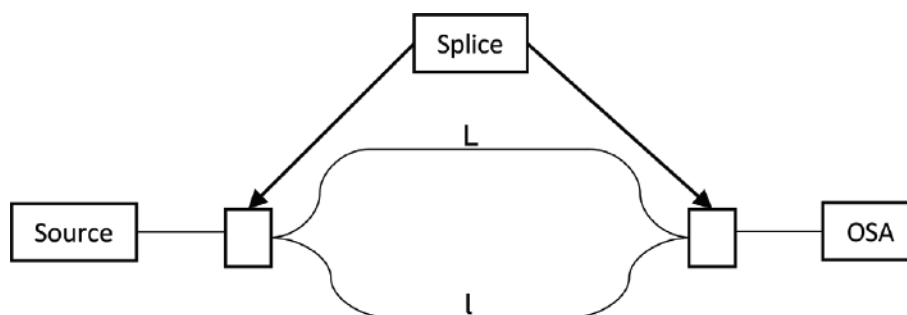


Figure 4.
 Schematic of Mach-Zehnder based sensor.

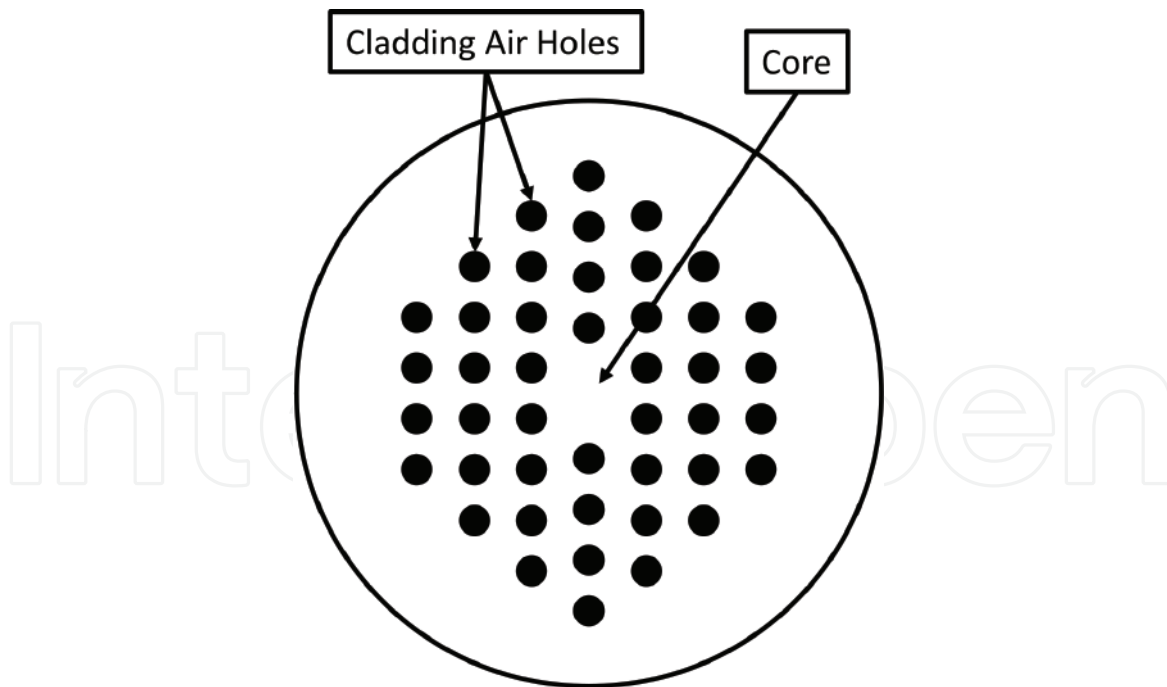


Figure 5.
Transverse section of a photonic crystal fibre.

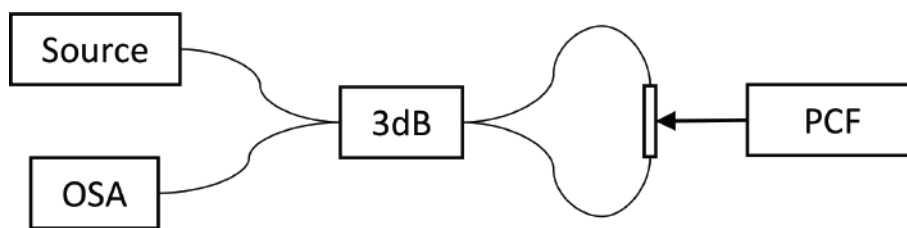


Figure 6.
Schematic of potential Sagnac interferometer based sensor.

respect to each other before being recombined at the detector. This type of interferometer is the basis of fibre-optic gyroscopes [43]. While it has been utilised in thermometry [44, 45] the sensors reported have not seen a similar level of research compared to their MZI counterparts. Reported sensors used a source beam counter-propagated by a 3 coupler. Birefringence in the PCF resulted in the optical path difference which was detected by the OSA [44, 45]. **Figure 6** above highlights how an SI based sensor may be constructed using optical fibre equipment.

4. Liquid filled optical fibre temperature sensors

As evident from Sections 1 and 3 temperature sensors have a long history. With respect to LiF-OFTSs however, while several types of sensor and base technologies have been presented in the literature, the authors have not encountered a concise review of said sensors. The materials utilised have included; alcohol [44] motor oil [34], silicone (polydimethylsiloxane) [46], and immersion oils [39]. While polydimethylsiloxane (PDMS) has only been presented in its cured form, it is not inconceivable that the liquid form be used given its optically transparent nature. The following section is arranged by the base interferometry principle of each fluid filled sensor.

4.1 EFPI type sensors

Chen et al. presented an FPI construction which contained an air micro-bubble encased in cured PDMS [46]. The sensor was manufactured by splicing an SMF to a hollow core fibre (HCF) 282 μm in length. The PDMS was subsequently introduced into the HCF via capillary effect. As PDMS entered the HCF it formed the air micro-bubble with the SMF, where the length of air micro-bubble was controlled by the period of time PDMS was allowed to enter the HCF. Online monitoring was conducted to establish the free spectral range (FSR) best suited to the desired application. A schematic of the sensor is presented in **Figure 7**.

The PDMS was cured for 45 min at 338.15 K, fixing the length of the air micro-bubble. Testing was conducted between 324.35–343.65 K and compared to a PT100 thermometer with a resolution of 0.01 K. Results indicated sensitivity was quite high with a value of 2.7035 nm/K and a highly linear response where $R^2 = 0.992$. In addition to the reported sensitivity, reference was made to the benefit of using a double FPI in the sensor. This consisted of a thin FPI (air micro-bubble) and thick FPI (PDMS filling). The thin FPI allowed for a large FSR and the thick FPI offered high temperature resolution.

Poeggel et al. [34] presented a novel ultra-high resolution temperature sensor (UHRTS). The sensor was comprised of an existing optical fibre pressure temperature sensor (OFPTS) [47] which was further encased in an outer oil-filled capillary. The sensor was noted to have an external diameter of less than 1 mm lending to its capability to be used in volume restricted areas, a schematic of the sensor is provided in **Figure 8**. By combining an FBG with the highly sensitive EFPI, the UHRTS behaved similar to that of Chen et al. [46] in that the FBG and air cavity allowed for a wide spectral range to be utilised with the diaphragm element providing high resolution. Dissimilar to Chen et al. however, the construction of the OFTS was reliant on the thin diaphragm element to transduce volume changes in the oil to a temperature measurement. This being demonstrated by Eqs. (4) and (5) in Section 3. It was claimed that the high ratio of oil in the outer capillary compared to air in the EFPI cavity was what resulted in high sensitivity. The sensor presented had a reported, theoretical, sensitivity of 52.7×10^3 nm/K. Comparison of the UHRTS to a Bosch BMP085 [48] was carried out over a temperature range of 7 K. While both sensors detected the 7 K variation, measured EFPI sensitivity was much lower than predicted, at 8.77 nm/K. It was suggested that the error was likely caused by inconsistencies in the manufacturing process of the sensor, and the presence of micro air bubbles in the oil which resulted in response damping. Considering oil was introduced into the capillary via a micro-syringe rather than by capillary effect as utilised by several authors such as Chen et al. [46] and Xu et al. [39] this may have

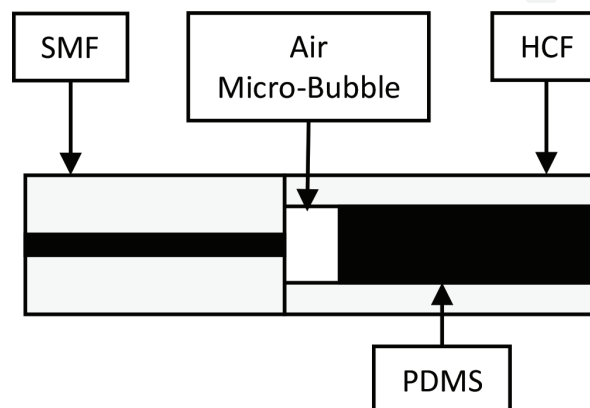


Figure 7.
Schematic of PDMS FPI sensor based on Chen et al. [46].

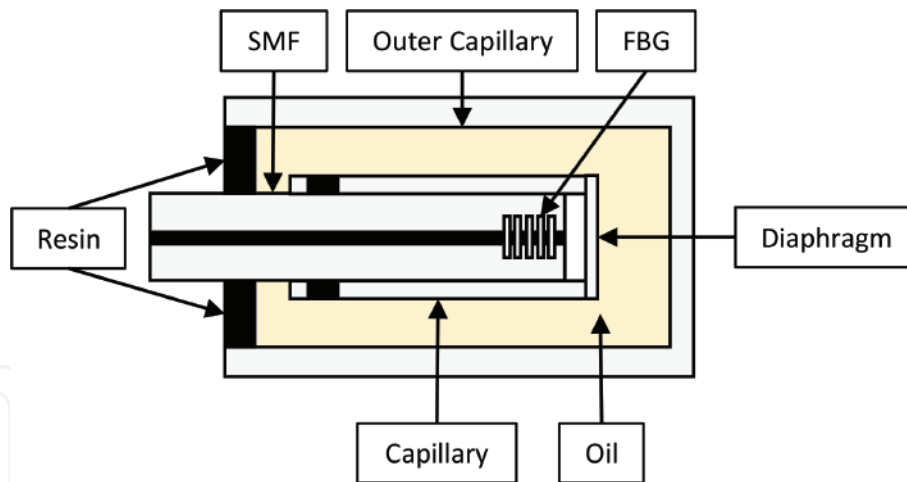


Figure 8.
Schematic of oil-filled EFPI sensor based on Poeggel et al. [34].

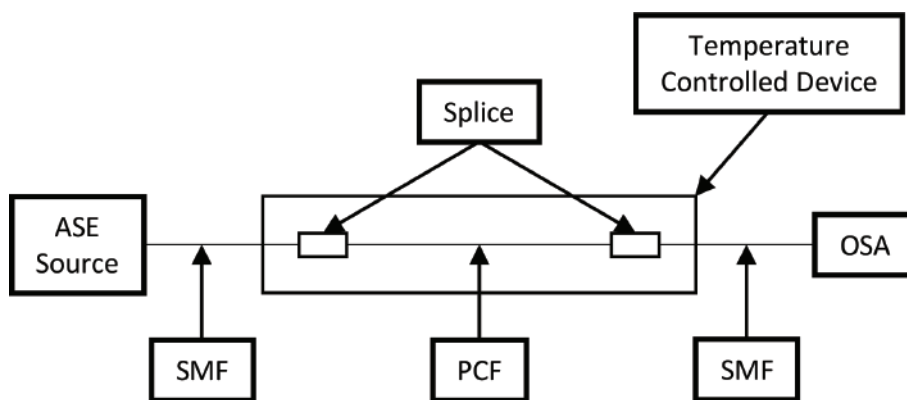


Figure 9.
Schematic of an inline PCF sensor based on Qiu et al. [37].

been a contributing factor to bubble formation. Another potential application of the sensor proposed by Poeggel et al. [34] is use of an ionising radiation sensitive fluid whereby the temperature response varies with exposure to ionising radiation.

4.2 Mach-Zehnder interferometer type sensors

Qiu et al. [37] presented a temperature sensor based on a non-polarimetric PCF, where the sensor was created by splicing a length of commercial single mode (LMA-8) [49] between two lengths of SMF-28. During construction, isopropanol was infused into the non-polarimetric PCF micro-holes by capillary effect, with the PCF subsequently fused between the SMFs. LMA-8 PCF was chosen due to having a diameter equal to that of the SMF-28, this reduced potential complications involved in the splicing process, care was also taken to minimise collapsing of the fibre air holes. Thermo-optic coefficients (TOCs) for the isopropanol and silica are $-4.5 \times 10^{-4}/\text{K}$ and $8.6 \times 10^{-6}/\text{K}$ respectively. A schematic for the sensor is provided in **Figure 9**, where an amplified spontaneous emission source (ASE) was used. As light entered from the SMF into the PCF, cladding and core modes propagated at different rates before recombining at the second splice point, this process introduced a phase difference which was observed to be temperature dependant. Akin to the designs of several other fluid-filled inline sensors, this sensor also relied on modifying the core and cladding mode TOCs in order to maximise temperature sensitivity. The sensor was tested in a temperature controlled device over temperatures ranging from 296.85–339.25 K. Blue-shifting of the two tracked waveform dips was

observed. A sample of how these waveforms may appear is presented in **Figure 10**. Temperature sensitivities were reported as -133 and -166 pm/K respectively. While this was an order of magnitude improvement over previously published works [50–52] it was significantly less sensitive when compared to the design of Qian et al. [44], indicating that exploiting the birefringent nature of PCFs may be highly beneficial in the development of inline PCF sensors.

Wang et al. [38] presented a fluid-filled PCF-based modal interferometer (PCFMI). The air holes of the PCF were filled with an oil provided by Cargille Laboratories Inc. (Cedar Grove, NJ, USA) (TOC = $-3.37 \times 10^{-4}/\text{K}$). The system design was similar to that of Qiu et al. [37]. That said however, the operation has similarities to that of Wang et al. [41] with the interference of LP₀₁ and LP₁₁ modes at the second splicing (recombination) point. Simulation suggested that temperature sensitivity increased proportionally with the ratio of filled to unfilled PCF, and that for constant filling ratio the sensitivity increased with increasing wavelength. It was reported that the latter was due to larger mode field areas of the longer wavelengths. Validation experiments were carried out at three filling ratios ($k = 0.256, 0.282, 0.476$) over a temperature range of 298.15–355.15 K. Results were in agreement with theoretical prediction, transmission spectra blue-shifted with increasing temperature, and the largest filling ratio ($k = 0.476$) resulted in the highest temperature sensitivity. Similarly, longer wavelengths resulted in increased sensitivity with a peak value of -340 pm/K at 1480 nm. Another benefit of the proposed sensor type is the linear response to straining, once matrix values were determined, the wavelength shifts may be used to produce temperature and strain measurements simultaneously. The matrix for the sensor presented by Wang et al. is provided by Eq. (7) where S_T and S_ϵ are the temperature and strain sensitivities respectively. A and B are the two waveform dips which were monitored.

$$\begin{bmatrix} \Delta T \\ \Delta \epsilon \end{bmatrix} = \begin{bmatrix} S_{T,A} & S_{\epsilon,A} \\ S_{T,B} & S_{\epsilon,B} \end{bmatrix}^{-1} \begin{bmatrix} \Delta \lambda_A \\ \Delta \lambda_B \end{bmatrix} \quad (7)$$

Wang et al. [41] presented an ultra-high resolution PCF sensor which had a single liquid filled cladding hole. In the precision filling of the hole, an initial 10 μm end cap was placed on the PCF, after which a hole was precision drilled into the desired PCF hole using a femtosecond laser (FSL). A Cargille Laboratories Inc. immersion oil with a TOC of -3.89×10^{-4} was introduced via capillary effect. The filled region of PCF was subsequently reduced incrementally by ~ 1 cm until a coherent resonant dip was present. Experimental results between 307.15 and 308.55 K indicated exceptional sensitivity at 54.3 nm/K. Linearity of the results was not provided. Numerical comparison was carried out in Comsol Multiphysics where

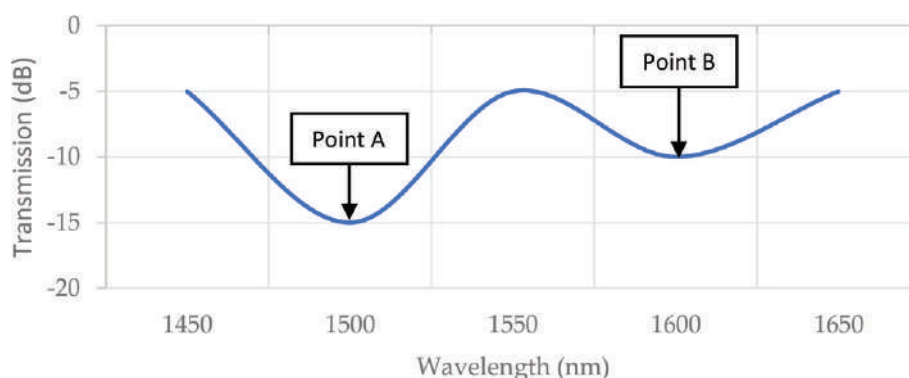


Figure 10.
 Representation of how two waveform dips may appear in a transmission spectrum.

the fibre and liquid rod core modes were compared. Results indicated coupling only occurred between the respective LP_{01} modes, where the coupling wavelength shifted by 292 nm between 303.15 and 308.15 K this giving a projected sensitivity of 58.4 nm/K. While predicted sensitivity largely agreed with experimental observations, the location of the dip did not. It was determined that this was predominantly due to uncertainty surrounding the refractive index of the immersion oil, as it had a tolerance of ± 0.002 , where an error of 0.001 led to a 150 nm wavelength shift.

Liang et al. [42] reported the first double-filled PCF sensor, with the two fluid rods having varied optical properties, both immersion oils were provided by Cargille Laboratories Inc. The first had a refractive index (RI) of 1.466 with a TOC of -3.91×10^{-4} and the second 1.500 with a TOC of -4.01×10^{-4} respectively. Owing to energy differences the PCF LP_{11} core mode was neglected. Finite element analysis indicated an interaction existed between LP_{01} (core)– LP_{01} (rod 1), and LP_{01} (core)– LP_{11} (rod 2). This indicated two waveform dips would be present in the transmission spectrum. Furthermore rod 1 displayed red-shift with increasing temperature with the converse being true of rod 2. As the two liquid rods were relatively far apart geometrically, there was no reported interaction. Temperature response was recorded between 325.15 and 327.15 K in increments of 0.2 K. Dip sensitivities were recorded as being 42.818 and -11.343 nm/K with linearities of $R^2 = 0.99951$ and 0.99935 , thus indicating the sensor had extremely high sensitivity. A highly sensitive strain response was also reported. Force on the fibre was increased from 0.218 to 0.855 N in increments of 0.049 N, with strain sensitivities being -38.041 and 8.702 pm/ $\mu\epsilon$. Linearities were $R^2 = 0.99869$ and 0.99495 .

Xu et al. [39] utilised a thin core fibre (TCF) rather than PCF in the development of their sensor. By immersing the TCF in a Cargille Laboratories Inc. immersion oil and sealing the PCF within a capillary, the influences of external refractive indices was eliminated. The TCF was approximately 20 mm long with the protective capillary 40 mm long. A schematic of the sensor is given in **Figure 11**. Similar to PCF style temperature sensors, there was a resonant dip in the transmission spectrum, which was located at 1561.7 nm for the unfilled sensor. Temperature was modulated on an unspecified thermoelectric cooler, which could be controlled to 0.1 K resolution in the temperature range 288.15–318.15 K. Results were in good agreement with other published works, where a temperature sensitivity of 9.0 pm/K was recorded with a sensor linearity of $R^2 = 0.9957$.

The introduction of immersion oil (TOC = $-3.95 \times 10^{-4}/K$) and capillary resulted in higher temperatures moving the resonance dip to a shorter wavelength, i.e. blue-shift, this being the converse of the bare TCF Mach-Zehnder Interferometer (TCFMI). Experimental results indicated that introduction of the immersion oil

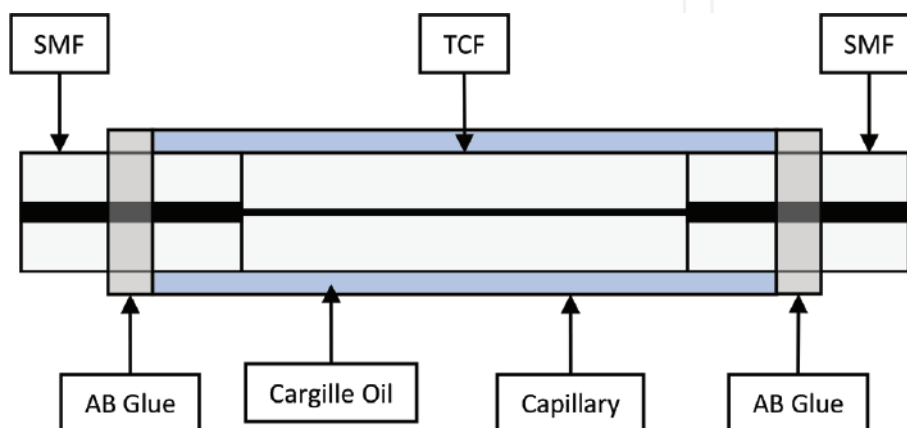


Figure 11.
Schematic of sensor based on Xu et al. [39].

as a sealing fluid increased the temperature sensitivity of the interferometer $>250\times$ compared to the baseline at -2.3 nm/K. Heating and cooling the sensor showed repeatable results with the fitted polynomial having an $R^2 = 0.999$. It should be noted however at higher temperatures, the sensitivity decreased and the fitting error increased. Peak resolution was reported at 283.15 K as 0.008 K with an OSA resolution of 0.2 pm.

Xu et al. [39] went further to quantify the influence of strain on the sensor by measuring the temperature responses of a mechanically strained bare TCFMI, and an air-sealed TCFMI. Results indicated that the resonance-dip blue shifted with strain on the bare TCFMI, and the air sealed TCFMI appeared relatively temperature insensitive. The work concluded on the point of the sensitivity being primarily driven by the sealing fluid's thermo-optic coefficient. Again, however, the sensor required transmission of the light in order to be used, thus eliminating its potential to be used as a point sensor.

4.3 Sagnac interferometer type sensors

Qian et al. [44] presented an alcohol filled temperature sensor based on a highly birefringent photonic crystal fibre (HiBi-PCF) within a fibre loop mirror (FLM) as illustrated in **Figure 12**, the light source used was a super-luminescent light emitting diode (SLED). Owing to the birefringence of the HiBi-PCF, the counter-propagating waves caused by the 3 dB coupler have an optical path difference at recombination. Two resonant dips manifested in the transmission spectrum at 293.15 K, these being present at 1455.8 and 1549.8 nm. The sensor was tested in two conditions within an unspecified controlled temperature chamber. The first of these increasing from 293.15 to 307.15 K and the latter reducing the temperature from 293.15 to 281.15 K with the two resonant dips' responses being monitored. Measurement linearities were $R^2 = 0.9995$ and $R^2 = 0.9997$ respectively. Measured sensitivities were 6.2 and 6.6 nm/K compared to the theoretical values of 6.1 and 6.5 nm/K.

Cui et al. [45] proposed an SI type sensor similar in construction to that of Qian et al. [44]. The study conducted, however, went further in an effort to quantify the influence of selective hole filling in the PCF versus non-selective filling. Further to this, the length of PCF and hole fill ratio were explored. Simulations of no infiltration, all holes filled, small holes filled, and big holes filled were carried out; with the birefringence sensitivity to infiltrating liquid being monitored. While all three liquid filled cases indicated a reduced PCF birefringence, the 'big holes filled'

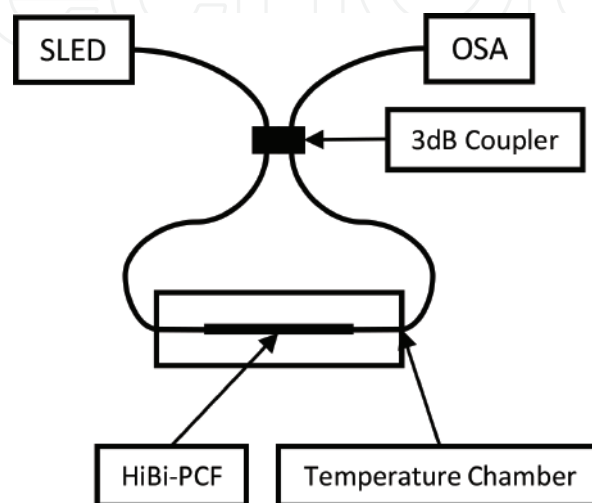


Figure 12.
Schematic of HiBi-PCF sensor based on Qian et al. [44].

condition resulted in the highest temperature sensitivity, with a birefringence change of 27% as liquid refractive index was varied from 1.33 to 1.36. Dissimilar to the selective collapsing and cleaving method employed by Peng et al. [40] Cui et al. [45] offered a simplistic method of sealing the outer holes by introducing a micro-droplet of glue to the fibre face while monitoring with a microscope. It was claimed that the process could be conducted in under a minute with repeatable results after minimal training. During experimentation, water was used in place of ethanol due to the high coefficient of thermal expansion, and reduced tendency to evaporate. The sensor indicated a good sensitivity of -2.58 nm/K with a linearity of $R^2 = 0.9991$. The OSA used to conduct the experiment had a resolution of 0.02 nm thus giving the sensor a resolution in the region of 7.75 mK. Accounting for the length of liquid filled PCF, results similar to that of Wang et al. [38] indicated increasing the ratio of filled to unfilled PCF increased temperature sensitivity.

4.4 Similar sensors

While one could consider liquid crystal based sensors in a similar category to those above, the authors wish to express they fall outside the remit of this chapter. However should the reader wish to explore these technologies, Windhorn and Cain [25] provides a good starting point. Several recent works exploring the use of liquid crystal thermometry using PCFs have also been published [53–55]. Wolinski et al. presented a multi-faceted liquid crystal PCF which was capable of temperature, electric field, and hydrostatic pressure detection [56].

5. Conclusions

The remit of this review was to address current state-of-the-art LiF-OFTSs presented in literature. The optical fibre sensors examined were based on the principles of extrinsic Fabry-Perot interferometers, Mach-Zehnder interferometers and Sagnac interferometers. While sensitivities varied to an extent, they each presented performance equivalent to, or better than, reported electrical sensors. As noted in other reviews of optical fibre sensing such as that of Lee [57] and Poeggel et al. [58] optical fibre sensors had numerous additional advantages over their electronic counterparts such as immunity to EMI, small form factor, along with distributed and multiplexed sensing capability. Perhaps encouragingly, the commercial marketplace for optical fibre sensors appears to have matured significantly since the publication of Lee's review [57]. A driving factor in this will likely have been the coupled high resolution and fast response times, which are generally sub-Kelvin and sub-second respectively.

While FBGs remain the predominant method of temperature sensing, EFPI sensors have gained momentum in the commercial arena with companies such as FISO & Opsens offering varied ranges, sensitivities and sampling rates, indicating that they are slowly gaining favour in engineering and biomedical applications. That said however, MZI based temperature sensors were the more reported sensor type in literature. From this review it was obvious that while several ultra-high resolution liquid filled temperature sensors have been developed there is still scope for significant work to be carried out to improve their performance and stimulate widespread commercial deployment.

Considering that a significant portion of optical fibre sensor research has been focused towards biomedical applications in recent years, it is understandable that a market for inline sensors may not exist, that said however it may bode well for the

Company	Proximion	OPSENS	RJC Enterprises
Sensor name	WISTHEAT [60]	OTG-MPK5 [61]	N/A [62]
Sensor type	FBG	GaAs Crystal	EFPI
Min. temperature	228.15 K	293.15 K	288.15 K
Max. temperature	523.15 K	318.15 K	328.15 K
Resolution	70 mK(0.5 pm OSA)	10 mK	100 mK

Table 2.
 Commercially available optical fibre temperature sensors.

designs of Chen et al. [46] and Poeggel et al. [34]. Another factor which has often been overlooked is the filling liquid properties, the majority of MZI sensors used an immersion oil provided by Cargille Laboratories Inc. and one reported using isopropanol. While the isopropanol may act as an irritant, the immersion oil used may be toxic if swallowed or inhaled, such as that of the Series AA [59]. It is also known to be damaging to waterways, thus indicating strict environmental controls require consideration. That said however, monitoring of industrial equipment using this method is more than plausible with the potential to use multiple PCFs on a single fibre to provide distributed sensing, **Table 2** lists example commercially available OFTSs. While the sensors are not of a liquid filled construction, they indicate the minimum required performance of any potential liquid filled sensor in order to potentially be commercially competitive.

Acknowledgements

This work was supported by the Science Foundation Ireland grant number: 15/CDA/3598

Conflict of interest

The authors wish to declare no conflict of interest.

Nomenclature

Symbol	Name	Unit
D	Flexural rigidity	Pa.m ³
E	Young's modulus	N/m ²
P	Pressure	N/m ²
Q	Heat	J
R	Outer radius	m
S _T	Temperature sensitivity	/K
S _ε	Strain sensitivity	-
T	Temperature	K
T ₀	Initial temperature	K
c	Specific heat capacity	J/kg.K
h	Thickness	m
n _{eff}	Effective refractive index	-
r	Reference radius	m

t	Time	s
z	Deflection	m
Λ	Bragg grating pitch	m
α_n	Thermal coefficient of refractive index	/K
α_d	Thermal coefficient of thickness	/K
ε	Strain	-
λ	Wavelength	m
λ_B	Bragg wavelength	m
ν	Poisson's ratio	-

IntechOpen

Author details

Fintan McGuinness¹, Gabriel Leen¹, Elfed Lewis¹, Gerard Dooly², Daniel Toal² and Dinesh Babu Duraibabu^{2*}

1 Optical Fibre Sensors Research Centre, University of Limerick, Limerick, Ireland

2 Centre for Robotics and Intelligent Systems, University of Limerick, Limerick, Ireland

*Address all correspondence to: dineshbabu.duraibabu@ul.ie

IntechOpen

© 2018 The Author(s). Licensee IntechOpen. This chapter is distributed under the terms of the Creative Commons Attribution License (<http://creativecommons.org/licenses/by/3.0>), which permits unrestricted use, distribution, and reproduction in any medium, provided the original work is properly cited. 

References

- [1] Valleriani M. Galileo Engineer. In: Cohen RS, Renn J, Gavroglu K, editors. *Boston Studies in the Philosophy of Science*. Vol. 269. Dordrecht: Springer Science + Business Media; 2010. pp. 155-165
- [2] McGee TD. *Principles and Methods of Temperature Measurement*. 1st ed. New York: Wiley-Interscience; 1988
- [3] Sverdrup H, Johnson MW, Fleming RH. *The Oceans, Their Physics, Chemistry, and General Biology*. New York: Prentice-Hall Inc.; 1942 [Internet]. Available from: <http://ark.cdlib.org/ark:/13030/kt167nb66r/>
- [4] Sarma U, Boruah PK. Design and development of a high precision thermocouple based smart industrial thermometer with on line linearization and data logging feature. *Measurement: Journal of the International Measurement Confederation*. 2010; **43**(10):1589-1594. DOI: 10.1016/j.measurement.2010.09.003 [Internet]
- [5] Yang F, Li G, Yang J, Wang Z, Han D, Zheng F, et al. Measurement of local temperature increments induced by cultured HepG2 cells with micro-thermocouples in a thermally stabilized system. *Scientific Reports*. 2017; **7**(1): 1-12. DOI: 10.1038/s41598-017-01891-1 [Internet]
- [6] Resistor Guide, NTC thermistor Resistor Guide [Internet]. Available from: <http://www.resistorguide.com/ntc-thermistor/> [Accessed: 25-07-2018]
- [7] Clow GD, Saltus RW, Waddington ED. A new high-precision borehole-temperature logging system used at GISP2, Greenland, and Taylor Dome, Antarctica. *Journal of Glaciology*. 1996; **42**(142):576-584. DOI: 10.3189/S0022143000003555 [Internet]. Available from: https://www.cambridge.org/core/product/identifier/S0022143000003555/type/journal%7B%5C_%7Darticle
- [8] Hanna Instruments, Ultra-Fast Penetration K-Type Thermocouple Probe with Handle [Internet]. 2018. Available from: <https://hannainst.com/hi766c1-ultra-fast-penetration-%20k-type-thermocouple-probe-with-handle.html> [Accessed: 27-06-2018]
- [9] Hammond DL, Benjaminson A. The linear quartz thermometer—A new tool for measuring absolute and difference temperatures. *Hewlett-Packard Journal*. 1965; **16**(7):1-7 [Internet]. Available from: ftp://dns.soest.hawaii.edu/bhowe/outgoing/20120920%7B%5C_%7DITU%7B%5C_%7DParis/HPJ-1965-03.pdf
- [10] Lerch BA, Nathal MV. *Thermocouple Calibration and Accuracy in a Materials Testing Laboratory*. TM-2002-211507. Ohio: Glenn Research Centre, NASA; 2002
- [11] IEEE Standards Association. IEEE Std 2700TM-2014, IEEE Standard for Sensor Performance Parameter Definition. New York: IEEE; 2014. DOI: 10.1109/70 IEEESTD.2014.6880296
- [12] Rhoades R, Pflanzner R. In: Bachman C, editor. *Human Physiology*. 4th ed. Pacific Grove: Thomson Learning Inc.; 2003
- [13] Omega. TCC type correltaion. Tech. Rep. type C [Internet]. pp. 4-5. Available from: <https://www.omega.com/techref/pdf/z202.pdf>
- [14] Buckton G, Russell SJ, Beezer AE. Pharmaceutical calorimetry: A selective review. *Thermochimica Acta*. 1991; **193** (C):195-214. DOI: 10.1016/0040-6031(91)80184-K
- [15] Rossi S. Brain temperature, body core temperature, and intracranial

- pressure in acute cerebral damage. *Journal of Neurology, Neurosurgery & Psychiatry*. 2001;**71**(4):448-454. DOI: 10.1136/jnnp.71.4.448 [Internet]
- [16] NASA. Heat Transfer [Internet]. 2018. Available from: <https://wright.nasa.gov/airplane/heat.html> [Accessed: 12-07-2018]
- [17] Burgett RR, Massoll RE, Van Uum DR. Relationship between spark plugs and engine-radiated electromagnetic interference. *IEEE Transactions on Electromagnetic Compatibility*. 1974; **EMC-16**(3):160-172. DOI: 10.1109/TEMC.1974.303355
- [18] GE Oil & Gas. Platinum Resistance Thermometer (PRT) [Internet]. 2012. Available from: https://geoilandgas.com/sites/geog/files/prt%7B%5C_%7Dplatinum%7B%5C_%7Dresistance%7B%5C_%7Dthermometer.pdf [Accessed: 27-06-2018]
- [19] Hanna Instruments. K-Thermometers [Internet]. 2018. Available from: https://hannainst.com/downloads/dl/file/id/1637/manhi%7B%5C_%7D93530%7B%5C_%7D531%7B%5C_%7D532.pdf [Accessed: 27-06-2018]
- [20] Shenzhen Senstech Electronic Technology Company Ltd. Waterproof Temperature Sensor DS18B20 Programmable Resolution 1-Wire Digital Thermometer [Internet]. 2018. Available from: https://www.alibaba.com/product-detail/Waterproof-Temperature-Sensor-DS18B20-Programmable-%20Resolution%7B%5C_%7D1898805574.html?spm=a2700.7724857.main07.31.40cb3892YwvGzX [Accessed: 27-06-2018]
- [21] Castellon J, Paez G, Strojnik M. Remote temperature sensor employing erbium-doped silica fiber. *Infrared Physics and Technology*. 2002;**43**(3-5): 219-222. DOI: 10.1016/S1350-4495(02)00142-1
- [22] Zhang H, Jiang Q, Wang BY, Wang JJ. Monitoring diesel engine parameters based on FBG probe. *Optoelectronics Letters*. 2016;**12**(5):0384-0388. DOI: 10.1007/s11801-016-6162-7
- [23] Pinet É, Hamel C, Glišić B, Inaudi D, Miron N. Health monitoring with optical fiber sensors: from human body to civil structures. In: Kundu T, editor. *SPIE Proceedings*. San Diego: SPIE; 19 May 2007;**6532**:653219-653230. DOI: 10.1117/12.715186. [Internet]. Available from: <http://proceedings.spiedigitallibrary.org/proceeding.aspx?articleid=1337730%20;> <http://proceedings.spiedigitallibrary.org/proceeding.aspx?doi=10.1117/12.715186>
- [24] Corning Incorporated. Frequently Asked Questions on Fiber Reliability [Internet]. 2016. Available from: <https://www.corning.com/media/worldwide/coc/documents/Fiber/RC-%20White%20Papers/WP5082%203-31-2016.pdf>
- [25] Windhorn TH, Cain CA. Optically active binary liquid crystal thermometry. *IEEE Transactions on Bio-Medical Engineering*. 1979;**26**(3): 148-152 [Internet]. Available from: <http://www.ncbi.nlm.nih.gov/pubmed/521025>
- [26] Poeggel S, Tosi D, Duraibabu D, Kelly J, Munroe M, Leen G, et al. Novel diaphragm microfabrication techniques for high-sensitivity biomedical fiber optic Fabry-Perot interferometric sensors. In: *Proceedings of SPIE—The International Society for Optical Engineering*. Vol. 9098. 2014. p. 909813. DOI: 10.1117/12.2050500 [Internet]. Available from: <http://proceedings.spiedigitallibrary.org/proceeding.aspx?doi=10.1117/12.2050500>
- [27] Nakazaki Y, Yamashita S. Fast and wide tuning range wavelength-swept fiber laser based on dispersion tuning and its application to dynamic FBG

- sensing. *Optics Express*. 2009;**17**(10): 8310. DOI: 10.1364/OE.17.008310 [Internet]. Available from: <https://www.osapublishing.org/abstract.cfm?URI=oe-17-10-8310>
- [28] Poeggel S, Duraibabu D, Tosi D, Leen G, Lewis E, McGrath D, et al. Differential *in vivo* urodynamic measurement in a single thin catheter based on two optical fiber pressure sensors. *Journal of Biomedical Optics*. 2015;**20**(3):037005. DOI: 10.1117/1.JBO.20.3.037005 [Internet]. Available from: <http://biomedicaloptics.spiedigitallibrary.org/article.aspx?doi=10.1117/1.JBO.20.3.037005>
- [29] Sellnau MC, Matekunas FA, Battiston PA, Chang C-F, Lancaster DR. Cylinder-Pressure-Based Engine Control Using Pressure-Ratio-Management and Low-Cost Non-Intrusive Cylinder Pressure Sensors no. 724 [Internet] . 2000. DOI: 10.4271/2000-01-0932. Available from: <http://papers.sae.org/2000-01-0932/>
- [30] Kasper JC, Wiggenhorn M, Resch M, Friess W. Implementation and evaluation of an optical fiber system as novel process monitoring tool during lyophilization. *European Journal of Pharmaceutics and Biopharmaceutics*. 2013;**83**(3):449-459. DOI: 10.1016/j.ejpb.2012.10.009 [Internet]
- [31] Hong CY, Zhang YF, Zhang MX, Leung LMG, Liu LQ. Application of FBG sensors for geotechnical health monitoring, a review of sensor design, implementation methods and packaging techniques. *Sensors and Actuators, A: Physical*. 2016;**244**:184-197. DOI: 10.1016/j.sna.2016.04.033 [Internet]
- [32] Gassino R, Pogliano J, Perrone G, Vallan A. Issues and characterization of fiber Bragg grating based temperature sensors in the presence of thermal gradients. *Measurement: Journal of the International Measurement Confederation*. 2018;**124**(January): 15-19. DOI: 10.1016/j.measurement.2018.03.049 [Internet]
- [33] Benham P, Crawford R, Armstrong C. *Mechanics of Engineering Materials*. 2nd ed. Harlow: Prentice-Hall Inc.; 1996
- [34] Poeggel S, Duraibabu D, Dooly G, Lewis E, Leen G. Novel ultrahigh resolution optical fibre temperature sensor. In: Lewis E, editor. *Proceedings of SPIE—The International Society for Optical Engineering*. Vol. 9916. 2016. p. 991605. DOI: 10.1117/12.2236155 [Internet]. Available from: <http://proceedings.spiedigitallibrary.org/proceeding.aspx?doi=10.1117/12.2236155>
- [35] Gao X, Yang M, Peng J, Lv D. Miniature fiber-optic temperature sensor based on optical coating interference. *Optik—International Journal for Light and Electron Optics*. 2017;**130**:1014-1020. DOI: 10.1016/j.ijleo.2016.11.114 [Internet]. Available from: <http://linkinghub.elsevier.com/retrieve/pii/S0030402616314516>
- [36] Hecht E. *Optics*. 5th ed. Harlow: Pearson Education Limited; 2014
- [37] Qiu S-j, Chen Y, Xu F, Lu Y-q. Temperature sensor based on an isopropanol-sealed photonic crystal fiber in-line interferometer with enhanced refractive index sensitivity. *Optics Letters*. 2012;**37**(5):863-865. DOI: 10.1364/OL.37.000863 [Internet]. Available from: <http://www.ncbi.nlm.nih.gov/pubmed/22378419>
- [38] Wang S, Liu Y-g, Wang Z, Han T, Xu W, Wang Y, et al. Intermodal interferometer based on a fluid-filled two-mode photonic crystal fiber for sensing applications. *Applied Optics*. 2013;**52**(14):3166-3171. DOI: 10.1364/AO.52.003166 [Internet]. Available from: <http://ao.osa.org/abstract.cfm?URI=ao-52-14-3166>
- [39] Xu B, Li J, Li Y, Xie J, Dong X. Liquid seal for temperature sensing with

fiber-optic refractometers. *Sensors* (Switzerland). 2014;**14**(8):14873-14884. DOI: 10.3390/s140814873

[40] Peng Y, Hou J, Zhang Y, Huang Z, Xiao R, Lu Q. Temperature sensing using the bandgap-like effect in a selectively liquid-filled photonic crystal fiber. *Optics Letters*. 2013;**38**(3): 263-265. DOI: 10.1364/OL.38.000263 [Internet]. Available from: <http://www.ncbi.nlm.nih.gov/pubmed/23381405>

[41] Wang Y, Yang M, Wang DN, Liao CR. Selectively infiltrated photonic crystal fiber with ultrahigh temperature sensitivity. *IEEE Photonics Technology Letters*. 2011;**23**(20):1520-1522

[42] Liang H, Zhang W, Geng P, Liu Y, Wang Z, Guo J, et al. Simultaneous measurement of temperature and force with high sensitivities based on filling different index liquids into photonic crystal fiber. *Optics Letters*. 2013;**38**(7): 1071-1073. DOI: 10.1364/OL.38.001071 [Internet]. Available from: <http://www.ncbi.nlm.nih.gov/pubmed/23546247>

[43] Napolitano F. Fiber-Optic Gyroscopes Key Technological Advantages. Saint-Germain en Laye, Tech. Rep. [Internet]. 2010. Available from: <https://www.ixblue.com/m/publication/fog-key-advantages.pdf>

[44] Qian W, Zhao C-L, He S, Dong X, Zhang S, Zhang Z, et al. High-sensitivity temperature sensor based on an alcohol-filled photonic crystal fiber loop mirror. *Optics Letters*. 2011;**36**(9):1548. DOI: 10.1364/OL.36.001548. arXiv: 0604155 [physics]. [Internet]. Available from: <https://www.osapublishing.org/abstract.cfm?URI=ol-36-9-1548>

[45] Cui Y, Shum PP, Hu DJJ, Wang G, Humbert G, Dinh XQ. Temperature sensor by using selectively filled photonic crystal fiber Sagnac interferometer. *IEEE Photonics Journal*. 2012;**4**(5):1801-1808. DOI: 10.1109/JPHOT.2012.2217945

[46] Qing Chen M, Zhao Y, Xia F, Peng Y, Jie Tong R. High sensitivity temperature sensor based on fiber air-microbubble Fabry-Perot interferometer with PDMS-filled hollow-core fiber. *Sensors and Actuators, A: Physical*. 2018;**275**:60-66. DOI: 10.1016/j.sna.2018.03.044 [Internet]

[47] Poeggel S, Duraibabu D, Kalli K, Leen G, Dooly G, Lewis E. Recent improvement of medical optical fibre pressure and temperature sensors. *Biosensors*. 2015;**5**(3):432-449. DOI: 10.3390/bios5030432 [Internet]. Available from: <http://www.mdpi.com/2079-6374/5/3/432/>

[48] Sensortec B. Data sheet. Tech. Rep. [Internet]. 2009. Available from: <https://www.sparkfun.com/datasheets/Components/General/BST-BMP085-DS000-05.pdf>

[49] NKT Photonics. LMA-8. Tech. Rep. [Internet]. Available from: <https://www.nktphotonics.com/wp-content/uploads/sites/3/2015/01/LMA-8.pdf>

[50] Jha R, Villatoro J, Badenes G, Pruneri V. Refractometry based on a photonic crystal fiber interferometer. *Optics Letters*. 2009;**34**(5):617. DOI: 10.1364/OL.34.000617 [Internet]. Available from: <https://www.osapublishing.org/abstract.cfm?URI=ol-34-5-617>

[51] Qiu S-j, Chen Y, Kou J-l, Xu F, Lu Y-q. Miniature tapered photonic crystal fiber interferometer with enhanced sensitivity by acid microdroplets etching. *Applied Optics*. 2011;**50**(22):4328. DOI: 10.1364/AO.50.004328 [Internet]. Available from: <https://www.osapublishing.org/abstract.cfm?URI=ao-50-22-4328>

[52] Gong H, Chan CC, Zhang YF, Wong WC, Dong X. Miniature refractometer based on modal interference in a hollow-core photonic crystal fiber with

- collapsed splicing. *Journal of Biomedical Optics*. 2011;**16**(1):017004. DOI: 10.1117/1.3527259 [Internet]. Available from: <http://biomedicaloptics.spiedigitallibrary.org/article.aspx?doi=10.1117/1.3527259>
- [53] Wolinski TR, Szaniawska K, Ertman S, Lesiak P, Domanski AW, Dabrowski R, et al. Influence of temperature and electrical fields on propagation properties of photonic liquid-crystal fibres. *Measurement Science and Technology*. 2006;**17**(5):985-991. DOI: 10.1088/0957-0233/17/5/S08 [Internet]. Available from: <http://stacks.iop.org/0957-0233/17/i=5/a=S08?key=crossref.f9489a53384ab98a6cd800efb7324542>
- [54] Wei L, Eskildsen L, Weirich J, Scolari L, Alkeskjold TT, Bjarklev A. Continuously tunable all-in-fiber devices based on thermal and electrical control of negative dielectric anisotropy liquid crystal photonic bandgap fibers. *Applied Optics*. 2009;**48**(3):497. DOI: 10.1364/AO.48.000497 [Internet]. Available from: <https://www.osapublishing.org/abstract.cfm?URI=ao-48-3-497>
- [55] Miao Y, Liu B, Zhang K, Liu Y, Zhang H. Temperature tunability of photonic crystal fiber filled with Fe₃O₄ nanoparticle fluid. *Applied Physics Letters*. 2011;**98**(2):21103. DOI: 10.1063/1.3540647
- [56] Wolinski T, Czaplak A. Photonic liquid crystal fibers for sensing applications. *IEEE Transactions on Instrumentation and Measurement*. 2008;**57**(8):1796-1802. DOI: 10.1109/TIM.2008.922077 [Internet]. Available from: http://ieeexplore.ieee.org/xpls/abs%7B%5C_%7Dall.jsp?arnumber=4510764
- [57] Lee B. Review of the present status of optical fiber sensors. *Optical Fiber Technology*. 2003;**9**(2):57-79. DOI: 10.1016/S1068-5200(02)00527-8
- [58] Poeggel S, Tosi D, Duraibabu D, Leen G, McGrath D, Lewis E. Optical fibre pressure sensors in medical applications. *Sensors*. 2015;**15**(7):17115-17148. DOI: 10.3390/s150717115 [Internet]. Available from: <http://www.mdpi.com/1424-8220/15/7/17115/>
- [59] Cargille Laboratories Inc. Cargille Refractive Index Liquid Series AA nD = 1.400–1.459 Safety Data Sheet [Internet]. Available from: http://www.cargille.com/SDS%7B%5C_%7DRI%7B%5C_%7DSeries%7B%5C_%7DAA.pdf
- [60] Proximion. High Temperature FBG Sensor for Harsh Environment [Internet]. Available from: https://static1.squarespace.com/static/54690ca0e4b0dc0a73f1772b/t/57f752ed579fb360231dc1f4/1475826414976/Proximion%7B%5C_%7Dprodblad%7B%5C_%7DWISTHEAT%7B%5C_%7D161005.pdf [Accessed: 12-07-2018]
- [61] OpSens. OTG-MPK5 Fiber Optic Temperature Sensor, Probe and Transducer [Internet]. 2018. Available from: <https://opsens-solutions.com/products/fiber-optic-temperature-sensors/otg-mpk5/> [Accessed: 12-07-2018]
- [62] RJC Enterprises. How Our Sensors Work [Internet] 2018. Available from: <http://www.rjcenterprises.net/background.html> [Accessed: 12-07-2018]

We are IntechOpen, the world's leading publisher of Open Access books Built by scientists, for scientists

6,300

Open access books available

171,000

International authors and editors

190M

Downloads

Our authors are among the

154

Countries delivered to

TOP 1%

most cited scientists

12.2%

Contributors from top 500 universities



WEB OF SCIENCE™

Selection of our books indexed in the Book Citation Index
in Web of Science™ Core Collection (BKCI)

Interested in publishing with us?
Contact book.department@intechopen.com

Numbers displayed above are based on latest data collected.
For more information visit www.intechopen.com



Optical Fibre Long-Period Grating Sensors Operating at and around the Phase Matching Turning Point

Rebecca Yen-Ni Wong, Dora Hu Juan Juan, Morten Ibsen and Perry Ping Shum

Abstract

Optical fibres have been exploited as sensors for many years and they provide a versatile platform with a small form factor. Long-period gratings (LPGs) operating at and around the phase matching turning point (PMTP) possess some of the highest sensitivities to external perturbations in the family of LPG-based sensor devices. This type of optical fibre grating has been demonstrated as a sensor for use in a wide range of applications. In this review chapter, an overview of PMTP LPGs is presented and the key developments, findings and applications are highlighted. The fabrication considerations and sensor limitations are also discussed.

Keywords: optical fibre, fibre optics, fibre sensors, long-period gratings, phase matching turning point, turn around point

1. Introduction

Optical fibre sensors do not only have use in telecommunications but are also extremely useful in a number of sensing applications. Many fields such as medical, oil and gas, civil, automotive as well as aerospace industries (structural health monitoring) have benefitted from optical fibre grating sensors [1–4].

In-fibre gratings are known as intrinsic sensing devices and therefore the propagation of light is guided and controlled within the fibre. Fibre gratings have a perturbation with a certain periodicity which will cause the fibre properties to change. They are also relatively easy to configure, are wavelength encoded enabling stable signals, and offer a high signal-to-noise ratio. One type of in-fibre grating is the long-period grating (LPG), which Vengsarkar et al. [5, 6] were the first to introduce. LPGs typically have periods ranging from around 100 μm to around 1 mm [7]. The principle of operation consists of the forward propagating core mode coupling with one or more of the forward propagating cladding modes [8]. The coupling involves the cladding modes, which means that the evanescent field will extend into the fibre surroundings. This will cause the LPG to be affected by its local environment. Another type of in-fibre grating is the fibre Bragg grating (FBG). The FBG promotes coupling of the propagating core mode with the counter-propagating core mode. FBGs typically have sub-micron periods and will produce a peak (in reflection) at a wavelength that is able to satisfy the Bragg condition. FBGs have also been used for numerous sensing applications [9, 10], but they will not be covered in this chapter.

By appropriately selecting the period of an LPG, it is possible to ensure the core mode will couple to a cladding mode operating at the turn around point (TAP) [11], also known as the phase matching turning point (PMTP), or dispersion turning point (DTP). A feature known as the dual resonance band can also be produced in this region. This type of LPG configuration has become increasingly popular due to its ultra-high sensitivity, a property usually desirable for a sensor. Approaches employed to improve the sensing capability of LPGs have included methods such as tapering [12] and etching [13]; however this can weaken the structure of the fibre and requires more delicate handling or complicated packaging. These sensors have been successfully used for measuring parameters such as temperature [14–16], strain [14–16] and refractive index (RI) [17–20]. The properties of LPGs at PMTP can be tailored further by adding a functional nanoscale coating for chemical and gas sensing [21]. This enables users to adapt the sensor to their own needs and applications. Chemical and bio-chemical based sensors, or those that can be applied to healthcare, are attracting increasing attention as they can have a more direct impact on the wellbeing of people. However, many are still yet to be applied in real situations outside of the laboratory [2].

This chapter aims to provide a more comprehensive coverage of LPGs which operate at and around the phase matching turning point, with respect to what can be found in existing literature [22]. The typical characteristics and fabrication considerations will be discussed. This will be followed by the different applications where PMTP LPGs have been demonstrated.

2. Long-period gratings at phase matching turning point

LPGs consist of some periodic modulation in the optical fibre which causes the core mode to couple with a number of modes in the cladding, at discrete wavelengths (**Figure 1**). The modes will propagate through the fibre with the propagation constants, β_{co} and β_{cl}^M (core and M -th cladding mode, respectively) and the wavelengths are dependent upon the satisfaction of the phase matching condition, which is described as [16]:

$$\lambda = [n_{co}(\lambda) - n_{cl}^M(\lambda)]\Lambda \quad (1)$$

Where λ is the resonant wavelength, n_{co} is the effective refractive index of the propagating core mode, n_{cl}^M is the effective refractive index of the M -th cladding mode, and the Λ is the period of the LPG.

Light that couples to the fibre cladding modes is lost rapidly through scattering and absorption at the cladding and the surrounding medium interface. This is presented as a transmission spectrum, as shown in **Figure 2**, that contains one or more resonance bands with wavelengths, λ_n .

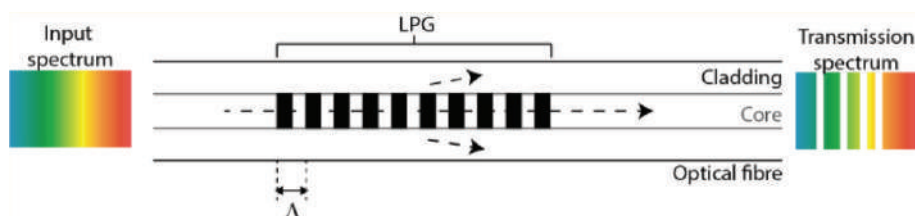


Figure 1.
Schematic diagram of an LPG.

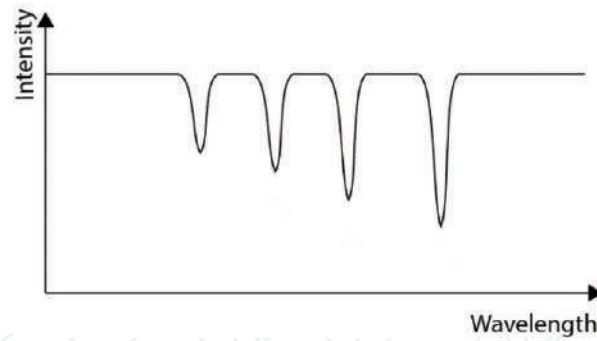


Figure 2.
 Illustration of an LPG transmission spectrum with resonance bands at discrete wavelengths.

Eq. (1) shows the resonant wavelength is dependent on the effective refractive indices of the core and cladding mode of the fibre. This central resonant wavelength and the sensitivity of an LPG is affected by the order of the coupled cladding mode; choosing the grating period, the type [23] and composition of the fibre [19], and any external perturbations can alter the coupled mode.

Optical fibre LPG structures (a three layer cylindrical waveguide consisting of the core, cladding and ambient surrounding) can be modelled using coupled mode theory [24–26]. This can be used to describe the power transmitted between the modes of the waveguides. Guided modes propagating in a fibre can be treated as linearly polarised (LP), employing the weakly guided approximation [27]; this approximates the difference between the normalised core and cladding refractive index, Δ , to be very small [24, 25, 27]:

$$\Delta = \frac{n_{co} - n_{cl}}{n_{co}} \ll 1 \quad (2)$$

The coupled mode theory equations that are used to describe the LPG can be simplified to [24]:

$$\frac{dA_{co}}{dz} = ik_{co-co} + i \sum_v \frac{m}{2} k_{cl-co}^M A_{cl}^M e^{(-i 2 \delta_{cl-co}^M z)}, \quad (3)$$

$$\sum_v \frac{dA_{cl}^M}{dz} = +i \frac{m}{2} k_{cl-co}^M A_{co} e^{(+i 2 \delta_{cl-co}^M z)} \quad (4)$$

Where A_{co} is the amplitude of the core mode along the z-axis, A_{cl}^M is the amplitude of the cladding mode along the z-axis, the z-axis is along the axis of the optical fibre, k is the coupling constant, m is the induced-index fringe modulation.

The small-detuning factor for the co-propagating modes is defined as:

$$\delta_{cl-co}^M \equiv \frac{1}{2} \left(\beta_{co} - \beta_{cl}^M - \frac{2\pi}{\Lambda} \right) \quad (5)$$

Phase matching curves of resonance wavelength against grating period of an LPG can be generated by calculating the dispersion of the modes of the core and the cladding. These sets of curves are able to predict coupling from the core to the cladding mode, and that for each cladding mode there will be a turning point [28]. Around the turning point, a single mode can be coupled at two different wavelengths simultaneously [11, 28]. **Figure 3** shows an example of phase matching curves for higher order cladding modes in the 600–1150 nm wavelength range. It

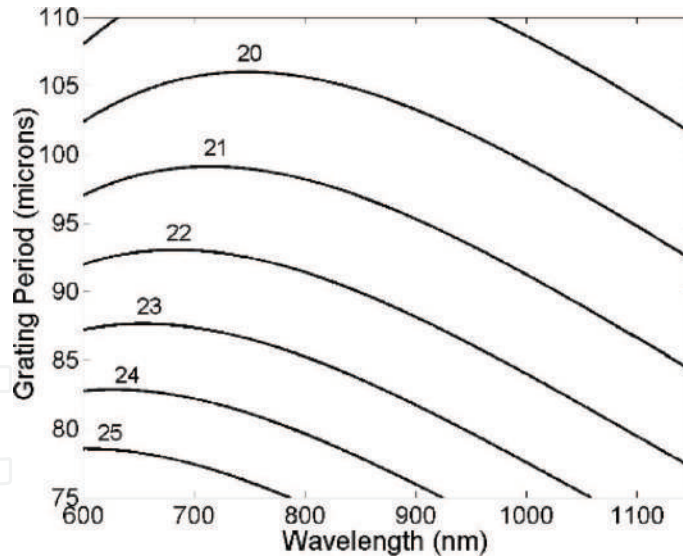


Figure 3.

Phase matching curves of the 20–25th cladding modes of an optical fibre with a cut-off wavelength of 670 nm. The relationship between the grating period and wavelength is shown. Reprinted with permission from Ref. [28], OSA.

can be observed that, at the turning point, the gradient of the curve tends to zero, $|d\Lambda/d\lambda| \rightarrow 0$ (and $|d\lambda/d\Lambda| \rightarrow \infty$). The waveguide dispersion of an LPG, expressed as $\gamma = (d\lambda/d\Lambda) \Delta n_{core}$ [29], will tend to infinity. As γ can be used to generalise the sensitivity of an LPG [11] it indicates that the transmission spectrum of an LPG that is fabricated with a period that closely matches a turning point, will have the highest sensitivity to external perturbations [11, 14]. The appearance of turning points will move towards shorter wavelengths when the cladding mode order is increased, as presented in **Figure 3**.

With increasing wavelength, the cladding mode's effective refractive index will decrease more than the effective refractive index of the core mode [15, 30]; this corresponds to the dual bands that become apparent in the LPG transmission spectrum.

Figure 4 shows how the grating period of an LPG approaching the turning point of the LP_{021} mode affects the transmission spectrum of the LP_{020} and LP_{021} cladding modes. **Figure 4(b)** shows the transmission spectrum where the period of the LPG chosen does not cut across the phase matching curve (**Figure 4(a)**) of LP_{021} at the turning point. A single resonant band develops (**Figure 4(d)**) followed by a small change in the central wavelength of the LP_{020} band as the period of the LPG hits the PMTP (**Figure 4(c)**). As the LPG crosses the turning point, the single band will split leading to the formation of two resonance bands. A much larger evolution can be seen for the LP_{021} mode when compared to the LP_{020} mode due to the much smaller gradient of the phase matching curve.

When an external perturbation is applied to the LPG, the two resonance bands of the mode around the turning point can either move towards or away from each other. This depends on the perturbation and the initial period of the LPG. The two bands respond differently to each other due to a non-symmetrical resonance [14], which may be due to modal dispersion [31]. For a 202.5 μm period LPG with dual resonance bands around the turning point, exposed to different temperatures, each band shows a sensitivity of 2.54 nm/ $^{\circ}\text{C}$ (red shifted) and 3.29 nm/ $^{\circ}\text{C}$ (blue shifted), respectively [14]. In the circumstance where the two bands shift towards each other, a single broad bandwidth band appears, similar to what is shown in **Figure 4(d)**. Under the influence of an external measurand, the coupling strength between the core mode and the cladding mode changes, altering only the amplitude of this single band and not the resonant wavelength [15].

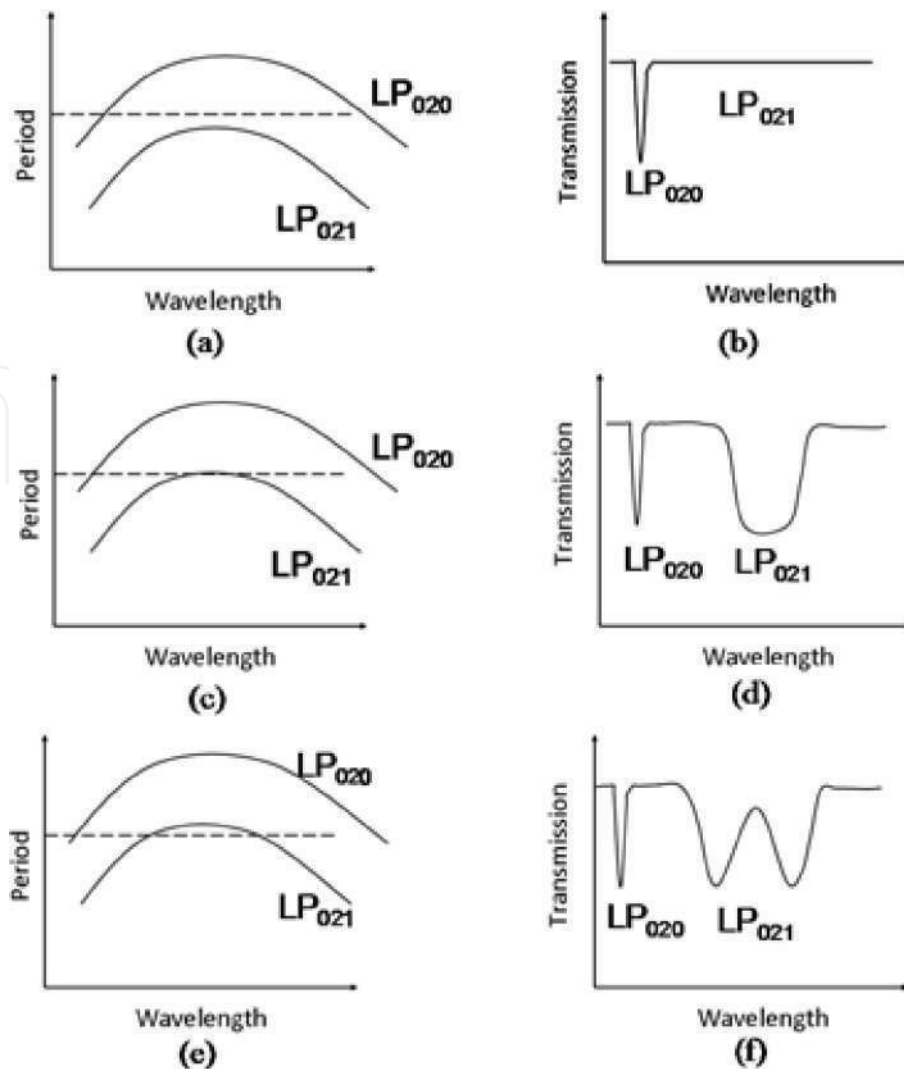


Figure 4. Illustration of the phase matching curve ((a), (c), (e)) with their corresponding transmission spectrum ((b), (d), (f)) for cladding modes LP₀₂₀ and LP₀₂₁ as coupling approaches and crosses the turning point. Korposh et al., adapted from [31]; originally published under CC BY 3.0 licence. Available from: 10.5772/52935

3. Fabrication

LPGs at PMTP can be fabricated using the same methods as those used for conventional LPGs, albeit with higher precision - the effective refractive indices of the optical fibre modes can be altered via photo-induction, or by physical deformation [7]. The refractive index can be altered using a number of different methods. Some of these include local exposure of the fibre to a UV laser [28, 32, 33, 34], CO₂ laser [35, 36], femtosecond laser [23, 37] or by electrical arc discharge [30, 38]. PMTPs have been written in conventional single mode and doped fibres [12, 11, 33, 34, 36, 39], and have been theoretically investigated using photonic crystal fibres [23]. The length of an LPG tends to range from 30 to 50 mm and have refractive index changes of around 10^{-4} [40]. Coelho et al. [41] calculated a refractive index change in the order of 2×10^{-4} and 3×10^{-4} for the core and cladding, respectively when writing an LPG in a single mode fibre using mid-infrared laser radiation. The same order of magnitude of refractive index change (4.49×10^{-4}) is also needed for femtosecond laser radiation [42].

A PMTP can also be tuned after an LPG has been fabricated, by tuning the mode coupling and effective index guiding via the means of tapering [12], UV exposure [43], with a thin film overlay [31, 28], etching [44] and radiation exposure [12].

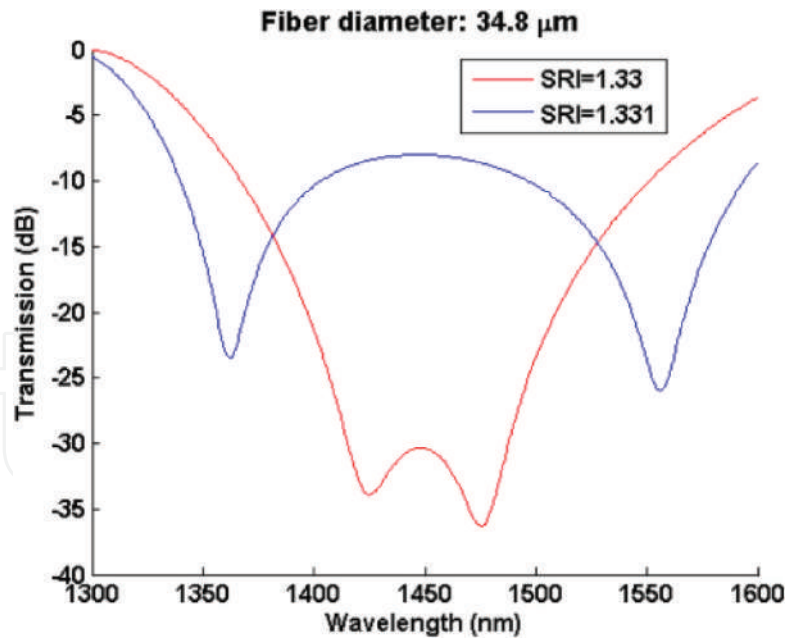


Figure 5.

Transmission spectra of a PMTP LPG with a 34.8 μm cladding diameter and 288.5 μm period, showing a large wavelength shift with a surrounding refractive index change of 0.001. SRI is surrounding refractive index. Reprinted with permission from Ref. [49], OSA.

The LPG can also be enhanced by reducing the cladding via hydrofluoric (HF) acid [13, 45–47] and plasma [48] etching to tailor the coupling strength of the cladding mode at PMTP. Using this method, Biswas et al. were able to increase the refractive index sensitivity of a hydrogen loaded PMTP LPG with a 165 μm period from 1350 to 1847 nm/RIU [45]. A refractive index sensitivity reported by Villar is 143×10^3 nm/RIU [49]. **Figure 5** shows the resonance band of the LPG splitting into two separate bands with a wavelength separation of approximately 200 nm, with a change of 0.001 RIU. This was theoretically obtained by reducing the diameter of a SMF28 single mode to 34.8 μm whilst operating at a period close to PMTP at 288.5 μm [49].

Plasma etching via ion bombardment and chemical reaction has been used to etch the fibre cladding of an LPG to bring the resonance closer to the turning point. This process assists in the precise post processing of nano-coated fibres in hard and chemically resistant films, for example, diamond-like carbon [50]. Radiation exposure has also been demonstrated to alter the refractive index of B-Ge co-doped fibres, with an equivalent increase in core refractive index of around 1×10^{-5} [12].

3.1 Fabrication considerations

Due to the nature of the LPG, they can be highly sensitive to the surrounding environment. There are stringent demands placed on the fabrication process and the system used in order to fabricate LPGs at PMTP reproducibly. The notable constraints are given by ambient temperature (**Figure 6**), duty cycle [32], power of the irradiation source [35] and amplitude of the index modulation [51]. The difference in the final outcome of LPG spectra where the ambient temperature is not controlled and allowed to fluctuate, and maintained to $\pm 0.5^\circ\text{C}$ are shown in **Figure 6(a)** and **(b)**, respectively.

A period change of less than 1 μm can also influence transmission spectrum significantly and high resolution control has to be taken into account when deciding on the grating period [32, 35]. UV exposure time may also play a part in the sensitivity of LPGs at turning point; the spectrum of a 168.7 μm period PMTP LPG written in

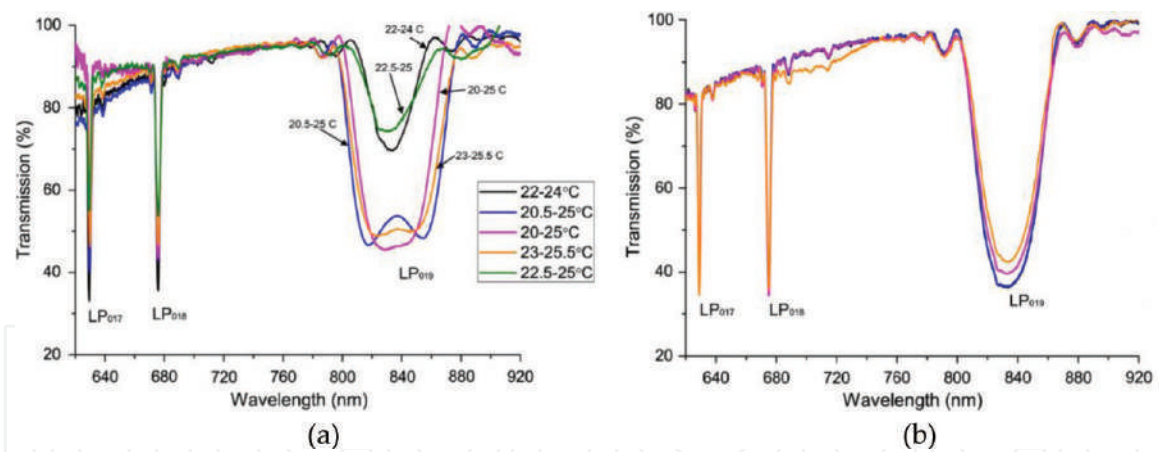


Figure 6. Transmission spectra of a 110.9 μm PMTP LPG. The temperature is (a) not controlled (5 spectra) and (b) controlled to $\pm 0.5^\circ\text{C}$ (4 spectra). Reprinted with permission from Ref. [32], OSA.

boron co-doped fibre had a greater variation with pressure when fabricated with a longer exposure time [34]. Other factors that can affect the grating include the size of the fibre. By changing the diameter of the cladding, but maintaining the same period, the dual resonance bands will also change accordingly [44].

Hydrogen loading can induce or increase the photosensitivity in a fibre by increasing the effective refractive index difference between the core and cladding [52]. However, hydrogen will diffuse from the fibre gradually over time, causing the LPG spectrum to drift [52, 53]. Annealing a hydrogen loaded fibre at a temperature above the desired operating temperature can help overcome this problem [54]. This rapid removal of hydrogen will still cause the resonance wavelengths to shift, due to the changing effective indices, but will remain stable and permanent after the annealing process has been completed. This has to be taken into consideration when choosing a period to fabricate an LPG, at or around turning point, using a hydrogen loaded fibre [33, 43].

4. Applications

For an LPG to function at its optimum sensitivity when exposed to an external perturbation, its period should be chosen such that it is able to operate at a turning point. Optical LPGs operating at the turning point provide the potential for low cost sensors with fast response time [21, 55, 56] and can provide a simpler detection method as some are able to work as intensity-based sensors [15, 17, 55].

LPGs operating at the PMTP have been used for temperature, strain, refractive index sensing [11, 35] and as filters. PMTP LPGs, when modified with a functional film can be adapted for potential uses as enhanced gas and chemical sensors [28].

4.1 Filters

By employing the broadband characteristics, PMTP LPGs can make successful bandpass and rejection filters [57, 58]. A coated PMTP LPG with a π phase shift is simulated to provide tuneable broadband characteristics for rejection filtering applications [58]. By introducing multiple π phase shifts, it is possible to adjust the separation between the dual resonant bands. On the other hand, by partially coating a phase shifted PMTP LPG, bandgaps appear over a narrow wavelength band which could be useful for designing spectral filters [59].

4.2 Temperature sensing

By careful choice of the grating period to allow coupling close to or at the turning point, it is possible to improve the temperature sensitivity of an LPG [14, 15, 33, 60]. Shu et al. [14] showed that for an LPG with a 175 μm period, the dual resonance band had a temperature sensitivity of 3.2 nm/ $^{\circ}\text{C}$ whereas the single band away from the PMTP had a much lower sensitivity of -0.31 nm/ $^{\circ}\text{C}$. The response of the dual resonant bands to changing temperature is non-linear, with a reduction in the rate of separation as the resonance moves away from the phase matching turning point. A band operating away from the turning point has a linear response to changing temperatures [60], which may make it easier to characterise temperature sensitivity. When comparing the sensitivities of LPGs with periods of 110.8, 111 and 111.5 μm the highest sensitivity was seen when the LPG was chosen to operate near the PMTP (111.5 μm period), just as the single broad resonance band would begin to appear. A sensitivity of 0.99 nm/ $^{\circ}\text{C}$ was achieved for the sensor at turning point, which was more than five times greater when compared to the sensitivity of a band away from turning point (0.17 nm/ $^{\circ}\text{C}$). As the temperature response changes depending on the surrounding environment, it may also be possible for the thermo-optic coefficients of a surrounding medium to be characterised [60].

4.3 Strain sensing

Previous studies have shown that the dual resonance bands will move together, when increasing strain is applied, with a near linear trend [14]. The separation of the dual bands was calculated to be -33.6 nm/1000 μm whereas the sensitivity of an LPG can be more than an order of magnitude less [16]. Using the single broad band resonant mode at PMTP, Grubsky et al. [15] were able to obtain a sensor resolution of 1 μm by changing the coupling strength using different strengths of strain; the band would show an appreciable decrease in amplitude as strain increased, whilst the wavelength remained fixed as shown in **Figure 7**. The fixed wavelength allows for a simpler detection method as spectrometers or post processing can be bypassed for a simple photodetector [15].

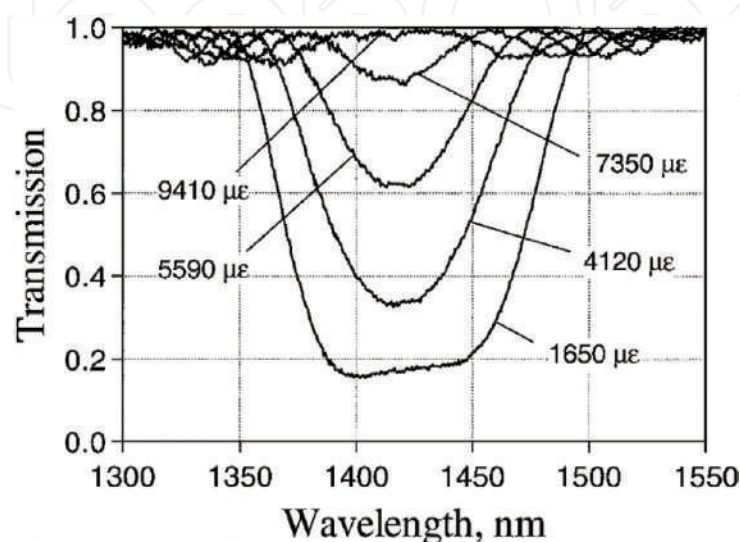


Figure 7. Transmission spectrum of a 50.1 μm period LPG with increasing strain. The wavelength of the band remains fixed at 1420 nm but the coupling efficiency decreases. Reprinted with permission from Ref. [15], OSA.

4.4 Refractive index sensing

The optical intensities of the guided cladding modes will likely dissipate out of the fibre after a short distance. This could be due the fibre being bent, or from scattering or absorption due to the protective jacket of the fibre. By removing the jacket, the cladding mode evanescent field extends into the immediate surroundings, which will influence the fibre mode properties. The refractive index of the local environment will affect the effective refractive indices of the cladding modes propagating in the fibre. These effective refractive indices determine the sensitivity of the PMTP LPG.

A refractive index PMTP LPG sensor based on intensity as opposed to wavelength shift provides high sensitivity with a linear response for different refractive indices. A linear correlation coefficient, of more than 0.98 and sensitivity of 59.88/RIU for the refractive index range of 1.410–1.420 was achieved using a PMTP LPG with a period of 231.5 μm [17]. This allows for simple calibration and linear interpolation to determine the sensitivity of the sensor within this refractive index range.

By coating a PMTP LPG, such that it coincides with the mode transition region, it can be possible to enhance the refractive index sensitivity of a sensor [18, 31]. Mode transition describes the reorganisation of cladding modes caused when a higher refractive index material of a certain optical thickness surrounds the LPG [61–63]. After a certain thickness, the surrounding material is able to guide the outer most cladding mode, causing large shifts in the resonance wavelengths. The sensitivity of the LPG can also be optimised by controlling the optical thickness of the overlay so that the turning point coincides with the mode transition region, and has been proven theoretically and experimentally [28, 64]. Pilla et al. [18] were able to achieve a sensitivity exceeding 9000 nm/RIU in solutions with RIs similar to water, using an LPG with a single resonance band close to 1.55 μm . By increasing the refractive index, the dual bands appear and eventually split as shown in **Figure 8**. A mesoporous coating consisting of silica nanospheres was able to improve the refractive index sensitivity of a 100 μm period LPG operating near turning point, with a maximum sensitivity of 1927 ± 59 nm/RIU, as well as increase the detection range of the LPG [19]. The refractive index sensitivity of the first electric arc induced LPG at turning point was increased from 400 to 700 nm/RIU to 887–2146 nm/RIU

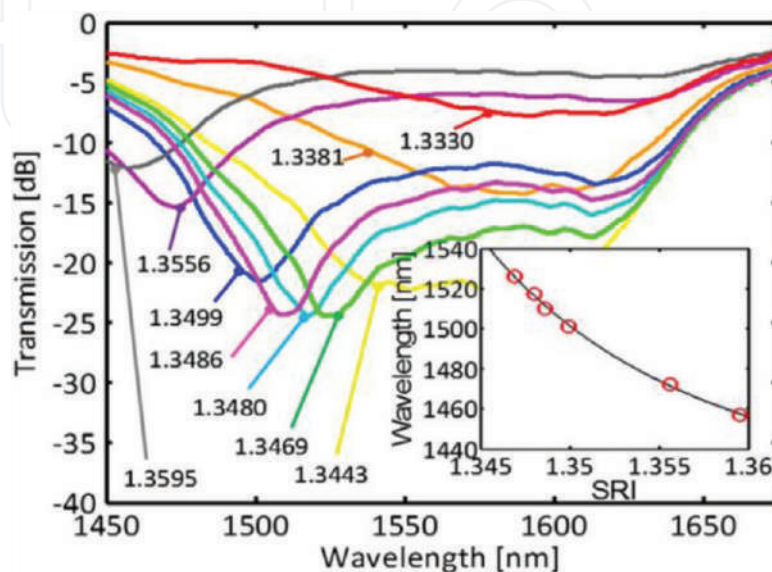


Figure 8. Transmission spectra showing the response to different refractive indices of ethanol solutions. SRI is surrounding refractive index. Reprinted with permission from Ref. [18], OSA.

by operating close to the turning point and by coating a thin film overlay of silicon nitride [20]. By combining these phenomena with a reduced diameter fibre, it can be possible to further enhance the sensitivity of the LPG, which can help improve the resolution of biochemical sensing applications.

4.5 Chemical and gas sensing

Their small dimensions, suitability in harsh environments and versatility make fibres ideal sensing platforms. The high sensitivity property of the PMTP allows for detection of low quantities and concentrations of different chemicals. For example, a PMTP is able to detect a 0.01% aqueous solution of cane sugar [65].

Optical fibre sensors with functional thin film coatings have become of interest due to the large pool of possible applications, especially in the chemical and bio-sensing fields. These sensors have the potential to measure concentrations of chemicals or for detecting gaseous species. These thin films can improve the sensing ability of the fibre and allow them to have different responses to different stimuli, such as concentrations of chemicals in the surrounding environment [19, 66, 67]. Functional materials can also be used to enhance the sensitivity for detection of a particular analyte. The thickness of the film on the LPG sensor is usually in the region of a few 100 nm as the transmission spectrum can be greatly affected [28, 61, 68, 69].

The following techniques allow for nanoscale thickness deposition control of the coating. These include the Langmuir–Blodgett deposition [28, 59, 70], self-assembly [21, 55, 71], layer-by-layer deposition [19], atomic layer deposition [72], sol-gel [73] and liquid phase deposition [67].

Functionalised LPGs operating around the PMTP have been tested for volatile organic compound (VOC) detection [70, 74, 75]. VOCs can be generated from a variety of processes. These include, but are not limited to, fuels and combustion processes, petroleum products, paints, and in nature and farming [76]. PMTP LPGs have been used for toluene [70, 74] and benzene [74] detection. By applying a functional overlay, particular compounds will affect the refractive index of the overlay and therefore influence the fibre modes, which will be shown as changes in transmission spectrum [74]. Providing clean water is an integral part of life, therefore monitoring water quality is critical. Partridge et al. demonstrated a proof-of-concept sensor for detecting toluene contamination in water. A 97 μm period LPG at turning point coated with calix [4]res C11 and was shown to be specific to toluene when compared to another potential contaminant, ethanol as shown in **Figure 9(a)**. The sensor was able to achieve a minimum detection limit of 100 ppm (see **Figure 9(b)**) which is the approximate limit of oil weep sampling and leaking oil plumes [70]. Some gases, such as hydrogen, are odourless and colourless, and have a low ignition energy. Means of detecting leaks in small quantities are therefore an important safety tool. A sensor coated with a 70 nm thick palladium overlay, when exposed to 4% hydrogen, experienced a dual band wavelength shift apart of 7.5 nm [77]. A thin film PMTP LPG with a functional material of poly(acrylic acid) PAA was successfully used to selectively bind to ammonia with lower detection levels when compared to other devices such as colorimetric and absorption spectroscopic devices [71].

Optical sensors have become more popular and valuable in the biomedical field. They have the potential to be used for diagnosis and monitoring and can be cost effective, portable and easy to use. This has also contributed to the increase in interest in label-free sensing using LPGs, especially at the PMTP where there is high RI sensitivity, rapid response and adaptability by choice of overlay [18, 72, 78, 79]. LPGs at PMTP have been used for real time monitoring of phage-bacteria interactions [80, 81] where a 1.3 nm wavelength shift was detected as bacteria binding

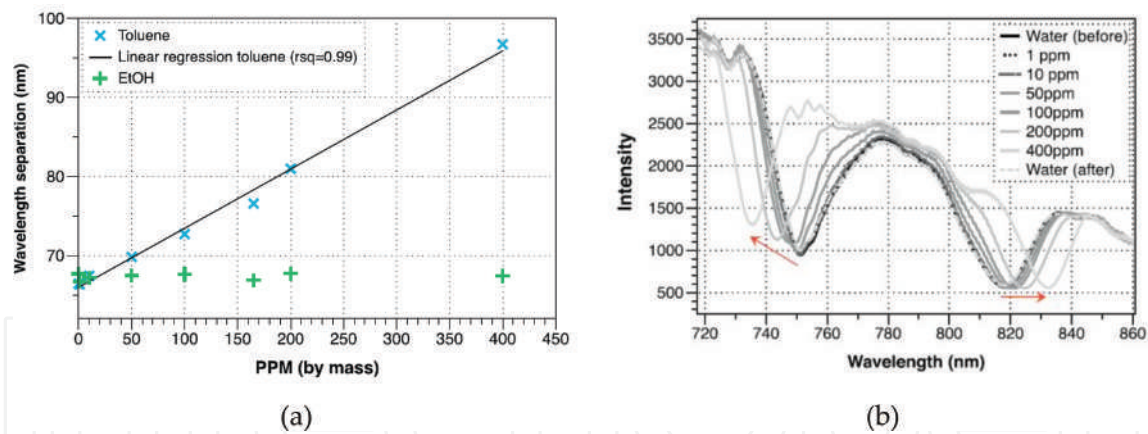


Figure 9. (a) Plots showing the response of a calix [4]red C11 coated LPG sensor to toluene and ethanol concentrations. Exposure to ethanol shows negligible response compared to toluene. (b) Transmission spectra showing the response of the dual resonance bands of a calix [4]red C11 coated LPG to different concentrations of toluene. Partridge et al.,. Reprinted from [70]; originally published under CC BY 3.0 licence. Available from: [10.1016/j.snb.2014.06.121](https://doi.org/10.1016/j.snb.2014.06.121)

occurred [80], and target-probe DNA hybridisation [82, 83]. The well-known properties of the streptavidin-biotin interaction, as well as its use for studying biological processes, have encouraged its use as a means of understanding the characteristics of thin film PMTP sensors [21, 55]. Korposh et al. showed a mesoporous SiO_2 film coated sensor with an additional functional material could detect a specific chemical species. In this case the species was a porphyrin compound, with a $10 \mu\text{M}$ concentration being detected in under 10s [56].

Selectivity is an important indicator for a sensor as it can potentially prevent false readings, which is especially helpful at the highly sensitive turning point region [66, 67, 84]. Molecular imprinting provides a versatile platform as the properties of the receptor can be modified to detect a desired molecular compound [66, 67]. An LPG coated with a molecularly imprinted polymer (MIP) was prepared, for the detection of antibiotics [66]. In the presence of different commonly prescribed antibiotics, the sensor showed selectivity to the target antibiotic vancomycin. The target compound can also be removed and the sensor reused. Removal methods used include organic solvents, and photodecomposition have also been investigated [67]. Reusing an LPG or sensor also increases the versatility of a biosensor [81, 82, 84] and can therefore be more time and cost effective.

Choosing a particular fibre type can also contribute to the final characteristics of the fabricated sensor. For instance, PMTP LPGs written in boron co-doped fibres have been demonstrated as radiation dose sensors [36], pressure sensors [34] (boron co-doping can increase the pressure-optic coefficient of a material [85]), and for fuel adulteration detection [39].

4.6 Sensor limitations

The inherent high sensitivity of the PMTP LPG also leads to its limitations. For instance, cross-talk or unwanted interference, such as from varying temperature, have to be limited in order to ensure the shift in the wavelengths is only due to the desired parameter. By fabricating cascaded PMTP LPGs, based on a Mach-Zehnder interferometer, it is possible to eliminate interference [86] and make simultaneous measurements for parameter compensated sensing [87]. James et al. demonstrated that coating a cascaded PMTP LPG device with mesoporous silica nanoparticles, and subsequently infusing a functional material to the central of the region (between the two gratings) enables measuring of only the desired analyte [86].

The broad spectral width of the resonance bands can also limit the multiplexing capabilities of the PMTP LPG. By utilising the double resonance bands, simultaneous measurements of surrounding refractive index and temperature were carried out for temperature ranges limited to $\pm 3^{\circ}\text{C}$ if the refractive index range is ± 0.004 RIU [87]. This information enables temperature calibrated sensing.

5. Summary

PMTP LPGs as versatile sensing platforms have become increasingly popular. The ultra-high sensitivity and quick response, as compared to other configurations of LPGs, proposes promising capabilities for use in many sensing applications. PMTP LPGs can be achieved by the precise choice of period or by post processing methods. However, the nature of their high sensitivity can also pose as limitations and sensors need to be optimised in order to avoid interference. By applying functional nanoscale coatings, it has been possible to tailor PMTP LPGs to have a preferred sensitivity to particular parameters. This opens the doors for a number of applications in the medical field for portable, real time monitoring. The sensors have potential deployment into the biochemical industry for measuring chemical concentrations and can also be applied to sense different gases in the environment. Specially designed sensors can also be used for monitoring food quality. However, calibration must be carried out first as the period and thickness of coating will affect the sensitivity of the sensor. More vigorous and consistent testing needs to be carried out before adoption in the healthcare and food safety industry [2]. Sensor packaging, ease of use and reusability are some aspects that need to be taken into consideration. As many chemical sensing applications take place in a solution, it may be beneficial to fabricate an LPG such that the appearance of the dual resonance bands will appear when the fibre is placed in solution. The fibre cladding size can greatly affect the sensitivity allowing a greater flexibility when designing an LPG at PMTP [49].

IntechOpen

IntechOpen

Author details

Rebecca Yen-Ni Wong^{1*}, Dora Hu Juan Juan¹, Morten Ibsen² and Perry Ping Shum^{3,4}

1 Institute for Infocomm Research, Agency for Science, Technology and Research (A*STAR), Singapore

2 Optoelectronics Research Centre, University of Southampton, Southampton, United Kingdom

3 Centre for Optical Fibre Technology, School of Electrical and Electronic Engineering, Nanyang Technological University, Singapore

4 CINTRA CNRS/NTU/THALES, UMI 3288, Research Techno Plaza, Singapore

*Address all correspondence to: rebecca-wong@i2r.a-star.edu.sg

IntechOpen

© 2019 The Author(s). Licensee IntechOpen. This chapter is distributed under the terms of the Creative Commons Attribution License (<http://creativecommons.org/licenses/by/3.0>), which permits unrestricted use, distribution, and reproduction in any medium, provided the original work is properly cited. 

References

- [1] Alwis L, Sun T, Grattan KTV. Developments in optical fibre sensors for industrial applications. *Optics and Laser Technology*. 2016;**78**(A): 62-66. DOI: 10.1016/j.optlastec.2015.09.004
- [2] Correia R, James S, Lee SW, Morgan SP, Korposh S. Biomedical application of optical fibre sensors. *Journal of Optics*. 2018;**20**(7):1-25. DOI: 10.1088/2040-8986/aac68d
- [3] Ramakrishnan M, Rajan G, Semenova Y, Farrell G. Overview of Fiber optic sensor Technologies for Strain/temperature sensing applications in composite materials. *Sensors*. 2016;**16**(99):1-27. DOI: 10.3390/s16010099
- [4] Mescia L, Prudenzano F. Advances on optical Fiber sensors. *Fibers*. 2014;**2**(1):1-23. DOI: 10.3390/fib2010001
- [5] Vengsarkar AM, Lemaire PJ, Judkins JB, Bhatia V, Erdogan T, Sipe JE. Long-period fiber gratings as band-rejection filters. *Journal of Lightwave Technology*. 1996;**14**(1):58-65. DOI: 10.1109/50.476137
- [6] Vengsarkar AM, Lemaire PJ, Judkins JB, Bhatia B, Erdogan T, Sipe JE. Long-period fiber gratings as band-rejection filters. In: *Optical Fiber Communications PD4*; San Diego; 1995
- [7] James SW, Tatam RP. Optical fibre long-period grating sensors: Characteristics and application. *Measurement Science and Technology*. 2003;**14**(5):R49-R61. DOI: 10.1088/0957-0233/14/5/201
- [8] Kashyap R. *Fibre Bragg Gratings*. 2nd ed. New York: Academic Press; 2010. DOI: 10.1016/C2009-0-16830-7
- [9] Werneck MMM, Allil RCSB, de Nazaré FVB. *Fiber Bragg Gratings: Theory, Fabrication, and Applications*. Washington: SPIE; 2017. DOI: 10.1117/3.2286558
- [10] Liu Z, Tam HY. Industrial and medical applications of fiber Bragg gratings (invited paper). *Chinese Optics Letters*. 2016;**14**(12):120007, 10.3788/COL201614.120007
- [11] Shu X, Zhang L, Bennion I. Sensitivity characteristics near the dispersion turning points of long-period fiber gratings in B/Ge codoped fiber. *Optics Letters*. 2001;**26**(22):1755-1757. DOI: 10.1364/OL.26.001755
- [12] Chaubey S, Kher S, Oak SM. Radiation and taper tuning of long period grating for high sensitivity strain measurement. In: *7th Workshop on Fibre and Optical Passive Components*. Montreal: Proceedings of the IEEE; 2011
- [13] Chen X, Zhou K, Zhang L, Bennion I. Dual-peak long-period fiber gratings with enhanced refractive index sensitivity by finely tailored mode dispersion that uses the light cladding etching technique. *Applied Optics*. 2007;**46**(4):451-455. DOI: 10.1364/AO.46.000451
- [14] Shu X, Shang L, Bennion I. Sensitivity characteristics of long-period fiber gratings. *Journal of Lightwave Technology*. 2002;**20**(2): 255-266. DOI: 10.1109/50.983240
- [15] Grubsky V, Feinberg J. Long-period fiber gratings with variable coupling for real-time sensing applications. *Optics Letters*. 2000;**25**(4):203-205. DOI: 10.1364/OL.25.000203
- [16] Bhatia V, Campbell DK, Sherr D, D'Alberto TG, Zaboronick NA, Eyck GAT, et al. Temperature-insensitive and strain-insensitive long-period grating

- sensors for smart structures. *Optical Engineering*. 1997;**36**(7):1872-1876. DOI: 10.1117/1.601379
- [17] Lan X, Han Q, Huang J, Wang H, Gao Z, Kaur A, et al. Turn-around point long-period fiber grating fabricated by CO₂ laser for refractive index sensing. *Sensors and Actuators B: Chemical*. 2013;**177**:1149-1155. DOI: 10.1016/j.snb.2012.12.006
- [18] Pilla P, Trono C, Baldini F, Chiavaioli F, Giordano M, Cusano A. Giant sensitivity of long period gratings in transition mode near the dispersion turning point: An integrated design approach. *Optics Letters*. 2012;**37**(19):4152-4154. DOI: 10.1364/OL.37.004152
- [19] Korposh S, Lee SW, James SW, Tatam RP. Refractive index sensitivity of fibre-optic long period gratings coated with SiO₂ nanoparticle mesoporous thin films. *Measurement Science and Technology*. 2011;**22**(7):1-10. DOI: 10.1088/0957-0233/22/7/075208
- [20] Debowska AK, Smietana M, Mikulic P, Bock WJ. High temperature nano-coated electric-arc-induced long-period gratings working at the dispersion turning point for refractive index sensing. *Japanese Journal of Applied Physics*. 2014;**53**(8S2)::08ME01-1-08ME01-5). DOI: 10.7567/JJAP.53.08ME01
- [21] Marques L, Hernandez FU, James SW, Morgan SP, Clark M, Tatam RP, et al. Highly sensitive optical fibre long period grating biosensor anchored with silica core gold shell nanoparticles. *Biosensors and Bioelectronics*. 2016;**75**:222-231. DOI: 10.1016/j.bios.2015.08.046
- [22] Ghambir M, Gupta S. Review of turn around point long period fiber gratings. *Journal of Sensor Technology*. 2015;**5**(4):81-89. DOI: 10.4236/jst.2015.54009
- [23] Kanka J. Design of turn-around-point long-period gratings in a photonic crystal fiber for refractometry of gases. *Sensors and Actuators B: Chemical*. 2013;**182**:16-24. DOI: 10.1016/j.snb.2013.02.048
- [24] Erdogan T. Cladding-mode resonances in short- and long- period fiber grating filters. *Journal of the Optical Society of America. A*. 1997;**14**(8):1760-1773. DOI: 10.1364/JOSAA.14.001760
- [25] Erdogan T. Cladding-mode resonance in short- and long- period fiber grating filters: Errata. *Journal of the Optical Society of America. A*. 2000;**17**(11):2113. DOI: 10.1364/JOSAA.17.002113
- [26] Huang WP. Coupled-mode theory for optical waveguides: An overview. *Journal of the Optical Society of America. A*. 1994;**11**(3):963-983. DOI: 10.1364/JOSAA.11.000963
- [27] Gloge D. Weakly guiding fibers. *Applied Optics*. 1971;**10**(10):2252-2258. DOI: 10.1364/AO.10.002252
- [28] Cheung CS, Topliss SM, James SW, Tatam RP. Response of fibre optic long period gratings near the phase matching turning point to the deposition of nanostructured coatings. *Journal of the Optical Society of America B: Optical Physics*. 2008;**25**(6):897-902. DOI: 10.1364/JOSAB.25.000897
- [29] MacDougall TW, Pilevar S, Haggans CW, Jackson MA. Generalized expression for the growth of long period gratings. *IEEE Photonics Technology Letters*. 1998;**10**(10):1449-1451. DOI: 10.1109/68.720290
- [30] Rego G. Arc-induced long period fiber gratings. *Journal of Sensors*. 2016;**2016**:1-13. DOI: 10.1155/2016/3598634

- [31] Korposh S, James S, Tatam R, Lee SW. Optical fibre long-period gratings functionalised with nano-assembled thin-films: Approaches to chemical sensing. In: Cuadrado-Laborde C, editor. *Current Trends in Short- and Long-Period Fiber Gratings*. Rijeka: InTech; 2013. pp. 63-86. DOI: 10.5772/52935
- [32] Wong RYN, Chehura E, Staines SE, James SW, Tatam RP. Fabrication of fiber optic long period gratings operating at the phase matching turning point using an ultraviolet laser. *Applied Optics*. 2014;**53**(21):4669-4674. DOI: 10.1364/AO.53.004669
- [33] Mizunami T, Fukuda T, Hayashi A. Fabrication and characterization of long-period-grating temperature sensors using Ge-B-co-doped photosensitive fibre and single-mode fibre. *Measurement Science and Technology*. 2004;**15**(8):1467-1473. DOI: 10.1088/0957-0233/15/8/006
- [34] Smietana M, Bock WJ, Mikulic P, Chen J. Tuned pressure sensitivity of dual resonant long-period gratings written in boron co-doped optical fiber. *Journal of Lightwave Technology*. 2012;**30**(8):1080-1084. DOI: 10.1109/JLT.2011.2169234
- [35] Lan X, Han Q, Wei T, Huang J, Xiao H. Turn-around-point long-period fiber gratings fabricated by CO₂ laser point-by-point irradiation. *IEEE Photonics Technology Letters*. 2011;**23**(22):1664-1666. DOI: 10.1109/LPT.2011.2166256
- [36] Kher S, Chaubey S, Kashyap R, Oak SM. Turnaround-point long-period fiber gratings (TAP-LPGs) as high-radiation-dose sensors. *IEEE Photonics Technology Letters*. 2012;**24**(9):742-744. DOI: 10.1109/LPT.2012.2187637
- [37] Shen F, Zhou K, Zhang L, Shu X. Long period Fiber grating around the dispersion turning point fabricated with a femtosecond laser. In: *Proceedings of OSA*. Guangzhou: ACPC; 2017
- [38] Colaço C, Caldas P, Del Villar I, Chibante R, Rego G. Arc-induced long-period Fiber gratings in the dispersion turning points. *Journal of Lightwave Technology*. 2016;**34**(19):4584-4590. DOI: 10.1109/JLT.2016.2540678
- [39] Kher S, Chaubey S, Kishore J, Oak SM. Detection of fuel adulteration with high sensitivity using turnaround point long period fiber gratings in B/Ge doped fibers. *IEEE Sensors Journal*. 2013;**13**(11):4482-4486. DOI: 10.1109/JSEN.2013.2270312
- [40] Martinez-Rios A, Monzon-Hernandez D, Torres-Gomez I, Salceda-Delgado G. Long period fibre gratings. In: Yasin M, editor. *Fiber Optic Sensors*. Rijeka: InTech; 2012. pp. 275-294. DOI: 10.5772/27727
- [41] Coelho JMP, Nespereira MC, Abreu M, Rebordao JM. Modeling refractive index change in writing long-period fiber gratings using mid-infrared laser radiation. *Photonic Sensors*. 2013;**3**(1):67-73. DOI: 10.1007/s13320-012-0084-1
- [42] Ahmed F, Joe HE, Min BK, Jun MBG. Characterization of refractive index change and fabrication of long period gratings in pure silica fiber by femtosecond laser radiation. *Optics and Laser Technology*. 2015;**74**:119-124. DOI: 10.1016/j.optlastec.2015.05.018
- [43] Shu X, Zhu X, Wang Q, Jiang S, Shi W, Huang Z, et al. Dual resonant peaks of LP₀₁₅ cladding mode in long-period gratings. *Electronics Letters*. 1999;**35**(8):649-651. DOI: 10.1049/el:19990442
- [44] Ling Q, Gu Z, Gao K. Smart design of a long-period fiber grating refractive index sensor based on dual-peak resonance near the phase-matching turning point. *Applied Optics*. 2018;**57**(10):2693-2697. DOI: 10.1364/AO.57.002693

- [45] Biswas P, Basumallick N, Bandyopadhyay S, Dasgupta K, Ghosh A, Bandyopadhyay S. Sensitivity enhancement of turn-around-point long period gratings by tuning initial coupling condition. *IEEE Sensors Journal*. 2015;**15**(2):1240-1245. DOI: 10.1109/JSEN.2014.2361166
- [46] Mysliwiec M, Grochowski J, Krogulski K, Mikulic P, Bock WJ, Smietana M. Effect of wet etching of arc-induced long-period gratings on their refractive index sensitivity. *Acta Physica Polonica, A*. 2013;**124**(3): 521-524. DOI: 10.12693/APhysPolA.124.521
- [47] Szymanska M, Krogulski K, Mikulic P, Bock WJ, Smietana M. Sensitivity of long-period gratings modified by their bending. In: *Procedia Engineering*, 28th Eurosensors; Brescia; 2014. pp. 1180-1183
- [48] Smietana M, Koba M, Mikulic P, Bock WJ. Measurements of reactive ion etching process effect using long-period fiber gratings. *Optics Express*. 2014;**22**(5):5986-5994. DOI: 10.1364/OE.22.005986
- [49] Del Villar I. Ultrahigh-sensitivity sensors based on thin-film coated long period gratings with reduced diameter, in transition mode near the dispersion turning point. *Optics Express*. 2015;**23**(7):8389-8398. DOI: 10.1364/OE.23.008389
- [50] Smietana M, Koba M, Mikulic P, Bock WJ. Tuning properties of long-period gratings by plasma post-processing of their diamond-like carbon nano-overlays. *Measurement Science and Technology*. 2014;**25**:1-7. DOI: 10.1088/0957-0233/25/11/114001
- [51] Partridge M, James S, Barrington J, Tatam R. Overwrite fabrication and tuning of long period gratings. *Optics Express*. 2016;**24**(20):22345-22356. DOI: 10.1364/OE.24.022345
- [52] Mizunami T, Fukuda T. FEM calculation and the effects of hydrogen diffusion in fabrication processes of long-period fiber gratings. *Optics Communication*. 2006;**259**(2):581-586. DOI: 10.1016/j.optcom.2005.09.002
- [53] Namihira Y, Mochizuki K, Kuwazuru M, Iwamoto Y. Effects of hydrogen diffusion on optical fibre loss increase. *Electronics Letters*. 1983;**19**(24):1034-1035. DOI: 10.1049/el:19830701
- [54] Libish TM, Bobby MC, Linesh J, Mathew S, Biswas P, Bandyopadhyay S, et al. The effect of annealing and temperature on transmission spectra of long period gratings written in hydrogen loaded standard single mode fiber. *Optik*. 2013;**124**(20):4345-4348. DOI: 10.1016/j.ijleo.2013.02.010
- [55] Wang Z, Helfin JR, Cott KV, Stolen RH, Ramachandran S, Ghalmi S. Biosensors employing ionic self-assembled multilayers adsorbed on long-period fiber gratings. *Sensors and Actuators B: Chemical*. 2009;**139**(2):618-623. DOI: 10.1016/j.snb.2009.02.073
- [56] Korposh S, James SW, Lee SW, Topliss S, Cheung SC, Batty WJ, et al. Fiber optic long period grating sensors with a nanoassembled mesoporous film of SiO₂ nanoparticles. *Optics Express*. 2010;**18**(12):13227-13228. DOI: 10.1364/OE.18.013227
- [57] Ramachandran S, Ghalmi S, Wang Z, Yan M. Band-selection filters with concatenated long-period gratings in few-mode fibers. *Optics Letters*. 2002;**27**(19):1678-1680. DOI: 10.1364/OL.27.001678
- [58] Chen H, Gu Z. Filtering characteristics of film-coated long-period fiber gratings operating at the phase-matching turning point. *Optik*. 2014;**125**(20):6003-6009. DOI: 10.1016/j.ijleo.2014.07.060

- [59] James SW, Topliss SM, Tatam RP. Properties of length-apodized phase-shifted LPGs operating at the phase matching turning point. *Journal of Lightwave Technology*. 2012;**30**(13):2203-2209. DOI: 10.1109/JLT.2012.2195473
- [60] Korposh S, Wong R, James S, Tatam R. Temperature and thermo-optic coefficient measurements using optical fibre long period gratings operating at phase matching turning point. In: *Proceedings of SPIE, 5th EWOFS; Krakow; 2013*
- [61] Del Villar I, Achaerandio M, Matias IR, Arregui FJ. Deposition of overlays by electrostatic self-assembly in long-period fiber gratings. *Optics Letters*. 2005;**30**(7):720-722. DOI: 10.1364/OL.30.000720
- [62] Cusano A, Iadicicco A, Pilla P, Contessa L, Campopiano S, Cutolo A. Mode transition in high refractive index coated long period gratings. *Optics Express*. 2006;**14**(1):20-34. DOI: 10.1364/OPEX.14.000019
- [63] Cusano A, Iadicicco A, Pilla P, Contessa L, Campopiano S, Cutolo A. Cladding mode reorganization in high-refractive index-coated long-period gratings: Effects on the refractive-index sensitivity. *Optics Letters*. 2005;**30**(19):2536-2538. DOI: 10.1364/OL.30.002536
- [64] Brabant D, Koba M, Smietana M, Bock WJ. Analysis of mode transitions in a long-period fiber gratings with nano-overlay of diamond-like carbon. In: *Proceedings of SPIE, Photonics North; Montreal; 2014*
- [65] Shu X, Huang D. Highly sensitive chemical sensor based on the measurement of the separation of dual resonant peaks in a 100-um-period fiber grating. *Optics Communication*. 1999;**171**(1-3):65-69. DOI: 10.1016/S0030-4018(99)00522-2
- [66] Korposh S, Chianella I, Guerreiro A, Caygill S, Piletsky S, James SW, et al. Selective vancomycin detection using optical fibre long period gratings functionalised with molecularly imprinted polymer nanoparticles. *The Analyst*. 2014;**139**(9):2229-2236. DOI: 10.1039/c3an02126b
- [67] Wong R, Korposh S, Lee SW, James SW, Tatam RP. Photodecomposition of a target compound detected using an optical fibre long period grating coated with a molecularly imprinted titania thin film. In: *Proceedings of SPIE, 24th OFS; Curitiba; 2015*
- [68] Rees ND, James SW, Tatam RP, Ashwell GJ. Optical fiber long-period gratings with Langmuir-Blodgett thin-film overlays. *Optics Letters*. 2002;**27**(9):686-688. DOI: 10.1364/OL.27.000686
- [69] Bandyopadhyay S, Biswas P, Chiavaioli F, DT K, Basumallick N, Trono C, et al. Long-period fiber grating: A specific design for biosensing applications. *Applied Optics*. 2017;**56**(35):9846-9853. DOI: 10.1364/AO.56.009846
- [70] Partridge M, Wong R, James SW, Davis F, Higson SPJ, Tatam RP. Long period grating based toluene sensor for use with water contamination. *Sensors and Actuators B: Chemical*. 2014;**203**:621-625. DOI: 10.1016/j.snb.2014.06.121
- [71] Wang T, Korposh S, Wong R, James S, Tatam R, Lee SW. A novel ammonia gas sensor using nanoassembled polyelectrolyte thin film on fiber-optic long-period gratings. *Chemistry Letters*. 2012;**41**(10):1297-1299. DOI: 10.1246/cl.2012.1297
- [72] Smietana M, Koba M, Brzozowska E, Krogulski K, Nakonieczny J, Wachnicki L, et al. Label-free sensitivity of long-period gratings enhanced by atomic layer deposited

TiO₂ nano-overlays. *Optics Express*. 2015;**23**(7):8841-8453. DOI: 10.1364/OE.23.008441

[73] Chiavaioli F, Biswas P, Trono C, Jana S, Bandyopadhyay S, Basumallick N, et al. Sol-gel-based titania-silica thin film overlay for long period fiber grating-based biosensors. *Analytical Chemistry*. 2015;**87**(24):12024-12031. DOI: 10.1021/acs.analchem.5b01841

[74] Topliss SM, James SW, Davis F, Higson SPJ, Tatam RP. Optical fibre long period grating based selective vapour sensing of volatile organic compounds. *Sensors and Actuators B: Chemical*. 2010;**143**(2):629-634. DOI: 10.1016/j.snb.2009.10.008

[75] Korposh S, David F, James SW, Wang T, Lee SW, Higson S, et al. Detection of volatile organic compounds (VOCs) using an optical fibre long period grating with a calixarene anchored mesoporous thin film. In: *Proceedings of SPIE, 5th EWOFs; Krakow; 2013*

[76] Viricelle JP, Pauly A, Mazat L, Brunet J, Bouvet M, Varenne C, et al. Selectivity improvement of semi-conducting gas sensors by selective filter for atmospheric pollutants detection. *Materials Science and Engineering: C*. 2006;**26**(2-3):186-195. DOI: 10.1016/j.msec.2005.10.062

[77] Kim YH, Kim MJ, Rho BS, Park MS, Jang JH, Lee BH. Ultra sensitive fiber-optic hydrogen sensor based on high order cladding mode. *IEEE Sensors Journal*. 2011;**11**(6):1423-1426. DOI: 10.1109/JSEN.2010.2092423

[78] Pilla P, Manzillo PF, Malachovska V, Buosciolo A, Campopiano S, Cutolo A, et al. Long period grating working in transition mode as promising technological platform for label-free biosensing. *Optics Express*. 2009;**17**(22):20039-20050. DOI: 10.1364/OE.17.020039

[79] Chiavaioli F, Biswas P, Trono C, Bandyopadhyay S, Giannetti A, Tombelli S, et al. Towards sensitive label-free immunosensing by means of turn-around point long period fiber gratings. *Biosensors and Bioelectronics*. 2014;**60**:305-310. DOI: 10.1016/j.bios.2014.04.042

[80] Smietana M, Bock WJ, Mikulic P, Ng A, Chinnappan R, Zourob M. Detection of bacteria using bacteriophages as recognition elements immobilized on long-period fiber gratings. *Optics Express*. 2011;**19**(9):7971-7978. DOI: 10.1364/OE.19.007971

[81] Koba M, Smietana M, Brzozowska E, Gorska S, Mikulic P, Bock WJ. Reusable bacteriophage adhesin-coated long-period grating sensor for bacterial lipopolysaccharide recognition. *Journal of Lightwave Technology*. 2015;**33**(12):2518-2523. DOI: 10.1109/JLT.2014.2364118

[82] Chen X, Zhang L, Zhou K, Davies E, Sugden K, Bennion I, et al. Real-time detection of DNA interactions with long-period fiber-grating-based biosensor. *Optics Letters*. 2007;**32**(17):2541-2543. DOI: 10.1364/OL.32.002541

[83] Chen X, Liu C, Hughes MD, Nagel DA, Hine AV, Zhang L. EDC-mediated oligonucleotide immobilization on a long period grating optical biosensor. *Biosensors and Bioelectronics*. 2015;**6**(2):1-6. DOI: 10.4172/2155-6210.1000173

[84] Hromadka J, Tokay B, James S, Tatam RP, Korposh S. Optical fibre long period grating gas sensor modified with metal organic framework thin films. *Sensors and Actuators B: Chemical*. 2015;**221**:891-899. DOI: 10.1016/j.snb.2015.07.027

[85] Smietana M, Bock WJ, Chen J, Mikulic P. Highly sensitive pressure

sensor based on long-period gratings written in boron co-doped optical fiber. *Measurement Science and Technology*. 2010;**21**(9):1-5. DOI: 10.1088/0957-0233/21/9/094026

[86] James SW, Korposh S, Lee SW, Tatam RP. A long period grating-based chemical sensor insensitive to the influence of interfering parameters. *Optics Express*. 2014;**22**(7):8012-8023. DOI: 10.1364/OE.22.008012

[87] Garg R, Tripathi SM, Thyagarajan K, Bock WJ. Long period fiber grating based temperature-compensated high performance sensor for bio-chemical sensing applications. *Sensors and Actuators B: Chemical*. 2013;**176**: 1121-1127. DOI: 10.1016/j.snb.2012.08.059

IntechOpen

We are IntechOpen, the world's leading publisher of Open Access books Built by scientists, for scientists

6,300

Open access books available

171,000

International authors and editors

190M

Downloads

Our authors are among the

154

Countries delivered to

TOP 1%

most cited scientists

12.2%

Contributors from top 500 universities



WEB OF SCIENCE™

Selection of our books indexed in the Book Citation Index
in Web of Science™ Core Collection (BKCI)

Interested in publishing with us?
Contact book.department@intechopen.com

Numbers displayed above are based on latest data collected.
For more information visit www.intechopen.com



Whispering Gallery Modes for Accurate Characterization of Optical Fibers' Parameters

Martina Delgado-Pinar, Xavier Roselló-Mechó, Emmanuel Rivera-Pérez, Antonio Díez, José Luis Cruz and Miguel V. Andrés

Abstract

Whispering gallery modes (WGMs) are surface modes that propagate azimuthally around resonators with rotational symmetry (toroidal, spherical, or, as in our case, cylindrical shaped, since the optical fiber itself plays the role of the microresonator). These modes are resonant in optical wavelength, and the spectral position of the resonances depends on the radius and the refractive index of the microresonator material. Due to the high-quality factor of the resonances (as high as 10^7 in cylindrical microresonators), they allow measuring different parameters with high sensitivities and very low detection limits. Here, we report the use of WGMs to characterize the properties of the material that forms the microresonator. In particular, we highlight the use of this technique to measure temperature profiles along conventional and special fibers (such as photosensitive or doped fibers), elasto-optic coefficients, and UV-induced absorption loss coefficients of different photosensitive fibers. These parameters of the fibers set the optical response of fiber-based components and may change when the device is in use in an optical system; thus, this technique allows an accurate characterization of the devices and leads to proper designs of components with specific optical responses.

Keywords: whispering gallery modes, surface modes, microresonators, optical fibers, fiber Bragg gratings, elasto-optic effect, thermo-optic effect

1. Introduction

Whispering gallery modes are surface modes that propagate azimuthally around resonators with rotational symmetry, generally a dielectric. This phenomenon was first described by Lord Rayleigh in the nineteenth century, when studying the propagation of acoustic waves in interfaces with a curvature [1]. St. Paul's Cathedral (London, UK), the Temple of Heaven (Beijing, China), the Pantheon (Rome, Italy), the Tomb of Agamemnon (Mycenae, Greece), and the Whispering Gallery in the Alhambra (Granada, Spain) are examples of architectural structures that support acoustic modes which propagate guided by the surface of the walls. It was at the beginning of the twentieth century when the study of this guiding mechanism was extended to the electromagnetic waves, since Mie developed his theory for the

plane electromagnetic waves dispersed by spheres with diameters of the same size as the optical wavelength [2]. Shortly after, Debye established the equations for the optical resonances of dielectric and metallic spheres based on Mie's dispersion theory [3]. The detailed study of the mathematical equations of WGMs was performed by Richtmyer [4] and Stratton [5], who predicted high-quality factors Q for these resonances and led to its implementation in different technologies based on microwave and acoustic waves. In the microscopic world, light can be guided by the same mechanism, when the resonator has dimensions of tens to hundreds of microns, and the wavelength of the light is in the visible-infrared range. In 1989, Braginsky et al. set the beginning of the optical WGMs when reporting the technique to excite optical modes in microresonators with spherical shape [6]. Since then, many researchers have studied the propagation of WGMs in structures with different symmetries [7] and have reported efficient methods based on microtapers to excite these modes in the optical range [8].

Due to the intrinsic low losses, WGMs show very high Q factors. For example, they can achieve values of 10^{10} in spheres [9], 10^8 in silicon microtoroids [10], or 10^6 – 10^7 in cylindrical microresonators [11]. At the resonance, the light guided by a WGM is recirculated in the microresonator many times, which provides a mechanism for decreasing the detection limit of the sensors based on them. This enhanced detection limit has been demonstrated to be low enough to measure a single molecule on the surface of a microtoroid [12].

WGM resonances shift in wavelength as the refractive index of the external medium changes. The sensitivity of WGMs as a function of these variations is significant: when considering a silica-cylindrical microresonator of $125\ \mu\text{m}$ in diameter, immersed in water ($n = 1.33$), the calculated shift in wavelength of the resonance is $77\ \text{nm}/\text{RIU}$. For a typical resonance width of $0.5\ \text{pm}$, this leads to a detection limit of $6 \times 10^{-6}\ \text{RIU}$. It is worth to note that the light guided by WGMs is mainly confined in the microresonator. Thus, their sensitivity to variations of the material refractive index will be even higher. For example, it can achieve values as high as $1.1\ \mu\text{m}/\text{RIU}$ when considering variations of the refractive index of the silica. In this example, the detection limit of the WGM decreases down to $4 \times 10^{-7}\ \text{RIU}$. In this chapter, we will report the use of WGMs in silica, cylindrical microresonators (an optical fiber) to measure and characterize the properties of the microresonator itself. There are a number of parameters, such as temperature or strain, which modify the refractive index of the material. Thus, this technique allows measuring with accuracy variations of temperature in doped optical fibers, in optical devices as fiber Bragg gratings (FBG), the elasto-optic coefficients of conventional silica fibers, and the absorption coefficient of photosensitive optical fibers, for example. We will report here the fundamentals of the technique, as well as the experimental results we obtained for these experiments.

2. Fundamentals

The guiding mechanism of WGMs in the azimuthal direction of a microresonator (MR) is total internal reflection, just as in the case of axial propagation in a conventional waveguide; see **Figure 1a**. Resonance occurs when the guided wave travels along the perimeter of the MR, and it drives itself coherently by returning in phase after every revolution. In its way, the wave follows continuously the surface of the MR, and the optical path in a circumnavigation must be equal to an integer multiple of the optical wavelength, λ . When this condition is fulfilled, resonances appear, and a series of discrete modes at specific wavelengths will show up. The resonant condition can be written as [13]

$$\lambda_R = \frac{2\pi a \cdot n_{\text{eff}}}{m} \quad (1)$$

where λ_R is the resonant wavelength, a is the radius of the MR, n_{eff} is the effective index of the WGM, and m is the azimuthal order of the mode (i.e., the number of wavelengths in the perimeter of the MR). The effective indices of the different modes are calculated, as usual, by solving Maxwell's equations and applying the proper boundary conditions [5]. In our case, we will deal with cylindrical, dielectric MRs with translational symmetry in the axial direction (see **Figure 1b**). Two zones can be identified, regions I (of radius a) and II (which extends to the infinite), with refractive indices n_1 and n_2 , respectively, with $n_1 > n_2$. The magnetic permeability of the material and of the external medium is equal to that of the vacuum, μ_0 , and both media are homogeneous although, in general, they present an anisotropy in the dielectric permittivity. In the axial direction, we will consider a refractive index of the material n_{1z} which is different to the refractive index in the transversal directions, n_{1t} (see Eq. (2) for the expression of the tensor of the refractive index):

$$n_2 = \begin{pmatrix} n_{1t} & 0 & 0 \\ 0 & n_{1t} & 0 \\ 0 & 0 & n_{1z} \end{pmatrix} \quad (2)$$

We do not intend to give a full description of the solution of this problem, which can be found in [14], but we will summarize the main equations and features of WGMs.

If we solve Maxwell's equations with this uniaxial tensor, the modes split in two series of family modes that, analogously to the case of axial waveguides, are denoted as TE-WGMs, which show a transversal electric field ($e_z = 0$), and TM-WGMs, with transversal magnetic field ($h_z = 0$). Each series of modes is ruled by a transcendental equation that must be solved: Eq. (3) for TM modes and Eq. (4) for TE modes. The solutions consist on a series of discrete wavelengths, which correspond to the different radial orders l of each m^{th} value. With these values, it is possible to calculate the effective indices of each WGM resonance using Eq. (1):

$$n_{1z} \frac{J_{m'}(k_0 n_{1z} a)}{J_m(k_0 n_{1z} a)} = n_2 \frac{H_m^{(2)'}(k_0 n_2 a)}{H_m^{(2)}(k_0 n_2 a)} \quad (3)$$

$$\frac{1}{n_{1t}} \frac{J_{m'}(k_0 n_{1t} a)}{J_m(k_0 n_{1t} a)} = \frac{1}{n_2} \frac{H_m^{(2)'}(k_0 n_2 a)}{H_m^{(2)}(k_0 n_2 a)} \quad (4)$$

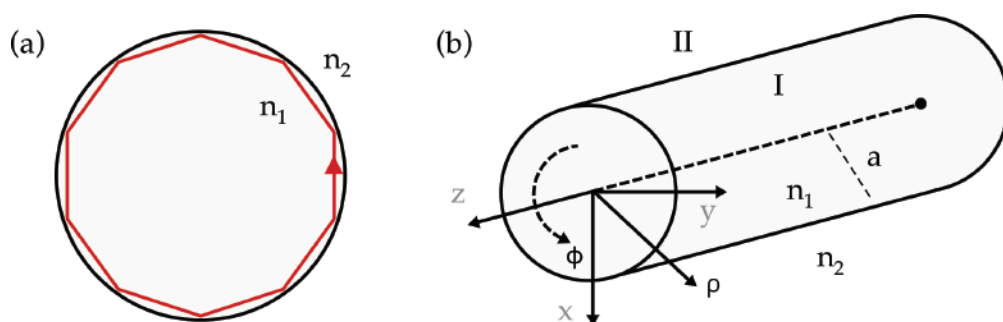


Figure 1.
 (a) Scheme of the WGM propagating azimuthally in the MR. (b) Cylindrical system of coordinates which shows the two regions considered in the problem.

In Eqs. (3) and (4), k_0 is the wavenumber in vacuum, $k_0 = 2\pi/\lambda$, J_m is the Bessel function of order m and J'_m is its first derivative, $H_m^{(2)}$ is the second class Hankel function of order m , and $H_m^{(2)'}$ is its first derivative. We have considered that the external medium does not present any anisotropy (in our case, it will be air).

By following this procedure, it is possible to calculate the dispersion curves of several WGMs propagating in a cylindrical, silica MR of $125\ \mu\text{m}$ diameter (the parameters of conventional optical fibers). Sellmeier dispersion of the silica was taken into account for the refractive index of the material. It is worth to note that the dispersion curves are not truly a curve, but a series of discrete solutions that have a particular radial order l and azimuthal order m . For a standard optical fiber and $1550\ \text{nm}$ optical wavelength, the azimuthal orders will be relatively high ($m \sim 300$). **Figure 2** shows the calculations of the resonant wavelengths for the first radial orders, as a function of the azimuthal order m for the TM polarization. The curves for the TE polarization follow the same trend, but the values of the resonant wavelengths are slightly different. By using Eq. (1), it is possible to relate the resonant wavelength with the effective index of the WGM resonance. For the azimuthal order $m = 360$ and the first radial order, $l = 1$, the resonant wavelengths and the effective indices of both polarization families are $\lambda_R^{\text{TM}} = 1508.25\ \text{nm}$, $n_{\text{eff}}^{\text{TM}} = 1.3826$ and $\lambda_R^{\text{TE}} = 1505.39\ \text{nm}$, $n_{\text{eff}}^{\text{TE}} = 1.3800$. Thus, the resonances for each polarization are not overlapped in wavelength.

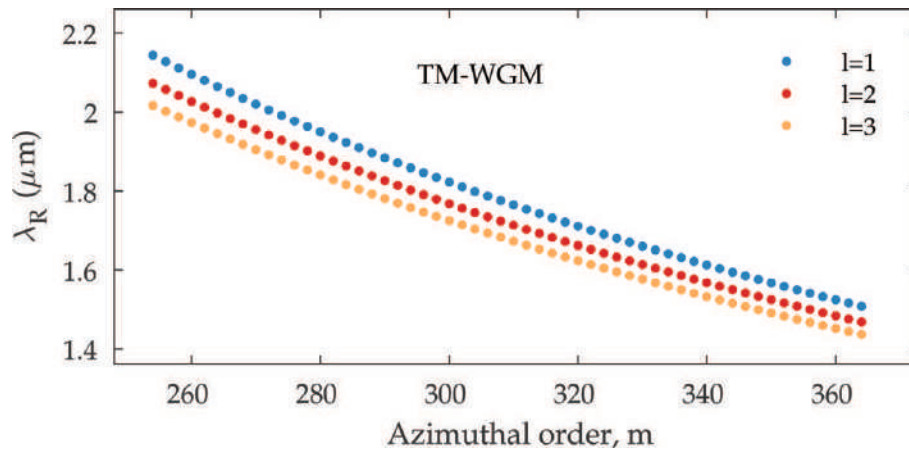


Figure 2. Resonant wavelength of WGMs with azimuthal orders from 250 to 370. Only a selection of the solutions to highlight their discrete nature is shown.

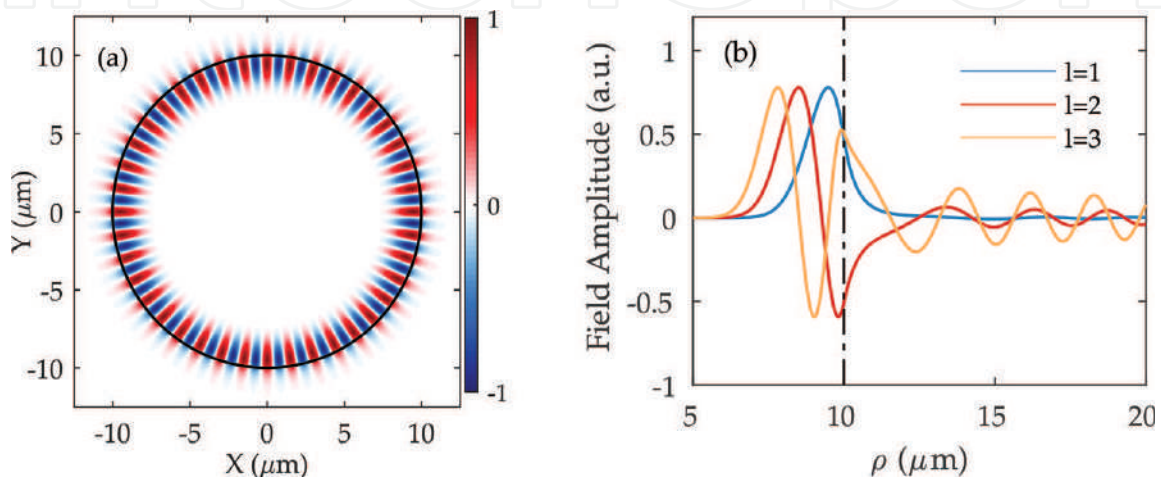


Figure 3. (a) Optical field of a $m = 40$ and $l = 1$ WGM in a silica, cylindrical MR. (b) Field amplitude of the WGM as a function of the radial coordinate, for $m = 40$ and $l = 1, 2, 3$.

Regarding the distribution of the fields, **Figure 3a** shows the amplitude of the electric field of the first radial order TM-WGM, propagating in a cylindrical, silica MR of $10\ \mu\text{m}$ diameter (the order m of the mode is 40; a low-order mode was considered in order to show the details of the field). As it can be observed, the field is well confined within the MR material (although its evanescent field is high enough to enable the use of these modes for sensing). As the azimuthal order of the WGM gets higher, the field will be more localized near the interface between the MR and the external medium. Also, it should be noted that, as the radial order of the WGM increases, the evanescent tail in the outer medium is larger; thus the quality factor of the correspondent resonance will be poorer. **Figure 3b** shows the field amplitude along the radial coordinate of the MR. As it can be observed, the optical power is localized in the outer region of the MR, near the interface, and shows a low-evanescent field in the outer medium, especially for the $l = 1$ mode.

3. Experimental setup

The general setup used in the experiments is shown in **Figure 4a**. The light source is a tunable diode, linearly polarized laser (TDL) with a narrow linewidth ($<300\ \text{kHz}$). The tuning range covers from 1515 to 1545 nm. The laser integrated a piezoelectric-based fine frequency tuning facility that allows continuous scanning of the emitted signal around a given wavelength, with subpicometer resolution. A polarization controller (PC) after the laser allows rotating the polarization of the light, and, as a consequence, it allows exciting TE- and TM-WGMs separately. The optical signal is then launched through an optical circulator, which enables measuring the WGM resonances in reflection by means of a photodetector (PD).

The MR will consist on a section of the bare optical fiber under test (FUT). Depending on the experiment, it will be a conventional telecom fiber, a rare-earth doped fiber, a photosensitive fiber, or a fiber where a grating has been previously inscribed. It is carefully cleaned and mounted on a three-axis flexure stage. WGMs are excited around the FUT by using the evanescent optical field of an auxiliary microtaper with a waist of $1\text{--}2\ \mu\text{m}$ in diameter and a few millimeters in length. This is not the only method that allows exciting WGMs in MRs: for example, one of the first techniques consisted on using a prism to excite the resonances in a spherical MR [15], but the efficiency was very poor. More recently, a fused-tapered fiber tip fabricated using a conventional fiber splicer was demonstrated to be capable of exciting WGMs in a cylindrical MR [16]. However, the highest efficiencies are achieved by using microtapers, with coupling efficiencies higher than 99% [8]. These microtapers are fabricated by the fuse-and-pull technique from conventional

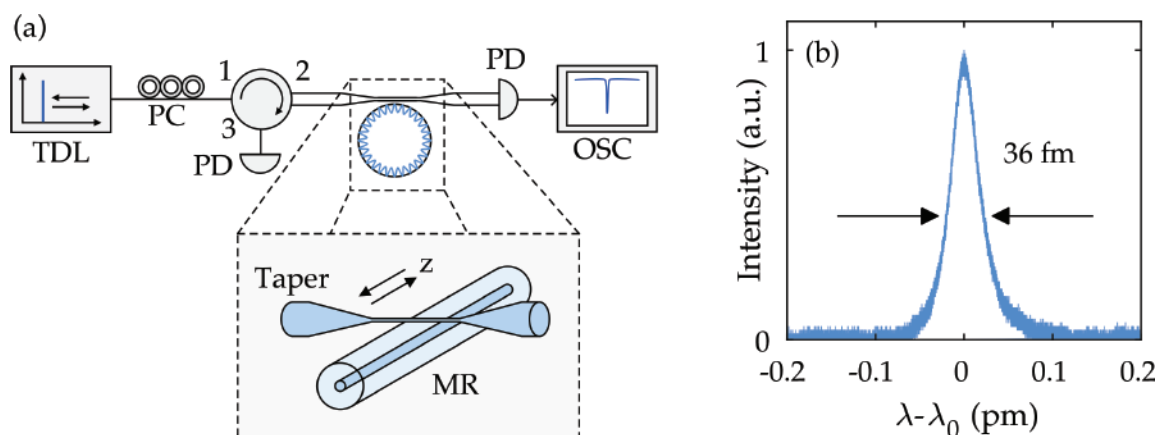


Figure 4.
(a) Scheme of the experimental setup. (b) Typical reflection spectrum of a WGM.

telecom fiber [17]. The microtaper and the MR are placed perpendicularly (see in the inset **Figure 4a**). Since the optical field of the WGMs is not axially localized (its extension is around $200 \mu\text{m}$ in length [7]), this setup allows exciting the WGM at different positions along the MR: by sweeping the microtaper along the MR, it is possible to detect variations of the parameters of the MR in the axial direction by measuring the shift of the resonances—radius [13, 18], temperature, or strain. Variations can be characterized along several centimeters of the MR.

The transmission of the taper was measured using a photodetector, and the signal was registered by an oscilloscope synchronized with the TDL. A typical transmission trace consists on a signal that will present a series of notches at the resonant wavelengths. For MRs of $125 \mu\text{m}$ in diameter, the free spectral range between two consecutive azimuthal orders m is $\sim 4 \text{ nm}$ at 1550 nm , and it is the same for both polarizations. **Figure 4b** shows the reflection spectrum of a resonance in an optical fiber ($a = 62.5 \mu\text{m}$): its linewidth is 36 fm , which corresponds to a Q -loaded factor of 4×10^7 .

As it was mentioned before, the position of the resonances will depend on the value of the refractive index of the material. In the next sections, we will study the characterization of different fibers and fiber components by means of the measurement of the shift of WGM resonances as the effective index of the MR is modified.

4. Measurement of temperature profiles in doped fibers and fiber gratings

When a silica fiber is heated up, two effects occur. First, the expansion of the fiber leads to a change of the diameter. Second, the thermo-optic effect induces a change in the refractive index of the material due to a variation of temperature. This variation modifies the spectral position of the WGM. From Eq. (1) it is possible to evaluate the shift of the resonant wavelength, $\Delta\lambda_R$, of a WGM due to a variation of temperature, ΔT :

$$\frac{\Delta\lambda_R}{\lambda_R} = \left(\frac{1}{a} \frac{da}{dT} + \frac{1}{n_{\text{eff}}} \frac{dn_{\text{eff}}}{dT} \right) \cdot \Delta T \quad (5)$$

In the case of optical fibers as MRs, it is a good approximation to assume that the thermo-optic coefficient (i.e., the second term in Eq. (5)) can be replaced by that of the pure silica, since the optical field of the WGMs is mainly localized in the fiber cladding (see **Figure 3**). The high sensitivity of WGMs to variations of temperature has been demonstrated for different geometries of the MR, such as microspheres [19, 20] or cylinders [21]. Moreover, the propagation of an optical signal of moderate power ($\sim 1 \text{ W}$ or higher) in a fiber generally induces a variation of temperature of the material. Due to the variation of temperature, the optical response of the fibers, or fiber components, may change when they are in operation. Thus, a detailed characterization of this effect is of interest to design properly the fiber-based optical systems. The use of WGMs allows achieving a very low detection limit: Rivera et al. claimed a detection limit of two thousandths of degree [21].

Here, we will present the characterization of temperature variations in two different examples: (i) rare-earth doped active fibers and (ii) fiber gratings inscribed in commercial photosensitive fibers.

4.1 Measurement of temperature in rare-earth doped fibers

Heating of rare-earth doped fibers can be an issue in fiber-based lasers and amplifiers. For example, thermal effects can be a limit to the maximum output

power that these systems can provide [22]. Another example is the shift in wavelength observed in distributed Bragg reflectors (DBR) and distributed feedback (DFB) lasers due to a pump-induced increment of temperature [23]. The heat is due to the non-radiative processes related to the electronic relaxation of some dopants: for example, this effect is less important in ytterbium-doped fibers, while Er/Yb-codoped and erbium-doped fibers exhibited a high increase of temperature with pump, due to its specific electronic-level system [24]. Thus, it is an intrinsic characteristic of the doped fibers that one needs to evaluate in order to design the proper optical system.

In the experiments presented here, several commercially available single-mode, core-pumped doped fibers from Fibercore were investigated. Specifically, the FUTs were three Er-doped fibers (DF-1500-F-980, M12-980/125, and I25-980/125), a Yb-doped fiber (DF-1100), and an Er/Yb-codoped fiber (DF-1500 Y). The values for absorption coefficients at the pump wavelength were 5.5 dB/m (DF-1500-F-980), 12 dB/m (M12-980/125), 21.9 dB/m (I25-980/125), 1000 dB/m (DF-1100), and 1700 dB/m (DF-1100). Short sections of ~ 2 cm in length of each FUT were used as the MR where the WGMs were excited. The FUTs were pumped with a single-mode, fiber-pigtailed laser diode that emitted a maximum power of 380 mW at 976 nm. As the pump launched to the FUT was increased, the WGM resonance shifted toward longer wavelengths in all cases, as it was expected, since the thermo-optic and the thermal expansion coefficients of silica are both positives. As an example, **Figure 5** shows the shift in wavelength of a resonance as a function of the pump launched to the fiber DF-1500-F-980. In our experiments, we did not investigate in detail the temporal response of the phenomenon, which will be ruled by the mechanisms that convert the pump power to heat, the heat conduction in silica, and the transfer of heat to the air. Typically, it will be on the range of a few tens of microseconds [25].

At this point, several features of this technique must be clarified. First, it is worth to point out that the shift in wavelength is virtually independent of the particular resonance used for the measurements, that is, it does not depend on its radial and azimuthal order nor on its polarization. The sensitivity to thermal variations of different WGM resonances was theoretically calculated around $1.53 \mu\text{m}$, taking into account both the thermal expansion of the fiber and the thermo-optic effect. The results showed that the difference in sensitivity between different resonances differs in less than 1/10000 per each $^{\circ}\text{C}$ of temperature increase. This simplifies the utility of this technique.

The second aspect to highlight is related to the fact that the dopants in the active fibers are located in their core, while WGMs are highly confined in the outer region of the cladding (see **Figure 3**). From the study of heat conduction in doped fibers

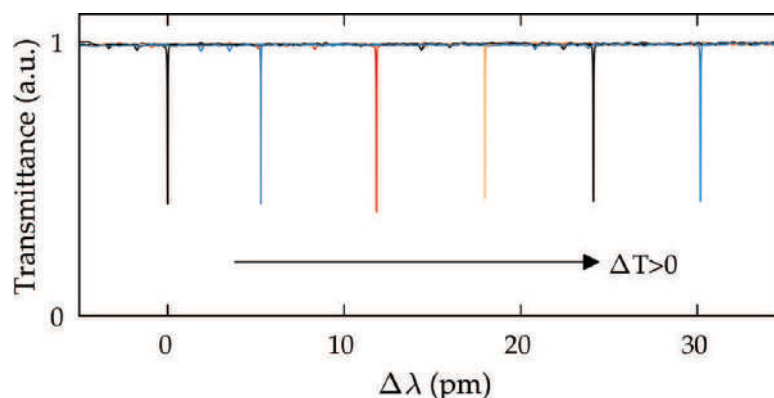


Figure 5. Wavelength shift of the resonant wavelength as the pump power is increased. From left to right: pump power 0 mW, 40 mW, 110 mW, 180 mW, 270 mW, and 370 mW.

carried out by Davis et al. [25], it is possible to calculate that, at the steady state, the increase of temperature at the core of the fiber is just 1.5% larger than at the outer surface.

In order to calibrate the shift in wavelength of the WGM resonances with the heating, a FBG inscribed in the core of a doped fiber was used for comparison. The procedure is described in [21]. The WGM resonances shift at a rate of $8.2 \text{ pm}/^\circ\text{C}$. With this calibration, it is possible to correlate the shifts in wavelength with the increase of temperature in the core of the fiber. For the example shown in **Figure 5**, the maximum increment of temperature achieved for a pump of 370 mW was 3.7°C .

Figure 6 summarizes the measurements performed for the different doped fibers. A similar trend can be observed in all the cases; the resonances shift fast in wavelength for low pump powers, and, beyond certain pump, heating tends to saturate. It can be observed that the Yb fiber DF 1100 shows a similar increase of temperature to those of the Er-doped fibers, although the concentration of the dopants in the Yb fiber is much larger (note the absorption coefficient around 975 nm). Also, the highest temperature increment corresponds to the Er/Yb-doped fiber (DF 1500 Y), despite that it shows a lower absorption coefficient than its equivalent Yb-doped fiber (DF 1100). These results are in accordance to the fact that the heating is related to the existence of non-radiative transitions for the relaxation of electrons in the active medium.

4.2 Measurement of temperature profiles in fiber components

As it was mentioned before, WGMs are axially localized: their extension along the fiber is $\sim 200 \mu\text{m}$, typically, for a MR of $62.5 \mu\text{m}$. Thus, this technique provides spatial resolution. The taper can be swept along the MR in order to characterize the parameters of the FUT point to point. This feature was used in order to characterize the temperature profile along fiber components [26].

The FBGs used in the experiments were written in germanium-silicate boron codoped, photosensitive fibers from Fibercore, using a doubled-argon UV laser and a uniform phase mask. The length of all the gratings was $\sim 10 \text{ mm}$. The WGMs were excited at different positions along the FBG, and, simultaneously, it was illuminated by optical signals of moderate powers, within or outside of the

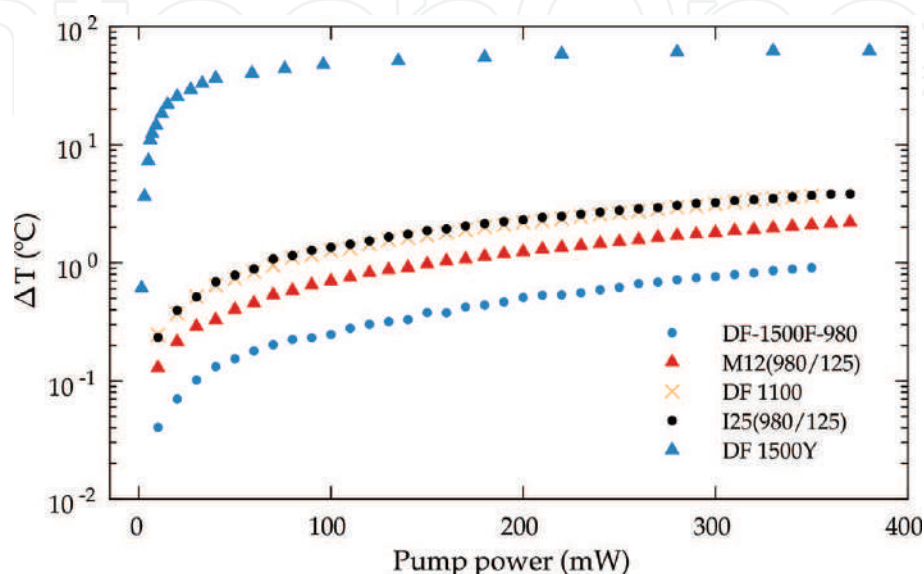


Figure 6.
Heating of the doped fibers as a function of pump power.

reflection band but in the vicinities of the Bragg wavelength. This illumination signal was provided by an amplified tunable laser (range, 1520–1560 nm) that provided up to 1 W of CW light.

As a preliminary experiment, a section of fiber Fibercore PS980 was uniformly irradiated (i.e., there was no grating inscribed). The length was 5 mm, and the UV fluence power used in the irradiation was 150 J/mm². The wavelength shift of the resonances was measured as the MR was illuminated with a 1550 nm optical signal, compared to the original position of the resonances, with no illumination along the FUT. **Figure 7a** shows the results. The data show a clear difference between the irradiated length ($z < 3$ mm) and the non-irradiated length ($z > 3$ mm). A temperature gradient in an intermediate region due to the heat conduction in silica and the transfer of heat to the air can be observed. It should be noted that this section is far larger than the length of the focused UV beam ($\sim 700 \mu\text{m}$); thus, the beam size is not the cause of this transition length. In the irradiated section, the temperature increases at a rate higher than 10 °C/W, for this sample, while the pristine fiber heats up at a rate lower than 1 °C/W. The increment of temperature was linear with power in the available power range. This experiment avails that this technique allows characterizing the variations of temperature along the components with a resolution of tenths of a millimeter. This feature is useful when one needs to detect, evaluate, and correct smooth undesired non-homogeneities that may occur during the fabrication of FBG and LPG, which are usually short components. As an example, **Figure 7b** shows the measurement of the temperature profile of a section of an irradiated fiber (length, 5 mm) that suffered from some misalignment during the UV irradiation process. For this sample, a variation of 4 °C is measured in such a short irradiated length.

The temperature profile along a FBG with strong reflectivity was measured using this technique. The FBG had a reflectivity higher than 99.9%; the Bragg wavelength was 1556 nm, its length was 12 mm, and it was fabricated in PS1250 fiber (Fibercore). First, the illumination signal was tuned well outside the reflection band, at 1540 nm; in this case, there is no reflection of the optical signal; it just propagates through the FBG. The power launched to the MR was 800 mW. Curve (i) in **Figure 8** shows the obtained results. As expected, a similar result to the case shown in **Figure 7a** was obtained: the heating over the length of the FBG was fairly constant, ~ 5.5 °C. It should be noted that the axial resolution of the technique will be larger than the grating period. Then, the average increment of temperature should be similar to that introduced in the case of the uniformly irradiated fiber, for

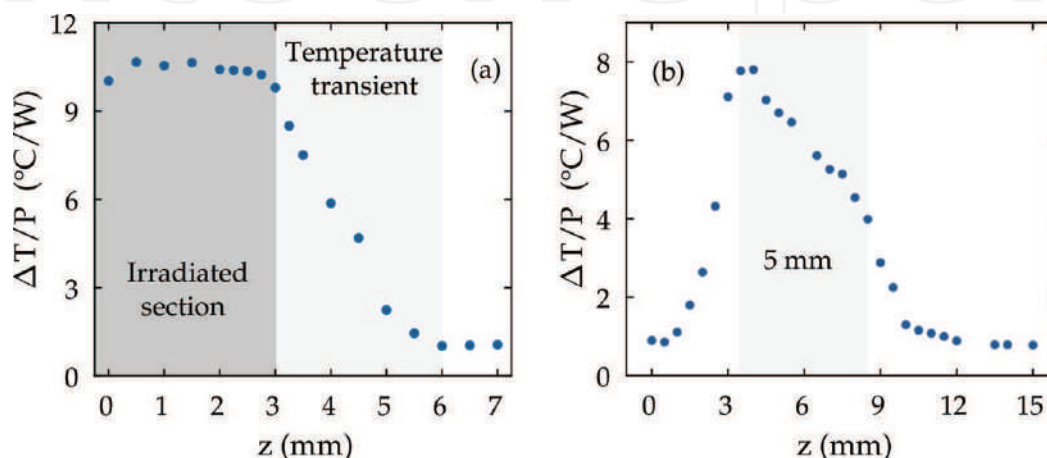


Figure 7.
 Temperature profile of irradiated FUTs, (a) uniformly and (b) nonuniformly.

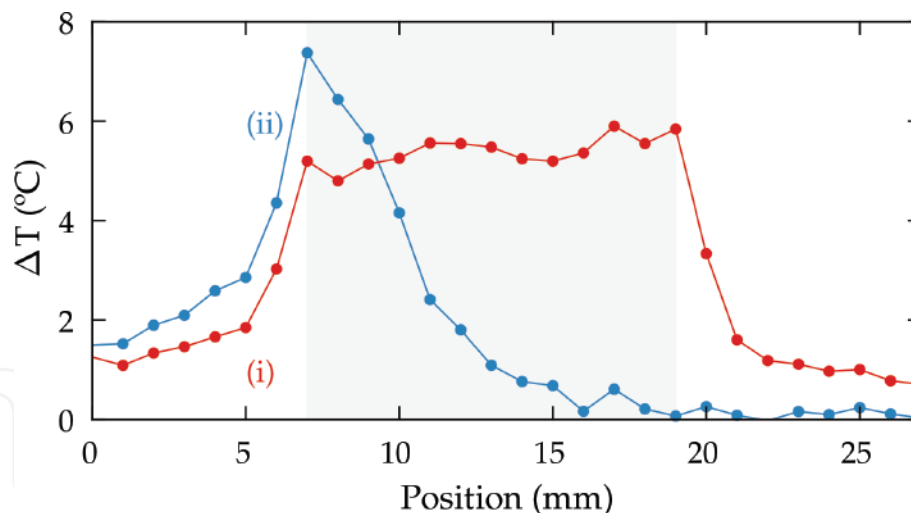


Figure 8.
Temperature profile of a FBG illuminated (i) outside and (ii) within the reflexion band.

the same UV fluence and fiber characteristics. Two transition zones were clearly observed at both ends of the grating.

Finally, the temperature profile was measured when the optical signal was tuned to the Bragg wavelength (power, 1 W) (see curve (ii) in **Figure 8**). In this case, one should take into account that the UV irradiation is constant over its length, and the gradient temperature is due to the fact that the optical signal is reflected as it penetrates into the grating. A sharp increment of temperature at the beginning of the grating, at the extreme that is illuminated, can be observed. The maximum is located at the vicinities of the point where the FBG begins. The decay of temperature extends over a length of ~ 5 mm, which is shorter than the length of the fiber itself (12 mm). This is consistent with the high reflectivity of this FBG. Moreover it should be noted that, at the beginning of the curve, that is, $z = 0 - 3$ mm, the temperature increase is ~ 2 °C, that is, roughly twice the value obtained for a pristine fiber. On the contrary, in the section after the grating (and even at the last millimeters of the FBG), the increment of temperature is below the detection limit of the technique. The origin of this asymmetry is the reflection of the optical signal: the amount of light that reaches the last millimeters of the FBG is very small. This technique, then, provides information about the effective length of gratings of different reflectivity, information that could be relevant for the design of optical systems that require of short cavities, or cavities that require of a very precise length, as in the case of mode-locked fiber lasers.

5. Measurement of absorption coefficients in photosensitive fibers

In the previous section, the gradient of temperature induced in fiber-optic components by means of an illumination signal has been characterized and discussed. It has been shown that there is a difference in temperature between the sections that have been irradiated with UV light compared to the pristine fibers. It is well known that the UV irradiation induces a change in the index of photosensitive fibers, which is employed to fabricate FBGs and LPGs. According to Kramers-Kronig relations, the change in the refractive index is associated with a variation of the absorption coefficient. In addition, the exposure of the fiber to the levels of UV light usually employed in the grating fabrication induces mechanical deformations in the fiber [27]. This leads to an increase of the loss due to scattering. Thus, when a

fiber is UV irradiated, its loss, α , increases due to two causes: absorption that will be quantified by α^{abs} and scattering, α^{scat} .

The increase of α introduced by UV irradiation has been measured before [28], since this is a parameter of interest to optimize the fabrication of FBGs, especially in the case of long or superimposed gratings with many reflection bands [29, 30]. This measurement provides information about an averaged value of the attenuation loss along the irradiated section, which includes both the absorption and the scattering contributions. The technique based on the measurement of the shift of WGM resonances will only measure the absorption coefficient; thus, by combining the two types of measurements, it is possible to evaluate both contributions separately.

Different types of photosensitive fibers were studied [11]: (i) Fibercore PS980, (ii) Fibercore PS1250, (iii) Fibercore SM1500, and (iv) Corning SMF28; this fiber was hydrogenated for 15 days (pressure: 30 bar) to increase its photosensitivity. The setup used in the experiments was the same than in the previous experiments shown in this chapter. In this case, the FUTs were short sections of the different fibers, which were exposed to a UV fluence of 150 J/mm². Similar temperature profiles to that shown in **Figure 7a** were obtained for all of them, but with different temperature increments, since the photosensitivity was also different for each of them.

The different increases of temperature between the irradiated fiber and the pristine fiber will provide us information to quantify the variation in the α^{abs} due to UV irradiation. It will be assumed that the heating over the transversal section of the fiber, at a given axial position, is set by the absorption coefficient, α^{abs} . According to the analysis reported by Davis et al. [25], the heating at the steady state, ΔT , will be given by

$$\frac{\Delta T}{P} = \frac{1}{2\pi ah} \alpha^{\text{abs}} \quad (6)$$

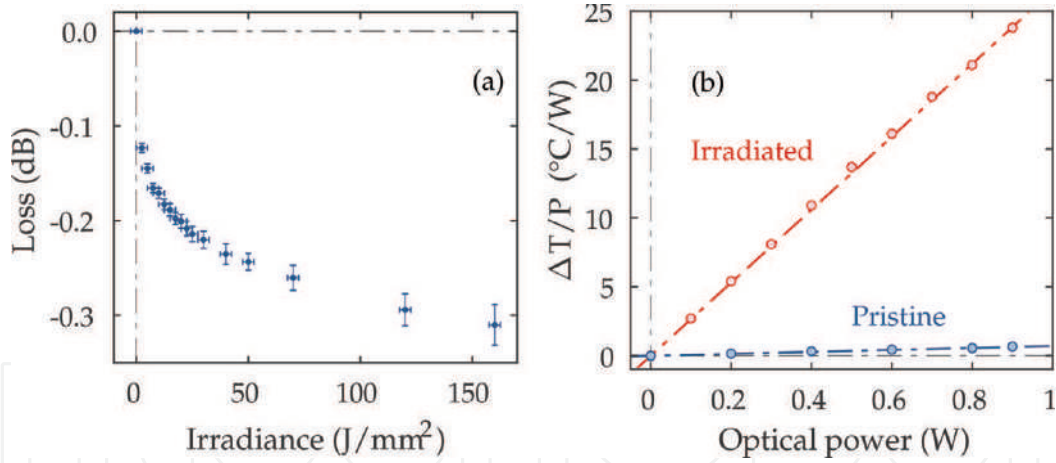
where h is the heat transfer coefficient ($81.4 \text{ W} \cdot \text{m}^{-2} \cdot \text{K}^{-1}$ for a silica fiber). Then, the ratio of ΔT between two different points along the FUT, 1 and 2, is given by

$$\frac{\Delta T_2}{\Delta T_1} = \frac{\alpha_2^{\text{abs}}}{\alpha_1^{\text{abs}}} \quad (7)$$

Thus, with this analysis and the experimental data obtained from the measurement of the wavelength shift of WGM resonances in irradiated points (1) and pristine points (2) of the FUT, this ratio between the respective α^{abs} can be calculated.

Direct measurements of transmission loss variation as the fibers were irradiated were carried out for a PS980 fiber. First, the value of the loss of the pristine fiber was measured at 1550 nm by means of the cutback method: the obtained value was 120.0 ± 0.5 dB/km. Then, the UV laser was swept back and forth along a 5-cm-long section of the fiber, repeatedly. The full description of the procedure is described in [11]. **Figure 9a** shows the data obtained in this experiment. The final loss was 6.2 ± 0.4 dB/m; thus the ratio between the loss coefficients, α_2/α_1 , increased 52 ± 3 times. Please remember that this loss coefficient includes both absorption and scattering contributions ($\alpha = \alpha^{\text{abs}} + \alpha^{\text{scat}}$).

The contribution to the loss by means of the absorption mechanism was measured using the WGM technique (see **Figure 9b**). In this case, a 1550 nm laser (maximum power, 1 W) was launched to the FUT, and the thermal shift of the


Figure 9.

(a) Direct measurement of the loss as the PS980 fiber is irradiated. (b) Heating of the PS980 fiber as a function of the illumination power.

	WGM technique			Direct measurements		
	$1 - \alpha_2^{\text{abs}}/\alpha_1^{\text{abs}}$	$\Delta T/P$ ($^{\circ}\text{C}/\text{W}$)		α_2/α_1	α (dB/km)	
		Irradiated	Pristine		Irradiated	Pristine
PS980	36.9 ± 0.7	26.48 ± 0.15	0.718 ± 0.014	52 ± 3	6200 ± 400	120 ± 2^3
PS1250	40.1 ± 0.8	30.80 ± 0.17	0.768 ± 0.014	50 ± 3	6600 ± 400	131.1^4
SM1500	$>40^1$	1.20 ± 0.03	$< 0.03^2$	190 ± 50	370 ± 90	1.95^4
H ₂ -SMF28	28.8 ± 0.5	23.48 ± 0.13	0.815 ± 0.012	n/a ²	5600 ± 400	n/a ¹

¹Nonavailable.

²Below detection limit.

³Cutback measurement.

⁴Nominal value.

Table 1.

Measurement of thermal heating and loss coefficient of different fibers.

resonances was measured as the laser power was increased, at two different points, one within the irradiated section and one outside it. The data does not show any sign of saturation of the heating, at this range of power. The temperature of the irradiated section increased linearly, at a rate of 26.48 ± 0.15 $^{\circ}\text{C}/\text{W}$, and at 0.718 ± 0.014 $^{\circ}\text{C}/\text{W}$ in the pristine region. The ratio between these values, that is, the ratio $\alpha_2^{\text{abs}}/\alpha_1^{\text{abs}}$, is 36.9 ± 0.7 $^{\circ}\text{C}/\text{W}$.

This process was repeated for all the different fibers mentioned before: PS1250, SM1500, and hydrogenated SMF28, at 1550. **Table 1** includes the results from the measurements and the corresponding analysis: α_2/α_1 was obtained for each of them from the direct measurement of the loss, while $\alpha_2^{\text{abs}}/\alpha_1^{\text{abs}}$ was calculated from the technique based in WGMs.

The results, compiled in **Table 1**, allow establishing several conclusions of interest. First, as expected, the absorption coefficient is substantially increased due to the UV irradiation. As a consequence, even for signals of moderate powers, FBGs might experience shifts and chirps that should be taken into account [31]. Second, the results show that α_2/α_1 is systematically higher than $\alpha_2^{\text{abs}}/\alpha_1^{\text{abs}}$. Roselló-Mechó et al. analyzed the measurements to demonstrate that these results lead to the conclusion that scattering loss increases at a higher rate than absorption loss [11].

Finally, Eq. (6) can be used to calculate the absolute value of the absorption and scattering coefficients by taking into account the values of h and a for a silica

	α^{abs} (dB/km)		α^{scat} (dB/km)	
	Irradiated	Pristine	Irradiated	Pristine
PS980	3680 ± 20	99.7 ± 1.9	2500 ± 400	20 ± 3
PS1250	4280 ± 20	106.6 ± 1.9	2300 ± 400	24.5 ± 1.9
SM1500	167 ± 4	$< 1.95^1$	200 ± 90	$< 1.95^1$
H ₂ -SMF28	3260 ± 18	113.1 ± 1.7	2300 ± 400	n/a ²

¹Nominal value.

²Nonavailable, hydrogenated fiber.

Table 2.
 Absorption and scattering contributions to the overall attenuation coefficient.

fiber [25] and the measurements of α . The results of the contributions are compiled in **Table 2**. Both contributions are in the same order of magnitude, but α^{scat} is smaller for three of the four FUTs. These values confirm that scattering loss increases faster than absorption loss.

Thus, by means of the combination of both techniques, it is possible to quantify the different contributions to the loss, even for short sections of fiber. This information might be useful, for example, in the design of novel-active doped fibers, since it is possible to evaluate if the doping technique increases the scattering loss unnecessarily, but not so much the absorption.

6. Measurement of Pockels coefficients in optical fibers

The elasto-optic effect consists on the variation in the refractive index generated by any strain applied to the fiber. The correspondent elasto-optic coefficients are usually determined by measuring the optical activity induced by a mechanical twist and the phase change induced by longitudinal strain [32, 33]. This technique relies on the use of the conventional axial modes propagating through the fiber. Since these modes are essentially transverse to the axis of the fiber [34], the anisotropy of the elasto-optic effect does not show up. On the contrary, WGMs have a significant longitudinal component; hence, their optical fields experience the anisotropy of the elasto-optic effect intrinsically. In the last years, researchers have demonstrated a number of fiber devices in which the longitudinal components of the electromagnetic modes are significant, such as microfibers [35] and microstructured optical fibers with a high air-filling fraction [36]. For these cases, the measurement and characterization of the anisotropy of the elasto-optic effect and its Pockels coefficients are of high interest. Roselló-Mechó et al. reported a technique based on the different wavelength shifts of TE- and TM-WGM resonances in a fiber under axial strain, to measure these coefficients [37]. This technique has the additional advantage that, since it does not involve the conventional modes of the fiber, there is no need that the FUTs are single mode in order to carry out the measurements. Then, the coefficients can be measured at different wavelengths to determine their dispersion; this is a limitation of the usual technique based on the optical activity which is overcome by means of WGM technique [38].

According to Eq. (1), a variation in the refractive index will tune the WGM resonances in wavelength. In this case, an axial strain will be applied to the FUT in order to induce this variation in the index, due to the elasto-optic effect. This feature was applied in different works in order to tune the WGM resonances

[39, 40]. However, there was not any mention to the different behaviors of TE- and TM-WGM.

An axial strain introduces a refractive index perturbation in an isotropic, cylindrical MR, due to the elasto-optic effect, which will be different for the axial (Δn_z) and transversal directions (Δn_t):

$$\frac{\Delta n_t}{n_0} = -p_{et} \varepsilon; \quad p_{et} \equiv \frac{n_0^2}{2} (p_{12} - \nu(p_{11} + p_{12})), \quad (8)$$

$$\frac{\Delta n_z}{n_0} = -p_{ez} \varepsilon; \quad p_{ez} \equiv \frac{n_0^2}{2} (p_{11} - 2\nu p_{12}), \quad (9)$$

where n_0 is the unperturbed index of the MR, p_{ij} are the elasto-optic coefficients, ν is Poisson's ratio, and ε is the strain applied to the MR. The coefficients p_{et} and p_{ez} are the effective elasto-optic coefficients, which are defined for simplicity. According to the reported values for the elasto-optic coefficients for fused silica ($p_{11} = 0.121$, $p_{12} = 0.27$ [41], $\nu = 0.17$ [42]), the ratio $\Delta n_t/\Delta n_z \approx 6.97$; hence, it is expected that the strain introduces a significant differential anisotropy. With this in mind, Maxwell's equations will be solved considering the uniaxial tensor given by Eq. (2). The solutions, as mentioned before, split in two families of WGM, the TE and TM modes, whose resonant frequencies will be obtained by solving Eqs. (3) and (4).

The refractive index perturbation is not the only factor to take into account when evaluating the wavelength shift of WGM resonances due to strain: the radius a of the MR also varies with it according to Poisson's ratio, $\Delta a/a = -\nu\varepsilon$.

With all these ideas in mind, the relative shift of the WGM resonances, $\Delta\lambda_R/\lambda_R$, can be characterized as a function of the strain, for TE- and TM-WGMs. **Figure 10a** shows an example of the anisotropic behavior of TE- and TM-WGM. The strain applied to the MR was $330 \mu\varepsilon$ for both polarizations, and the measured wavelength shift was different for each of them: 0.18 nm for TE-WGM and 0.11 nm for TM-WGM. $\Delta\lambda_R/\lambda_R$ was measured as a function of the strain in detail at 1531 nm , for both polarizations; the results are shown in **Figure 10b**. A linear trend in both cases can be observed: the slopes of the linear regressions that fit the experimental values are $s_{TE} = -0.369 \pm 0.006 \mu\varepsilon^{-1}$ for the TE- and $s_{TM} = -0.201 \pm 0.004 \mu\varepsilon^{-1}$ for the TM-WGM. The ratio $s_{TE}/s_{TM} = 1.84$ shows the anisotropy of the elasto-optic effect. From these values, it is possible to calculate the elasto-optic coefficients p_{ij} with its uncertainties (see [37] for a more detailed description of the procedure), by taking

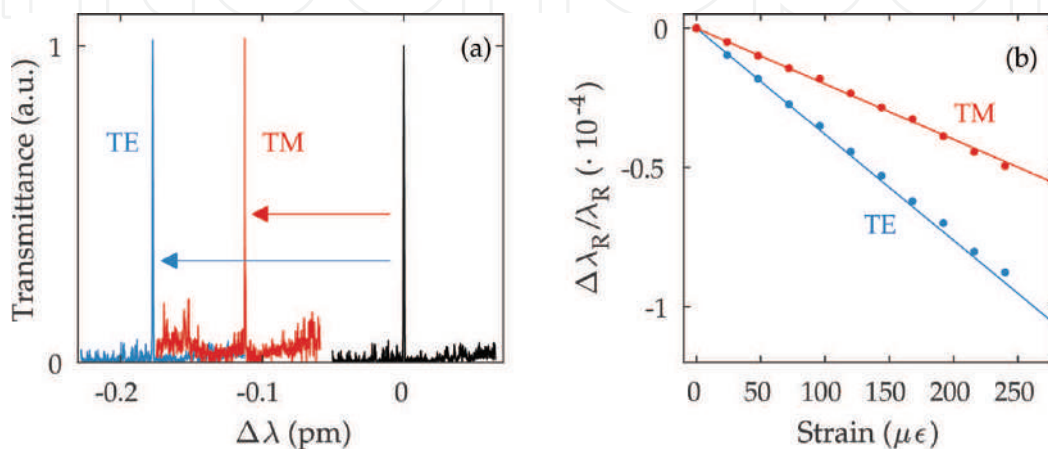


Figure 10.

(a) Wavelength shift of TE-/TM-WGM resonances for $\varepsilon = 330 \mu\varepsilon$. (b) Measurement of the wavelength shift as a function of the strain.

	Present work		Literature
	1531 nm	1064 nm	
p_{11}	0.116	0.131	0.113 @ 633 nm [32] 0.121 @ 633 nm [41]
p_{12}	0.255	0.267	0.252 @ 633 nm [32] 0.270 @ 633 nm [41]

Table 3.
 Comparison of experimental p_{ij} values with those reported in the literature.

into account the Sellmeier coefficients for the value of the refractive index at 1531 nm and Poisson's ratio of $\nu = 0.17 \pm 0.01$.

The measurements were repeated at 1064 nm, to study the dispersion of the elasto-optic effect. Results at both wavelengths are compiled in **Table 3** and are compared with those reported in the literature. Both sets of measurements are in good agreement, and the small differences might be due to the fact that the technique based in WGM measures the p_{ij} of the cladding material (i.e., fused silica), while in the case of the other techniques, the coefficients are determined by the material of the fiber core, which is usually silica doped with other elements.

7. Conclusions

In this chapter, we described a technique based on the excitation of WGMs around cylindrical MRs, to measure properties of the MR material. The resonant nature of the WGMs confers this technique with high sensitivity and low detection limits. Also, the technique allows measuring these parameters with axial resolution; hence, it is possible to detect changes of the parameters point to point along the MR.

The technique has been applied to different experiments. Mainly, thermo-optic effect and elasto-optic effect have been investigated in silica fibers. The variation in the index, due to a change in the temperature or strain, rules the shift in wavelength of the WGM resonances. When the technique was applied to different types of fibers and components, different information were obtained from the experiments. In particular, we measure temperature profiles in pumped, rare-earth doped fibers and in FBGs; the absorption coefficient in irradiated photosensitive fibers; and the Pockels coefficients in telecom fibers. Novel results were obtained: for example, it was possible to measure absorption and scattering loss coefficients separately, and, also, the anisotropy of the elasto-optic effect was observed experimentally. The information provided by the WGM-based technique might help to optimize the fabrication procedures of doped fibers and fiber components as FBGs or LPGs.

Acknowledgements

This work was funded by Ministerio de Economía y Competitividad of Spain and FEDER funds (Ref: TEC2016-76664-C2-1-R) and Generalitat Valenciana (Ref: PROMETEOII/2014/072), Universitat de València (UV-INV-AE16-485280). X. Roselló-Mechó's contract is funded by the FPI program (MinECo, Spain, BES-2014-068607). E. Rivera-Pérez's contract is funded by the Postdoctoral Stays in Foreigner Countries (291121, CONACYT, Mexico).

IntechOpen

Author details

Martina Delgado-Pinar*, Xavier Roselló-Mechó, Emmanuel Rivera-Pérez,
Antonio Díez, José Luis Cruz and Miguel V. Andrés
Applied Physics Department, Science Materials Institute, University of Valencia,
Valencia, Spain

*Address all correspondence to: martina.delgado@uv.es

IntechOpen

© 2018 The Author(s). Licensee IntechOpen. This chapter is distributed under the terms of the Creative Commons Attribution License (<http://creativecommons.org/licenses/by/3.0>), which permits unrestricted use, distribution, and reproduction in any medium, provided the original work is properly cited. 

References

- [1] Rayleigh L. The Theory of Sound. Vol. 2. London: Macmillan; 1896
- [2] Mie G. Beiträge zur Optik trüber Medien, speziell kolloidaler Metallösungen. *Annalen der Physik*. 1908;**330**(3):377-445. DOI: 10.1002/andp.19083300302
- [3] Debye P. Der Lichtdruck auf Kugeln von beliebigem Material. *Annalen der Physik*. 1909;**335**(11):57-136. DOI: 10.1002/andp.19093351103
- [4] Richtmyer RD. Dielectric resonators. *Journal of Applied Physics*. 1939;**10**(6): 391-398. DOI: 10.1063/1.1707320
- [5] Stratton JA. *Electromagnetic Theory*. 1st ed. New York: McGraw-Hill; 1941
- [6] Braginsky VB, Gorodetsky ML, Ilchenko VS. Quality-factor and nonlinear properties of optical whispering-gallery modes. *Physics Letters A*. 1989;**137**(7):393-397. DOI: 10.1016/0375-9601(89)90912-2
- [7] Sumetsky M. Mode localization and the Q-factor of a cylindrical microresonator. *Optics Letters*. 2010; **35**(14):2385-2387. DOI: 10.1364/OL.35.002385
- [8] Knight JC, Cheung G, Jacques F, Birks TA. Phase-matched excitation of whispering-gallery-mode resonances by a fiber taper. *Optics Letters*. 1997; **22**(15):1129-1131. DOI: 10.1364/OL.22.001129
- [9] Gorodetsky ML, Savchenkov AA, Ilchenko VS. Ultimate Q of optical microsphere resonators. *Optics Letters*. 1996;**21**(7):453-455. DOI: 10.1364/OL.21.000453
- [10] Armani DK, Kippenberg TJ, Spillane SM, Vahala KJ. Ultra-high-Q toroid microcavity on a chip. *Nature*. 2003; **421**:925-928. DOI: 10.1038/nature01371
- [11] Roselló-Mechó X, Delgado-Pinar M, Cruz JL, Díez A, Andrés MV. Measurement of UV-induced absorption and scattering losses in photosensitive fibers. *Optics Letters*. 2018;**43**(12): 2897-2900. DOI: 10.1364/OL.43.002897
- [12] Armani AM, Kulkarni RP, Fraser SE, Flagan RC, Vahala KJ. Label-free, single-molecule detection with optical microcavities. *Science*. 2007;**317**(5839): 783-787. DOI: 10.1126/science.1145002
- [13] Birks TA, Knight JC, Dimmick TE. High-resolution measurement of the fiber diameter variations using whispering gallery modes and no optical alignment. *IEEE Photonics Technology Letters*. 2000;**12**(2):182-183. DOI: 10.1109/68.823510
- [14] Rivera-Pérez E. *Microcavidades ópticas cilíndricas y sus aplicaciones [thesis]*. Universidad Autónoma de San Luis de Potosí-IICO; 2015. pp. 1-84
- [15] Schiller S, Byer RL. High-resolution spectroscopy of whispering gallery modes in large dielectric spheres. *Optics Letters*. 1991;**16**(15):1138-1140. DOI: 10.1364/OL.16.001138
- [16] Arques L, Carrascosa A, Zamora V, Díez A, Cruz JL, Andrés MV. Excitation and interrogation of whispering-gallery modes in optical microresonators using a single fused-tapered fiber tip. *Optics Letters*. 2011;**36**(17):3452-3454. DOI: 10.1364/OL.36.003452
- [17] Kenny RP, Birks TA, Oakley KP. Control of optical fibre taper shape. *Electronics Letters*. 1991;**27**(18): 1654-1656. DOI: 10.1049/el:19911034
- [18] Sumetsky M, Dulashko Y. Radius variation of optical fibers with angstrom

- accuracy. *Optics Letters*. 2010;**35**(23): 4006-4008. DOI: 10.1364/OL.35.004006
- [19] Guan G, Arnold S, Otugen V. Temperature measurements using a microoptical sensor based on whispering gallery modes. *AIAA Journal*. 2006;**44**(10):2385-2389. DOI: 10.2514/1.20910
- [20] Ma Q, Rossmann T, Guo Z. Temperature sensitivity of silica microresonators. *Journal of Physics D: Applied Physics*. 2008;**41**(24):245111. DOI: 10.1088/0022-3727/41/24/245111
- [21] Rivera-Pérez E, Villegas IL, Díez A, Andrés MV, Cruz JL, Rodríguez-Cobos A. Measurement of pump-induced temperature increase in doped fibers using whispering-gallery modes. *IEEE Photonics Technology Letters*. 2013;**25**(24):2498-2500. DOI: 10.1109/LPT.2013.2288865
- [22] Wang Y, Xu CQ, Hong P. Thermal effects in kilowatt fiber lasers. *IEEE Photonics Technology Letters*. 2004; **16**(1):63-65. DOI: 10.1109/LPT.2003.818913
- [23] Haderler O, Ibsen M, Zervas MN. Distributed-feedback fiber laser sensor for simultaneous strain and temperature measurements operating in the radio-frequency domain. *Applied Optics*. 2001;**40**(19):3169-3175. DOI: 10.1364/AO.40.003169
- [24] MJF D. Rare-earth-doped fiber lasers and amplifiers, revised and expanded. In: *Optical Science and Engineering*. Boca Raton: Taylor & Francis; 2001
- [25] Davis MK, Digonnet MJF, Pantell RH. Thermal effects in doped fibers. *Journal of Light-Wave Technology*. 1998;**16**(6):1013-1023. DOI: 10.1109/50.681458
- [26] Delgado-Pinar M, Villegas IL, Díez A, Cruz JL, Andrés MV. Measurement of temperature profile induced by the optical signal in fiber Bragg gratings using whispering-gallery modes. *Optics Letters*. 2014;**39**(21):6277-6280. DOI: 10.1364/OL.39.006277
- [27] Poumellec B, Guénot P, Riant I, Sansonetti P, Niay P, Bernage P, et al. UV induced densification during Bragg grating inscription in Ge: SiO₂ preforms. *Optical Materials*. 1995;**4**(4):441-449. DOI: 10.1016/0925-3467(94)00114-6
- [28] Canning J, Åslund M, Hu PF. Ultraviolet-induced absorption losses in hydrogen-loaded optical fibers and in presensitized optical fibers. *Optics Letters*. 2000;**25**(22):1621-1623. DOI: 10.1364/OL.25.001621
- [29] Arigiris A, Konstantaki M, Ikiades A, Chronis D, Florias P, Kallimani K, et al. Fabrication of high-reflectivity superimposed multiple-fiber Bragg gratings with unequal wave-length spacing. *Optics Letters*. 2002;**27**(15): 1306-1308. DOI: 10.1364/OL.27.001306
- [30] Gagné M, Loranger S, Lapointe J, Kashyap R. Fabrication of high quality, ultra-long fiber Bragg gratings: Up to 2 million periods in phase. *Optics Express*. 2014;**22**(1):387-398. DOI: 10.1364/OE.22.000387
- [31] Lauzon J, Thibault S, Martin J, Ouellette F. Implementation and characterization of fiber Bragg gratings linearly chirped by a temperature gradient. *Optics Letters*. 1994;**19**(23): 2027-2029. DOI: 10.1364/OL.19.002027
- [32] Bertholds A, Dandliker R. Determination of the individual strain-optic coefficients in single-mode optical fibres. *Journal of Lightwave Technology*. 1988;**6**(1):17-20. DOI: 10.1109/50.3956
- [33] Dragic PD, Ballato J, Morris S, Hawkins T. Pockels' coefficients of alumina in aluminosilicate optical fiber. *Journal of the Optical Society of*

America B: Optical Physics. 2013;**30**(2): 244-250. DOI: 10.1364/JOSAB.30.000244

[34] Bertholds A, Dandliker R. Deformation of single-mode optical fibers under static longitudinal stress. *Journal of Lightwave Technology*. 1987; **5**(7):895-900. DOI: 10.1109/JLT.1987.1075583

[35] Skelton SE, Sergides M, Patel R, Karczewska E, Maragó OM, Jones PH. Evanescent wave optical trapping and transport of micro- and nanoparticles on tapered optical fibers. *Journal of Quantitative Spectroscopy and Radiation Transfer*. 2012;**113**(18): 2512-2520. DOI: 10.1016/j.jqsrt.2012.06.005

[36] Lægsgaard J. Theory of surface second-harmonic generation in silica nanowires. *Journal of the Optical Society of America B: Optical Physics*. 2010;**27**(7):1317-1324. DOI: 10.1364/JOSAB.27.001317

[37] Roselló-Mechó X, Delgado-Pinar M, Díez A, Andrés MV. Measurement of Pockels' coefficients and demonstration of the anisotropy of the elasto-optic effect in optical fibers under axial strain. *Optics Letters*. 2016;**41**(13):2934-2937. DOI: 10.1364/OL.41.002934

[38] Jülich F, Aulbach L, Wilfert A, Kratzer P, Kuttler R, Roths J. Gauge factors of fibre Bragg grating strain sensors in different types of optical fibres. *Measurement Science and Technology*. 2013;**24**(9):094007. DOI: 10.1088/0957-0233/24/9/094007

[39] Pöllinger M, O'Shea D, Warken F, Rauschenbeutel A. Ultrahigh-Q tunable whispering-gallery-mode microresonator. *Physical Review Letters*. 2009;**103**:053901. DOI: 10.1103/PhysRevLett.103.053901

[40] Linslal CL, Kailasnath M, Mathew S, Nideep TK, Radhakrishnan P,

Nampoorei VPN, et al. Tuning whispering gallery lasing modes from polymer fibers under tensile strain. *Optics Letters*. 2016;**41**(3):551-554. DOI: 10.1364/OL.41.000551

[41] Lide DR. *CRC Handbook of Chemistry and Physics*. 84th ed. Boca Raton: CRC Press; 2003

[42] Shackelford JF, Alexander W. *CRC Materials Science and Engineering Handbook*. 3rd ed. Boca Raton: CRC Press; 2001